

DZYALOSHINKII-MORIYA INTERACTION AND HALL EFFECTS IN BULK
CHIRAL MAGNETS FROM FIRST PRINCIPLE CALCULATIONS

A Dissertation

by

JACOB DAVIS GAYLES

Submitted to the Office of Graduate and Professional Studies of
Texas A&M University
in partial fulfillment of the requirements for the degree of

DOCTOR OF PHILOSOPHY

Chair of Committee,	Artem Abanov
Co-Chair of Committee,	Jairo Sinova
Committee Members,	Glenn Agnolet Rusty Harris
Head of Department,	Peter McIntyre

December 2016

Major Subject: Physics

Copyright 2016 Jacob Davis Gayles

ABSTRACT

In this dissertation I will discuss the effect of real, momentum, and mixed space Berry phases in B20 compounds: MnSi, $\text{Mn}_{1-x}\text{Fe}_x\text{Ge}$, and $\text{Fe}_{1-y}\text{Co}_y\text{Ge}$. Recently there has been a tremendous experimental effort in stabilizing skyrmion crystal phases in these systems. We calculate, from state of the art first principle calculations, the Dzyaloshinskii-Moriya interaction (DMI), the anomalous Hall effect (AHE), and the topological Hall effect (THE). These three effects are intimately related through Berry phase physics, where I test how the strength of the exchange interactions and spin-orbit coupling play a role in the underlying physics for these systems. In this dissertation, I compare the strength of different first principle methods in calculating magnetic ground state properties in B20 compounds. In this, I see that Full Potential Linearized Augmented Plane Wave Method treats different magnetic states most accurately. Calculations of spin-spiral states are performed in these B20 compounds showing long wavelength spin-spirals due to the interaction of the exchange stiffness and the DMI field. The DMI in these materials reaches maxima and minima with alloying concentration due the hybridization of d -states, which I complement with an intuitive tight-binding model. The AHE is also calculated in these materials and shows remarkable agreement with experimental measurements. Whereas the THE agrees in sign for these materials and quantitatively in the FeGe, the values in MnGe predict smaller values. This discrepancy, where the DMI is also smaller than expected, is attributed to breakdown of the adiabatic theorem, where in MnGe, the magnetic texture rotates too quickly to capture the real space Berry phase physics. The work of this dissertation is compared with computational results that have followed and ongoing experimental studies.

DEDICATION

For my beautiful son Noah Emanuel, and my amazing big brother James Sol.

ACKNOWLEDGEMENTS

Firstly, I would like to show acknowledgement and appreciation for my advisors Jairo Sinova and Artem Abanov, who have increased my own inspiration for the field of physics through their own excitement and vigor for the field. Without the many discussions and support this thesis would not have been possible. Their depth in knowledge of the field has given me a model to strive for. My advisors have continually put my academic goals as a priority. I would also like to acknowledge the INSPIRE working group who have shown immense support, with many discussions and last minute readings of this thesis. I would also like to thank the physics departments of Johannes Gutenberg Universität and of Texas A&M for facilitating my research and studies. Lastly, I would like to thank Cristian Cernov for the production of many of the high-quality figures.

I would also like to thank the group in the Jülich Forschungszentrum, specifically Frank Freimuth, Yuriy Mokrousov, and Stefan Blügel. Here, the learning of many of the coding techniques and discussion were taken. Specifically, I would like to thank Frank Freimuth who spent countless time with me on the technical details of this work. I would also like to thank the experimental group of Chris Marrows, and his student Charles Spencer for the experimental discussion and support.

Lastly, I would like to thank my family and friends for giving me support and encouragement throughout the process.

CONTRIBUTORS AND FUNDING SOURCES

Contributors Section

This work was supervised by a dissertation committee, consisting of Professor Artem Abanov (chair), Professor Jairo Sinova (co-advisor) and Professor Glenn An-golet, of the Department of Physics & Astronomy, and Professor Harlan R. Harris, of the Department of Electrical & Computer engineering.

All work for the dissertation was completed by the student, in collaboration with Dr. Frank Freimuth, Dr. Timo Schena, Dr. Giovanna Lani, Professor Phivos Mavropoulos, Professor Yuriy Mokrousov, and Professor Stefan Blügel, at the Peter Grünberg Institut & Institute for Advanced Simulation, Forschungszentrum Jülich and JARA, and Professor Rembert A. Duine, at the Institute for Theoretical Physics and Center for Extreme Matter and Emergent Phenomena, Utrecht University. The experimental work was completed by Charles Spencer and Professor Christopher Marrows, at the Department of Physics and Astronomy at the University of Leeds.

Funding Sources

Graduate study was supported by the fellowship, LSAMP Bridge to the Doctorate from Texas A&M University. This work was made possible in part by, the NSF grant no. DMR-1105512, Alexander von Humboldt Foundation, the ERC Synergy Grant SC2 (No. 610115), the Transregional Collaborative Research Center (SFB/TRR) 173 SPIN+X, the HGF Programme VH-NG 513 and DFG SPP 1568.

NOMENCLATURE

1-D	One-Dimensional
2-D	Two-Dimensional
3-D	Three-Dimensional
AHE	Anomalous Hall Effect
ASA	Atomic Sphere Approximation
BC	Berry-Curvature
DFT	Density Functional Theory
DMI	Dzyaloshinskii-Moriya Interaction
(F)LAPW	(Full Potential) Linearized Augmented Planewave
GGA	Generalized Gradient Approximation
HK	Hohenberg-Kohn
IBZ	Irreducible Brillouin Zone
KS	Kohn-Sham
LCAO	Linear Combination of Atomic Orbitals
LDA	Local Density Approximation
LMTO	Linear Muffin-Tin Orbital
PP	Pseudopotentials
PUC	Primitive Unit Cell
SB	Semiclassical Boltzmann
SK	Slater-Koster
Skx	Skyrmion Crystal
SOC	Spin-Orbit Coupling
SOI	Spin-Orbit Interaction

SS	Spin-Spiral
TB	Tight-Binding
TF	Thomas-Fermi
THE	Topological Hall Effect
TM	Transition-Metal
xc	Exchange Correlation

TABLE OF CONTENTS

	Page
ABSTRACT	ii
DEDICATION	iii
ACKNOWLEDGEMENTS	iv
CONTRIBUTORS AND FUNDING SOURCES	v
NOMENCLATURE	vi
TABLE OF CONTENTS	viii
LIST OF FIGURES	x
1. INTRODUCTION	1
2. FIRST PRINCIPLE CALCULATIONS	6
2.1 Density Functional Theory	7
2.1.1 The Hohenberg-Kohn Theorem	7
2.1.2 Kohn-Sham States and Jacob's Ladder	9
2.2 DFT Methods	11
2.2.1 TB-LMTO-ASA	12
2.2.2 (F)LAPW	15
2.2.3 DFT Method Rankings	16
2.3 Spin-Orbit Coupling in DFT	18
2.4 DFT Results in B20 Compounds	21
2.4.1 Alloy Calculations	24
2.4.2 Spin-Orbit Coupling in B20 Compounds	32
3. HEISENBERG INTERACTIONS AND NON-COLLINEAR MAGNETISM	36
3.1 Classical Spin Hamiltonian	36
3.1.1 Symmetric Exchange	37
3.1.2 Antisymmetric Exchange	38
3.1.3 Symmetry of the DMI	39
3.1.4 Anisotropy	40

3.1.5	Higher Order Exchange	41
3.2	First-Principles approach to Non-Collinear Magnetism	42
3.2.1	Spin-Stiffness	45
3.2.2	Dzyaloshinskii-Moriya Interaction	50
3.2.3	Band Structures of Spin-Spiral States	52
3.3	TIGHT-BINDING CALCULATIONS OF THE DMI	54
3.4	Tight-Binding Approximation	54
3.5	Slater-Koster Two-Center Approximation	56
3.6	Trimer Model for B20 Compounds	59
3.7	WANNIER FUNCTIONS FOR BERRY CURVATURE	67
3.8	Theory	68
3.9	Computation	71
3.10	Band Structure Results	73
3.11	BERRY PHASE EFFECTS	77
3.12	General Berry-Phase Theory	78
3.13	Anomalous Hall Effect	79
3.14	Topological Hall Effect	81
3.15	Phase-Space Berry Effects	84
3.16	Results in B20 Systems	85
3.17	OVERVIEW AND DISCUSSION	90
3.18	Theoretical Studies	90
3.19	Experimental Studies	93
3.20	Experimental and Computational Studies of FeCoGe	96
4.	CONCLUSION	102
	REFERENCES	105
	APPENDIX A. BLOCH THEOREM	127
A.1	Periodic Systems	127
A.2	Generalized Bloch Theorem	128
	APPENDIX B. EXCHANGE AND CORRELATIONS FUNCTIONALS	130
B.1	Local Density Approximation	130
B.2	Generalized Gradient Approximation	131
	APPENDIX C. CONVERGENCE	132

LIST OF FIGURES

FIGURE	Page
1.1 a) Spiral skyrmion b) hedgehog skyrmion [78]	2
1.2 a) B20 structure with P2 ₁ 3 symmetry. The grey (black) are the magnetic transition metal (semi-metallic Ge) atoms. The transition metal ion carries the larger magnetic moment and the spin-spiral. The diagonal line shows atoms which keep the C3 symmetry. b)Magnetic temperature phase diagram of MnSi showing the onset of the A-phase [120].	3
2.1 Comparison of a wavefunction in the Coulomb potential of the nucleus (blue) to the one in the pseudo-potential (red). The real and the pseudo wavefunction and potentials match above a certain cutoff radius.	15
2.2 Right and left-handed crystal chiralities of the B20 compound. The green arrows show an arbitrary magnetization direction.	22
2.3 First principles collinear ferromagnetic spin- and orbitally-resolved DOS at a given concentration x of a) 0 for MnGe, b) 0.4, c) 0.8, d) 1.0 for FeGe, for the d_{xy} (solid red), $d_{x^2-y^2}$ (dashed blue), and p_x (purple with dots) orbitals, computed without SOC.	25
2.4 <i>top</i> <i>Ab initio</i> input of the lattice constant in Fe _{1-y} Co _y Ge compared to thin film measurements (red) of the lattice constant. <i>bottom</i> Comparison of magnetic moment per formula unit (f.u.) for <i>ab initio</i> and experiment.	27
2.5 <i>Top</i> Collinear ferromagnetic <i>ab initio</i> band structure comparison in Mn _{1-x} Fe _x Ge with x=0.1 and x=-0.8 using the VCA approximation for the majority (maj) and minority (min) spin channels. <i>Bottom</i> Collinear ferromagnetic <i>ab initio</i> band structure comparison in Mn _{1-x} Fe _x Ge with x=0.9 and x=-0.8 using the VCA approximation. .	30

2.6	<i>Top</i> VCA calculations of the FM (blue closed) and AFM (red open) of $\text{Cr}_{1-w}\text{Mn}_w\text{Ge}$, $\text{Mn}_{1-x}\text{Fe}_x\text{Ge}$, $\text{Fe}_{1-y}\text{Co}_y\text{Ge}$ magnetic moment shown as squares and that of MnSi shown as circles. <i>Bottom</i> Difference in energy of the AFM and FM state.	31
2.7	<i>Left</i> Orbital projected bands of FeGe with SOC. <i>Bottom</i> Orbital projected bands of MnGe with SOC. The red (blue) circles show the d (p) character of the bands and the size of the circles show the amount of the SOC \times 15.	33
2.8	Band structure of MnGe with SOC for the SQA in the 001 (green) and the (111).	34
3.1	Half of a homogeneous spin-spiral state on a mono-atomic 1D magnetic lattice with φ being the rotation angle between neighboring unit cells	44
3.2	<i>Left</i> Spin-spiral dispersion relation for $\text{Mn}_{1-x}\text{Fe}_x\text{Ge}$ for $x=1$ (black), $x=0$ (red) and $x=0.8$ (green) up to half of the spin-spiral Brillouin zone, M, along the high symmetry direction (q,q,q) . <i>Right</i> Spin-spiral dispersion relation for $\text{Mn}_{0.2}\text{Fe}_{0.8}\text{Ge}$ for high symmetry spin spiral directions along $(0,0,q)$ in black, $(0,q,q)$ in red, and (q,q,q) in green. The inset shows the spin spiral direction up to the edge of the Brillouin zone.	47
3.3	Plot of the spin-stiffness (blue) on a log scale and the magnetic moment (green) in $\text{Fe}_{1-y}\text{Co}_y\text{Ge}$. The line at $x=0.5$ is the value with the lowest DMI where one would expect the size of the skyrmions to increase to a ferromagnetic state with no chirality.	49
3.4	<i>Left:</i> *Strength of the DMI as a function of concentration x in $\text{Mn}_{1-x}\text{Fe}_x\text{Ge}$ alloys. The total value of the DMI (filled squares) is decomposed into the contributions coming from the transition-metal (red dots) and Ge (blue dots). The inset depicts the crystal structure of the studied B20 compound, with light grey and dark grey spheres representing the transition-metal (TM) and Ge atoms, respectively. <i>Right:</i> Strength of the DMI as a function of concentration x in $\text{Fe}_{1-y}\text{Co}_y\text{Ge}$ alloys.	51

3.5	Left panels: the unperturbed spin-spiral bands for a) MnGe and b) FeGe with the spin-orbit correction to them displayed with blue (positive) and red (negative) dots. Right panels: the density of SOC-induced energy correction to the eigenvalues at a given energy, e_{DM} , and the value of the total DMI energy as a function of Fermi energy E_F , E_{DM} , obtained as an integral of all e_{DM} below E_F	53
3.6	Hamiltonian hopping matrix elements between s , p and d states. Where red(blue) lobes are positive(negative).	57
3.7	Schematic figures for two-center elements between $p - x$ and p_z for sites distance by vector \mathbf{R}	58
3.8	Schematic figure of the trimer model with grey sites as non-collinear magnetic sites with angle of 2φ between magnetic directions and $d_{x^2-y^2}(d_{xy})$ -states in blue(red). The dark site is contains the spin-degenerate p -state.	59
3.9	<i>Bottom</i> : Strength of the DMI as a function of electron occupation computed from a simple tight-binding model of a finite trimer (structure shown in inset). Essential is the breaking of local inversion symmetry of the bond between the transition-metal (light gray) and Ge (dark gray). The direction of the left (S_1) and right (S_2) spin lies in the xy plane, and the DMI vector is pointing out of plane. <i>Top</i> : schematic evolution of the d states at the Fermi energy in the tight-binding model with electron occupation.	64
3.10	Spin and Orbitally-resolved ferromagnetic tight-binding DOS at a given occupation of a) 4.2, b) 4.7, c) 4.9, d) 5.2 electrons for the d_{xy} (solid red), $d_{x^2-y^2}$ (dashed blue), and p_x (purple with dots) orbitals.	65
3.11	In the top panels Orbitally-resolved ferromagnetic tight-binding DOS at a given occupation of a) 4.2, b) 4.7, c) 4.9, d) 5.2 electrons for the d_{xy} (solid red), $d_{x^2-y^2}$ (dashed blue), and p_x (green) orbitals. The bottom panels show the Fermi energy dependence of the DMI.	66
3.12	<i>Left</i> SOC bands of FeGe <i>ab-initio</i> in black and the MLWF in red for the outer window. <i>Right</i> Zoom of the plot on the left ± 2 eV around the Fermi level.	74

3.13	<i>Top eft</i> SOC bands of MnGe <i>ab-initio</i> in black and the MLWF in red from the bottom of the frozen energy window to -1 eV below the Fermi level. <i>Top right</i> MLWF at ± 1 eV around the Fermi Level. <i>Bottom left</i> MLWF from 1 eV above the Fermi level to 3 eV above the Fermi level. <i>Bottom right</i> MLWF from 3 eV above the Fermi level to 7 eV above the Fermi level.	76
3.14	<i>Left</i> Black bands show majority spin bands for $\text{Mn}_{0.4}\text{Fe}_{0.6}\text{Ge}$ and red circles are the fitted MLWFs. <i>Right</i> Black bands show minority spin bands for $\text{Mn}_{0.4}\text{Fe}_{0.6}\text{Ge}$ and blue circles are the fitted MLWFs.	76
3.15	The anomalous Hall conductivity σ_{xy} in FeGe as a function of the disorder parameter with the magnetization in the negative z-direction.	86
3.16	<i>Top Left:</i> Plot of the number of states as a function the Fermi energy for MnGe for the majority (red) and minority (green) spin. <i>Top Right:</i> The longitudinal conductivity as a function of the fermi energy for the majority (red) and minority (green) spin. <i>Bottom Left:</i> The ordinary Hall conductivity as a function of the fermi energy for the majority (red) and minority (green) spin. <i>Bottom Right:</i> The ordinary Hall conductivity as a function of the disorder parameter for the majority (red) and minority (green) spin.	88
3.17	<i>Left:</i> The anomalous hall conductivity (blue squares) and topological Hall constant (green circles) is plotted for $\text{Mn}_{1-x}\text{Fe}_x\text{Ge}$ and <i>Right :</i> $\text{Fe}_{1-y}\text{Co}_y\text{Ge}$ for different concentrations of Fe.	89
3.18	<i>Top:</i> Schematic of static spin-current Doppler shift. <i>Bottom:</i> Comparison of DMI for expectation of the static spin-current (red) and from the values of a helical spin-spiral (blue) [79].	91
3.19	<i>Left:</i> AHE and DMI as a function of chemical potential from FeGe. <i>Right:</i> x and y component of the DMI as a function of uniaxial strain on the y axis at the concentration of $n=-0.45$ [84].	92
3.20	The Hall conductivity (black circles) and magnetization as a functions of temperature at fields higher than the critical field to cause a ferromagnetic structure. The insets show the temperature dependence of the zero field resistivity [72].	95
3.21	Experimental calculation of the exchange constant and the DMI using two methods [51].	97

3.22	Helical wavelength of the $\text{Fe}_{1-y}\text{Co}_y\text{Ge}$ compound as a function of y comparing the thin film PNR (blue), bulk <i>ab-initio</i> (red), and bulk SANS (black) [50]. The inset is a zoom out of the original plot, where lines are shown as guides for the eye.	99
3.23	<i>Left:</i> Comparison of first-principles (green with line) longitudinal conductivity with that of the thin film measurement. <i>Right:</i> The anomalous Hall conductivity for $\text{Fe}_{1-y}\text{Co}_y\text{Ge}$ comparing the first-principle and experimental results.	100
C.1	<i>Left:</i> Total energy convergence in FeGe as a function of the number of kpoints in the IBZ. <i>Right:</i> Total energy convergence in FeGe as a function of the planewave cutoff radius K_{max}	132

1. INTRODUCTION

Recently, the interest in magnetic skyrmions [16, 136] has generated a significant effort in spintronics research for the purpose of use in logic devices [182, 181, 137, 69, 39]. Magnetic Skyrmions are topologically protected non-trivial magnetic structures (see fig. 1.1), that stem from ideas of nuclear physics [149]. The topological charge for a skyrmion in two dimensions can be detailed as,

$$S = \frac{1}{4\pi} \int \hat{\mathbf{n}} \cdot (\partial_x \hat{\mathbf{n}} \times \partial_y \hat{\mathbf{n}}) dx dy \quad (1.1)$$

where $\hat{\mathbf{n}}$ is the magnetization unit vector. The topological charge, S , can take integer values from 0, $\pm 1, \pm 2, \pm 3, \dots$, is a topologically non-trivial object (for $|S| > 0$) and a (-)+ corresponds to a (anti-)skyrmion. Experimentally, the skyrmion phase can be detected using Lorentz transmission electron microscopy, hall measurements, small angle neutron scattering and magnetic susceptibility measurements [113, 179, 171, 129]. These topologically protected objects were first seen to be stable in Cuprates [2] and the B20 transition metal compounds [113, 179, 171, 129, 145, 49] and more recently in Heusler materials [104]. Although not necessary, the Dzyaloshinskii-Moriya interaction (DMI) plays a crucial role in the stabilization of magnetic skyrmions and domain walls with chiral textures [75, 7, 65, 130]. The DMI arises in magnetic systems with spin-orbit coupling and broken structural inversion symmetry [110, 109, 108, 75, 7, 65, 130]. Contradictory to the symmetric scalar Heisenberg exchange interaction, the DMI prefers spins to point perpendicular for linked magnetic moments.

The DMI is a ground state property that can be calculated from a phase-space

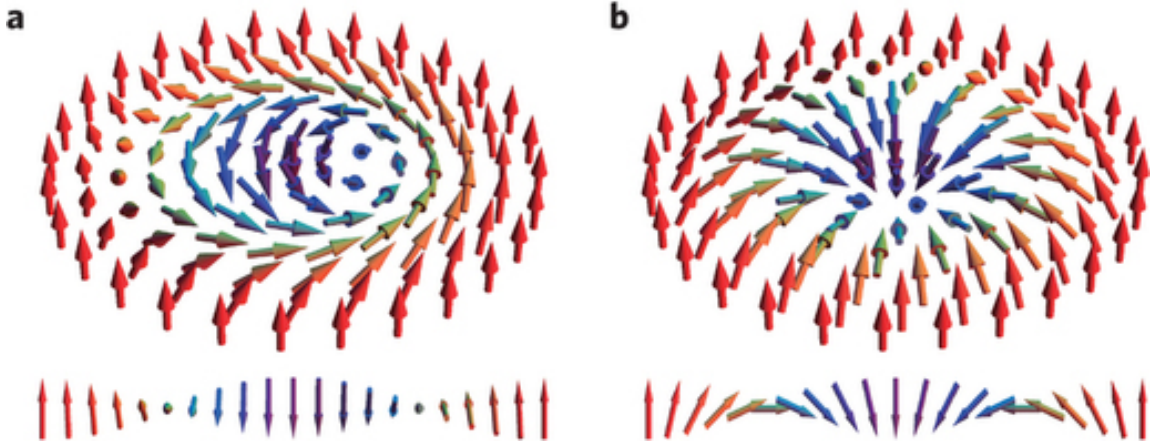


Figure 1.1: a) Spiral skyrmion b) hedgehog skyrmion [78]

Berry curvature where crossings in reciprocal and real space lead to a finite DMI. Analogous to the DMI, the intrinsic anomalous Hall effect (AHE) is seen as the momentum-space Berry Curvature where crossing Bloch functions in the k -space produce magnetic *monopoles* accelerating charged quasi-particles with spin perpendicular to both the external electric field and the magnetization direction [114]. The AHE also has contributions from non-Berry phase effects due to impurities giving rise to the impurity-density independent side jump mechanism and the impurity-density dependent skew-scattering mechanism [114]. In principle the strength and sign of the scattering mechanisms are material and sample preparation dependent, whereas the intrinsic mechanism is purely dependent on the electronic structure. Furthermore, real space Berry-phases can arise in non-trivial magnetic textures with a finite winding number, S i.e. a skyrmion. The topological Hall effect (THE) arises from a finite Berry phase due to an emergent magnetic field that acts with an opposite sign on charged quasiparticles with opposite spin [20]. These three phenomena can be gathered into a 6×6 anti-symmetric phase-space Berry curvature (BC) tensor (described below) [174].

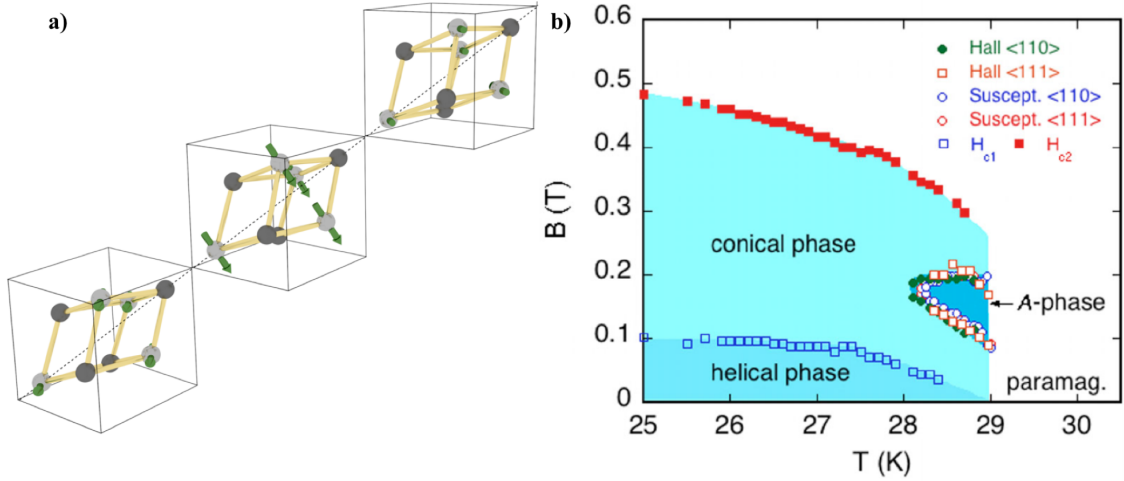


Figure 1.2: a) B20 structure with $P2_13$ symmetry. The grey (black) are the magnetic transition metal (semi-metallic Ge) atoms. The transition metal ion carries the larger magnetic moment and the spin-spiral. The diagonal line shows atoms which keep the $C3$ symmetry. b) Magnetic temperature phase diagram of MnSi showing the onset of the A -phase [120].

In this dissertation we study the effect of this BC tensor in the limits of strong and weak interactions of magnetism and spin orbit coupling, resulting in these emergent phenomena using first principle density functional theory (DFT) calculations. In recent years DFT has shown promising results in real materials for the calculation of the AHE for bulk materials and the DMI in bilayer systems, reproducing qualitative and in some cases predicting quantitative results [73, 42, 44, 131]. However, there has been little description of the THE in realistic materials [42]. Furthermore, the B20 compounds $MnSi$, $Mn_{1-x}Fe_xGe$ and $Fe_{1-y}Co_yGe$ are particularly interesting materials to study from a computational effort, in that a range of effects, due to the electronic structure, can be seen in these materials without changing the crystal symmetry. These materials have become very popular for experimentalists, where $MnSi$ has small magnetic moments dominated by spin fluctuations [67], $Mn_{1-x}Fe_xGe$ and $Fe_{1-y}Co_yGe$ show that spiral skyrmion (see fig. 1.1) sizes change several orders

of magnitude with concentration, and lastly CoGe collapses to a paramagnetic phase [28, 118].

The work of Pfleiderer et al. initiated experimental studies of skyrmions in condensed matter physics [120, 129]. In this seminal experimental work, the authors were the first to experimentally realize the illusive A -phase, i.e skyrmions, in the B20 compound MnSi below the transition temperature of 29.5 K. A few years later the work by Shibata et al. characterized the skyrmion crystal phase of $\text{Mn}_{1-x}\text{Fe}_x\text{Ge}$ as a function of concentration x [156, 145, 107]. In these studies it was found that at the critical concentration of $x=0.8$ there is a reversal in the chirality of the skyrmions. Furthermore, the authors found that at this critical point the size of the skyrmions blow up and as the concentration recedes from this point the size decreases. It is found that the skyrmion sizes in FeGe are on the order of 70 nm [64], where as MnGe shows the smallest skyrmion crystal phase of 3 nm [97, 34] giving rise to a large THE [71]. In addition to the work of Shibata et al., Grigoriev et al. nearly simultaneously showed that there is a discontinuity around the critical concentration for the helical pitch length in $\text{Mn}_{1-x}\text{Fe}_x\text{Ge}$ [49]. However, there has not been any computational or theoretical studies to explain the varying skyrmion size in these materials as a function of concentration.

In this dissertation we will show that these phenomena in the B20 compounds are governed by Berry phase physics, by using first principle calculations. This dissertation is divided into three parts: *i*) first principle calculations of the DMI and the simple tight-binding model to interpret the results, *ii*) calculation of the hall effects with the use of the Wannier interpolation and the connection to Berry-phase effects, *iii*) lastly, the connection to recent studies of the DMI and ongoing calculations in direct comparison to experiments. In the first part we will discuss the advantages and shortcomings of our DFT to treat magnetism in B20 compounds,

while also comparing it to that of other methods. Within the DFT method I will discuss how to calculate the DMI in the long wavelength approximation. We will describe simple models to explain these systems and how they give an intuitive picture to the underlying physics. We then discuss the calculations of the AHE and THE in the BC picture using Wannier functions [111, 166, 42] as input into the Kubo formula and semiclassical Boltzmann formulae, respectively. Lastly, I will briefly discuss some of the ongoing results using DFT in direct comparison to experimental measurements. The dissertation is then concluded in Section 4.

2. FIRST PRINCIPLE CALCULATIONS

Although, this is the first section in this dissertation, it is not the heart but the backbone of this work. Despite the fact that first principle calculations are not the main focus of this body of work, we can make use of electronic structure methods to obtain experimentally relevant results. First principle calculations show predictive and experimentally comparable results for many types of materials and states of matter [68]. In this dissertation I will primarily focus on density functional theory (DFT) calculations in the bulk helimagnetic B20 compounds.

Within the last sixty years DFT has shown very promising results for many types of materials, i.e. magnetic, metallic, and semiconductive. One of the well-known shortcomings of DFT is the incorrect prediction of band gaps in semiconductors and insulators. However, within recent years there has been a significant effort in correcting this problem using state-of-the-art approximations, such as the GW approximation, hybrid functionals, time-dependent DFT and so on. These methods can also be applied to magnetic metals, however they are outside the focus of this work, in that we are only interested in ground state properties. In many cases, one may wish to calculate properties of materials based on impurities or disorder. For these types of calculations one would use approximations such as KKR [32] and CPA [134, 91], which are also outside the scope of this work.

The main purpose of the dissertation is to understand Berry phase effects, such as the anomalous Hall effect, Dzyaloshinskii-Moriya interaction and topological Hall effect in magnetic materials. It is necessary to have a computationally accurate description of the electronic ground state in order to compute relevant quantities of these phenomena. In that vein, most of this section is devoted to comparing different

types of electronic structure methods for the B20 compounds. This results will serve as a basis for all results in this work.

2.1 Density Functional Theory

DFT began in the early 1930's for calculating the properties of solids. However it was not until the theorems of Hohenberg and Kohn and the reformulation of the problem of by Kohn and Sham that DFT became practical for the calculation of condensed matter properties in realistic materials. Walter Kohn has received the Nobel prize in chemistry for his contributions to DFT. In this section, we will set the stage for DFT calculations by briefly describing the seminal work of Kohn. We also discuss the relevance of the Jacob's ladder of exchange-correlation approximations.

2.1.1 *The Hohenberg-Kohn Theorem*

The beginning of DFT started with the Thomas-Fermi (TF) model[159, 37]. This was the first step in simplifying the many-body Schrödinger equation for N interacting electrons with $3N$ degrees of freedom. The TF model aimed to solve a many-body problem for a functional, the total energy $E[n]$, in terms of the electron density, $n(\mathbf{r})$, that is a function of the position. The TF model's approximations are crude in the simplification of the kinetic energy of electrons as a functional of the local density for non-interacting electrons of a homogeneous electron gas.

In addition, the model neglected exchange and correlation of the electrons. A few years later, Dirac[27] extended the model to include the exchange energy, due to the Pauli exclusion principle[123, 125]. This model is only correct for infinite nuclear charge. However, the approximations fail to capture the relevant physics in the description of electrons in matter. Specifically, in molecules, the model gives an incorrect picture of the binding[158].

Contrary to the TF approximations, the Hohenberg-Kohn (HK) approach is exact

for the formulation of the electron density in a many-body system of interacting particles. Neglecting the nuclei-nuclei interaction at the moment, the Hamiltonian for N electrons in an external potential, $V_{ext}(\mathbf{r})$, can be written as,

$$\hat{H} = \frac{\hbar^2}{2m_e} \sum_i^N \nabla_i^2 + \sum_i^N V_{ext}(\mathbf{r}_i) + \frac{1}{2} \sum_{i \neq j}^N \frac{e^2}{|\mathbf{r}_i - \mathbf{r}_j|}. \quad (2.1)$$

In Eq. 2.1 the first sum is the kinetic energy of the electrons, and the kinetic energy of the nuclei are treated adiabatically in the Born-Oppenheimer approximation[18]. The last term is the electron-electron Coulomb interaction. Lastly, $V_{ext}(\mathbf{r}_i)$ includes all external forces on an electron i , i.e. the nuclei and any external field.

The objective of the HK approach is to solve a system of interacting particles in an external potential as a function of only the electron density, that contain all the information of the many-particle wave function. The theorem states that ground state density $n_o(\mathbf{r})$ uniquely determines the $V_{ext}(\mathbf{r})$ up to a constant. Secondly, HK proved that if the functional $E[n]$ is known, then the true ground state density minimizes the functional, given that the total number of particles does not change. The HK theorems lead to a very powerful statement such that the energy functional can be written as,

$$E_{HK}[n] = F_{HK}[n] + \int d\mathbf{r} V_{ext}(\mathbf{r})n(\mathbf{r}) + E_{NN}. \quad (2.2)$$

Here I have introduced the term E_{NN} as the nuclei-nuclei interaction. The functional $F_{HK}[n] = T[n] + E_{int}[n]$ is a universal functional for all systems of N particles, where the kinetic, $T[n]$, and the interaction, E_{int} , energy are only functionals of the density. Levy[89] and Lieb [90] have generalized and simplified the HK theorem. DFT has also been extended for spin dependent densities[164, 68, 53] and for that

current-DFT[163].

2.1.2 Kohn-Sham States and Jacob's Ladder

The TF approximation gave an intuitive picture of DFT, however the crude approximations are too inaccurate for the understanding of real systems. Contrary to the TF approximation, the HK theorems are exact, yet they lead to no practical method of the calculation of $F_{HK}[n] = T[n] + E_{int}[n]$ in equation 2.2. Quantum Monte Carlo methods can calculate exact properties by a direct treatment of the many-body wavefunction[22, 41]. Hartree-Fock allows for a mean-field approximation (MFA) of the many-body problem with an exact description of the exchange[55, 56, 40, 151]. However, both of these methods are computationally expensive for large solid state systems. Kohn and Sham (KS) proposed a method that takes into account a single-particle picture in a MFA that includes exchange and correlation on a density functional setting[83].

The KS method is the most computationally accepted method for quantitatively and qualitatively describing the nature of large many-body systems. The self-consistent method replaces the many-body problem of HK with that of independent particles in an interacting density. The HK energy functional can be rewritten as,

$$E_{KS}[n] = T_{ind}[n] + \int d\mathbf{r} V_{ext}(\mathbf{r})n(\mathbf{r}) + E_{NN} + E_H[n] + E_{xc}[n]. \quad (2.3)$$

Here, I have introduced the term T_{ind} for the independent-particle kinetic energy. Secondly, there is the classical self-interaction of the electron density, E_H , which is typically called the Hartree energy. The last term in Eq. 2.3 is the exchange-correlation (XC) energy which includes all many body effects, and is written as so,

$$E_{xc}[n] = F_{HK}[n] - (T_{ind}[n] + E_H[n]) \quad (2.4)$$

All of the many-body effects are in the XC energy described in Eq. 2.4. Eq. 2.3 solves the many-body problem for the correct XC functional. In practical calculations, the XC functional is approximated. There are many approximations for the XC functional, employing different constraints on the density. The level of these approximations is termed *Jacob's Ladder* of DFT[157, 127].

The practical advantage of DFT comes from the use of approximate XC functionals that depend on the locality of the density. The strength of these approximations increases with constraints on some physical quantity, e.g. the charge density, gradients of the density, the kinetic energy density, the KS orbitals and non-local contributions to the XC energy. These functionals should be determined heuristically for transferability and applicability to specific problems. On the *bottom* level of Jacob's Ladder is the Hartree-Fock method where exchange is treated exactly and the correlation energy is neglected.

1st Level The first level on this ladder is the local density approximation (LDA). The effects of XC potential are local in the limit of the homogenous electron gas (HEG). In this approach one can use the LDA (or the local spin density approximation (LSDA)), where the XC energy is an integral over space with the XC energy density equivalent to that of an HEG,

$$E_{xc}^{LSDA}[n^\uparrow, n^\downarrow] = \int d\mathbf{r} n(\mathbf{r}) \epsilon_{xc}^{HEG}(n^\uparrow(\mathbf{r}), n^\downarrow(\mathbf{r})). \quad (2.5)$$

Here, I have split the total density into spin dependent densities with the assumption that the spin-quantization axis is collinear at all points in space. The generalization to non-collinear spins and the exact form of the XC energy density can be found in the Appendix B. The LDA and LSDA approximations work best for descriptions of systems that are close to the HEG, e.g. a nearly-free-electron metal.

The approximation fails in inhomogeneous cases such as atoms and molecules where the density must smoothly go to zero away from the centre.

2nd Level The success of the LSDA method has led to the development of the generalized gradient approximation (GGA). The GGA approximation is widely used in chemistry, in addition to the main XC functional used in this body of work. The objective GGA describes the functional in terms of the local density as well as the magnitude of gradient of the density $|\nabla n^\sigma(\mathbf{r})|$. The many GGAs propose functions to treat large gradients for desired quantities, which can be defined in a general form,

$$E_{xc}^{GGA}[n^\uparrow, n^\downarrow] = \int d\mathbf{r} n(\mathbf{r}) \epsilon_{xc}(n^\uparrow(\mathbf{r}), n^\downarrow(\mathbf{r}), |\nabla n^\uparrow(\mathbf{r})|, |\nabla n^\downarrow(\mathbf{r})|, \dots). \quad (2.6)$$

In the appendix the forms of Perdew and Wang (PW91) [128], and Perdew, Burke and Enzerhof (PBE) [126] are discussed. These functionals have led to some of the most highly cited papers in physics and have shown accurate descriptions of many materials, from solids to molecules. There are higher levels of Jacob's ladder, such as meta-GGA's and hybrid functionals, which are beyond the scope of this dissertation.

2.2 DFT Methods

In actual DFT calculations one has to take care of how the basis functions are treated. In principle, the most efficient way to treat Bloch functions (see Appendix...) as a linear combination of plane waves. However, close to the nucleus the infinite Coulomb potential causes rapid variations in the wavefunction, which requires an increasing number of plane waves for larger Z (See Fig. 2.1). In attempt to circumvent this issue the many DFT codes take different approximations of a given area surrounding the nucleus and treat the interstitial differently. In this section we will discuss the details of the TB-LMTO code primarily developed by Ole Krogh Andersen at the MPI institute in Stuttgart. We will also discuss the comparison

to other methods, such as pseudo-potentials (PP), the full potential linearized augmented plane wave (FLAPW) method and linear combination of atomic orbitals (LCAO), and the various advantages and shortcomings of the different DFT codes that use these methods [100]. These methods attempt to solve the singularity of the Coulomb potential giving rise to a rapidly varying wavefunction as $r \rightarrow 0$ (See Fig. 2.1)

2.2.1 TB-LMTO-ASA

Firstly, lets begin with describing a very general Hamiltonian for linear equations, where the linearity governs the differential equation, and for a muffin-tin (MT) potential which encapsulates many of the methods listed above. We would like to solve a Hamiltonian for Bloch functions expanded in a set of basis functions $\psi_{i,n}(\mathbf{r}) = \sum_n c_{i,n}(\mathbf{k})\chi_n(\mathbf{r})$. For simplicity we will only take into account a flat interstitial potential with muffin-tin radii of S. For a single muffin-tin the Schrödinger equation follows:

$$\left(-\hbar^2/2m_e \frac{d^2}{dr^2} + V_{MT} - E_\nu \right) r\psi(E_\nu, r) = 0, \quad (2.7)$$

with an arbitrarily chosen energy $\varepsilon = E_\nu$. The energy partial derivative of a normalized ψ in the MT taken at $\varepsilon = E_\nu$. From here it is easy to show that ψ and $\dot{\psi}$ are orthogonal, and the two functions span a larger space with,

$$(\hat{H} - \varepsilon)\dot{\psi}(\varepsilon, r) = \psi(\varepsilon, r) \quad (2.8)$$

Higher order derivatives of ψ can be formulated in terms of ψ and $\dot{\psi}$. The augmentation functions as a function of the energy can be specified in terms of the

dimensionless logarithmic derivative,

$$D(\varepsilon) = \left[\frac{r}{\psi} \frac{d\psi}{dr} \right]_{r=S} \quad (2.9)$$

with

$$\psi(D) = \psi + \omega(D)\dot{\psi} \quad (2.10)$$

and ω given by,

$$\omega(D) = -\frac{\psi(S) D - D(\psi)}{\dot{\psi}(S) D - D(\dot{\psi})}. \quad (2.11)$$

When ψ and $\dot{\psi}$ are calculated at a reference energy E_ν the wavefunction is first order in energy $E(D) - E_\nu$, the second order in energy is $E_\nu + \omega(D)$ and the variational estimate of third order in energy is,

$$E(D) = -\frac{\langle \psi(D) | H | \psi(D) \rangle}{\langle \psi(D) | \psi(D) \rangle} = E_\nu + \frac{\omega(D)}{1 + \omega(D)^2 \langle \dot{\psi}(D) | \dot{\psi}(D) \rangle}. \quad (2.12)$$

The LMTO method builds upon the properties of muffin-tin orbitals, which was introduced by Andersen (cite) in 1971 to provide a satisfying interpretation of the electronic structure of materials with a minimal basis of localized augmented orbitals. In addition, the LMTO method should coincide with the linear limit of the KKR method, which is beyond the scope of these notes. In general a linearized equation for muffin-tin orbital basis can be written from the above equations 2.7-2.12.

$$\chi_j(\mathbf{r}) = \chi_j^e(\mathbf{r}) + \sum_{L,s} \left[\psi_{l,s}(\mathbf{r} - \tau_s) \Pi_{Lsj} + \dot{\psi}_{l,s}(\mathbf{r} - \tau_s) \Omega_{Lsj} \right] i^l Y_L(\widehat{\mathbf{r} - \tau_s}). \quad (2.13)$$

Here ψ and $\dot{\psi}$, the energy derivative, are the radial part of the wavefunctions in the muffin-tins, and Π and Ω are factors to be determined. $Y_L \equiv Y_l^m$ and for each

atom s at origin τ_s . The function χ_j^e describes the interstitial region between the MT's and from here one can describe the LAPW method with plane waves or the LMTO method with a sum of Neumann or Hankel functions. Let us continue with the description of the LMTO method and we will continue later with a comparison of the FLAPW method later on. In the LMTO method the envelope function is described by the energy ε and the constant decay function κ . Inside the muffin-tin for a fixed value of κ the basis functions are a linear combination of ψ and $\dot{\psi}$ at $\varepsilon = E_\nu$. This is formally written as,

$$\chi_L^{LMTO}(\mathbf{r}) = i^l Y_L \begin{cases} \psi_l(\varepsilon, r) + \kappa \cot(\eta_l(\varepsilon)) J_l(\kappa r), & r < S, \\ \kappa N_l(\kappa r), & r > S. \end{cases} \quad (2.14)$$

functions J_l and N_l play an analogous role to the Bessel and Neuman functions j_l and n_l for MTO when $\kappa=0$. Eq. 2.14 leads to an energy-independent basis function when $\varepsilon = E_\nu$ because the energy derivative of $\chi_L^{LMTO}(\varepsilon, \mathbf{r}, \kappa)$ vanishes at the muffin-tin boundary S . With the augmented Neumann functions N_L defined in terms of n_l the LMTO basis functions is a linear combination of ψ and $\dot{\psi}$, in the muffin tin and continuing smoothly in the interstitial region and joining smoothly to $\dot{\psi}$ in each neighboring MT.

To simplify we set $\kappa = 0$ the w.f. in the MT are chosen to match the interstitial solution $\propto (r/S)^{-l-1}$. This is accomplished for $r < S$ for radial w.f. with $\psi(D = -l - 1, r) \equiv \psi_{l-}(r)$ and for w.f. from other MT overlapping onto the original MT $\psi(D = l, r) \equiv \psi_{l+}(r)$ and of course with proper normalization. We can then define an energy independent LMTO orbital with a smooth continuation into the interstitial

as,

$$\chi_{L,\mathbf{k}}^{LMTO}(\mathbf{r}) = \frac{\psi_{L-}(\mathbf{r})}{\psi_{l-}(S)} - \frac{1}{\psi_{l+}(S)} \sum_{L'} \psi_{L'}(\mathbf{r}) \frac{1}{2(2l'+1)} S_{LL'}(\mathbf{k}). \quad (2.15)$$

The orbital contains effects of neighbors through the structure constants $S_{LL'}(\mathbf{k})$ that depend on the crystal environment and are constant κ and do not depend on ε , which is in contrast to the KKR method.

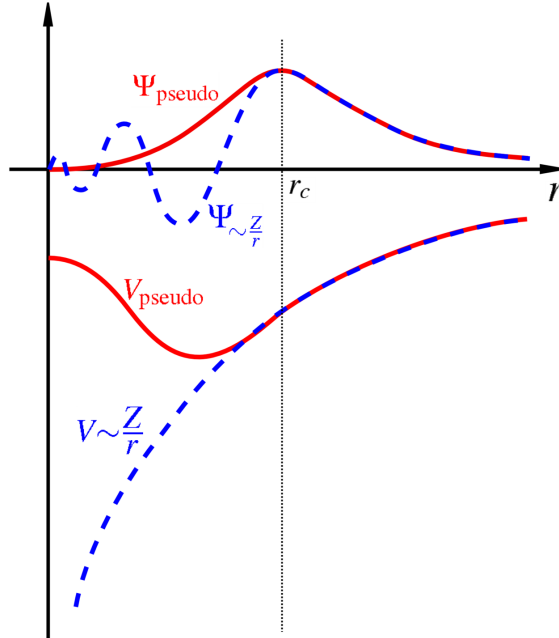


Figure 2.1: Comparison of a wavefunction in the Coulomb potential of the nucleus (blue) to the one in the pseudo-potential (red). The real and the pseudo wavefunction and potentials match above a certain cutoff radius.

2.2.2 (F)LAPW

Now let us briefly discuss the basis functions for the LAPW method. This is achieved by choosing plane waves for the envelope functions in the interstitial. The

basis functions take the form,

$$\chi_{\mathbf{K}_m}^{LAPW}(\mathbf{r}) = \begin{cases} \sum_{Ls} C_{Ls}(\mathbf{K}_m) \psi_{Ls}(D_{lsK_m}, \mathbf{r}) i^l Y_L(\widehat{\mathbf{r} - \tau_s}) & r < S, \\ e^{i\mathbf{K}_m \cdot \mathbf{r}}, & r > S. \end{cases} \quad (2.16)$$

with similar notation in the LMTO basis $\mathbf{K}_m = \mathbf{k} + \mathbf{G}_m$ where \mathbf{G}_m are the reciprocal lattice vectors for $m = 0, 1, 2, 3, \dots$. Also $K_m = |\mathbf{K}_m|$. The coefficients C_{Ls} are found by forcing a boundary condition at $r = S$ that the wavefunction and its first derivative are continuous from the solution in the MT to the plane wave. This leads to $\psi_{Ls}(D_{lsK_m}, \mathbf{r})$ as a function of the wave function and its derivative including an energy dependence to first order without increasing the size of the basis. D_{ls} is the usual logarithmic derivative at the MT boundary and fixes the solution inside the sphere for given values of L and \mathbf{K} as in Eq. 2.10.

Lastly let us give a general overview of the pseudo-potential method (see Fig. 2.1). The main idea of the pseudo-potential method is to simulate the effect of the strong Coulomb potential with an effective ionic potential describing the core electrons and acting on the valence electrons. This approximation is valid when the core states in the nucleus remain relatively unchanged by the valence states. In practice most pseudo-potential codes use plane wave in the interstitial region.

2.2.3 DFT Method Rankings

Let us now list the strength of the DFT methods from the strongest to the weakest. However, a caveat, is that any of these methods can give you meaningful or meaningless results and it quite depends on the user's understanding of the problem at task.

1. **FLAPW** The Full-potential LAPW with all electron basis set is the strongest of the methods and most cumbersome. In contrast to the LAPW here there is a full non-spherical potential in the MT and spatially varying potential in the interstitial. There are no approximations on the wavefunctions or the potential except for truncations at l_{max} and G_{max} . In practice large values of l_{max} are need for accurately satisfying the continuity conditions. The most relevant codes that use this method are ELK, FLEUR (spin-spiral), and WIEN2K.
2. **PP** There are many ways to approximate pseudo-potentials such as Ultra-soft and PAW but much less of a reproducible method and requires ingenuity and expertise in developing accurate potentials. This method offers a large speed up compared to the FLAPW method. When accurate PP are used it gives good results for relaxations making use of the Born-Oppenheimer approximation and that the nucleus is inert. Many pseudo-potentials can include relativistic effects. The most relevant codes that use this method are ABINIT, CASTEP (good reproduction of full potential), GPAW, Quantum Espresso, VASP (most robust, spin-spiral).
3. **LCAO** The localized atomic-(like) orbitals provides a basis that captures the essence of the atomic like features of molecules and solids which provide a localized description of the electronic structure. This method is close to a tight-binding picture is widely used in molecular calculations. Many of the codes have inputs for NEGF transport. The most relevant codes that use this method are OpenMX, SIESTA (NEGF transport included), QuantumWise (nearly the same as SIESTA, transport much more developed)
4. **LMTO** The fastest of the methods and one of the least accurate. This method is interchangeable with the above (3). The LMTO method can also be approx-

imated to include the full potential method. In addition the code is suitable for electronic structure calculations of large systems with much smaller basis sets and requiring small l_{max} . In construction this code is most similar to method one the FLAPW. There are many version of the TB-LMTO code, however they all stem from the original of Ole Andersen.

2.3 Spin-Orbit Coupling in DFT

One of the more necessary interactions in this dissertation is the spin-orbit interaction. Spin-orbit coupling (SOC) is necessary for the anomalous Hall effect in collinear ferromagnets (see 3.13). In magnetic systems that break inversion symmetry the Dzyaloshinskii-Moriya interaction (DMI) is allowed and is first order in SOC (see 3.2.2). The DMI plays a large role in the stabilization of non-collinear magnetic textures, e.g. skyrmions (see 1.1). Lastly, the magneto-crystalline anisotropy energy is a second order effect in SOC, causing magnetic structures to orient in a high symmetry direction.

The spin-orbit interaction stems from relativistic physics, and becomes increasingly important with heavier nuclei due to high kinetic energy of the electrons in the proximity of the nucleus. One of the great success's of DFT is the inclusion of the Dirac-equation [95] which gives a relativistic density-functional theory. In this section, we simply show how to obtain the relativistic correction to the Pauli equation [124] starting from the Dirac equation. For a more extensive and complete review the reader is directed towards the works of Sinova [147] and Winkler [172]. The Dirac equation for an electron in an external potential reads:

$$\{c\boldsymbol{\alpha} \cdot \mathbf{p} + \frac{1}{2}\beta c^2 + V_{ext}(\mathbf{r}) + \mathbf{B}_{xc} \cdot \boldsymbol{\sigma}\}\Psi_{\nu}(\mathbf{r}) = E_{\nu}\Psi_{\nu}(\mathbf{r}). \quad (2.17)$$

In the above equation: c is the speed of light, \mathbf{p} is the momentum operator, V_{ext}

is the external potential as described in the previous sections, \mathbf{B}_{xc} is the exchange-correlation field. Here the relativistic energy $E_\nu = \epsilon_\nu + 1/2c^2$ is the kinetic energy plus the rest energy. The vector of Pauli spin-matrices is denoted by $\boldsymbol{\sigma}$. The wavefunction, Ψ_ν , is a four component spinor with

$$\boldsymbol{\alpha} = \begin{pmatrix} 0 & \boldsymbol{\sigma} \\ \boldsymbol{\sigma} & 0 \end{pmatrix}, \quad (2.18)$$

$$\boldsymbol{\beta} = \begin{pmatrix} \mathbb{1} & 0 \\ 0 & -\mathbb{1} \end{pmatrix}. \quad (2.19)$$

Here $\mathbb{1}$ is a 2×2 identity matrix. The four component spinor can be separated into two parts each with two spins, the large and small component.

$$\Psi_\nu = \begin{pmatrix} \varphi_\nu \\ \chi_\nu \end{pmatrix}, \quad \varphi_\nu = \begin{pmatrix} \varphi_\nu^\uparrow \\ \varphi_\nu^\downarrow \end{pmatrix}, \quad \chi_\nu = \begin{pmatrix} \chi_\nu^\uparrow \\ \chi_\nu^\downarrow \end{pmatrix}. \quad (2.20)$$

In systems with a larger atomic numbers, it becomes increasingly more crucial to fully solve the relativistic Dirac equation (see Eq. 2.17). However, in the B20 compounds of interest it is sufficient to solve the non-relativistic KS equation (see Eq. 2.3) with relativistic corrections in a $\frac{1}{c^2}$ -expansion of the full Dirac equation [8]. This leads to a computationally simpler matrix to diagonalize, which scales to the third power. The KS equation takes a new form,

$$\mathcal{H}_{rel}\phi_\nu = \epsilon_\nu\phi_\nu. \quad (2.21)$$

One can write the small and large component spinors in terms of the spinor wavefunction, ϕ_ν , as

$$\varphi_\nu = \left(1 - \frac{1}{2c^2}\mathbf{p}^2\right)\phi_\nu + \mathcal{O}(c^{-4}), \quad (2.22)$$

$$\chi_\nu = \left(\frac{1}{c}(\boldsymbol{\sigma} \cdot \mathbf{p}) + \frac{1}{c^3}\left(-\frac{\mathbf{p}^2}{2} + V - \epsilon_\nu\right)(\boldsymbol{\sigma} \cdot \mathbf{p})\right)\phi_\nu + \mathcal{O}(c^{-5}) \quad (2.23)$$

With the relativistic corrections the Hamiltonian takes the form,

$$\begin{aligned} \mathcal{H}_{rel} = \mathcal{H}_{KS} + \frac{1}{c^2} & \left(-\mathbf{p}^4 \mathbb{1} + \frac{1}{2}(\nabla^2(V_{eff}\mathbb{1} + \boldsymbol{\sigma} \cdot \mathbf{B}_{xc})) \right) \\ & + \frac{1}{c^2}\boldsymbol{\sigma} \cdot ((V_{eff}) \times \mathbf{p}) + \frac{1}{c^2}\underline{\mathbf{B}}. \end{aligned} \quad (2.24)$$

The last term containing $\underline{\mathbf{B}}$ is a 2×2 matrix that is small compared to other corrections and is usually neglected. The first part of the Hamiltonian, \mathcal{H}_{KS} , is the non-relativistic hamiltonian discussed in section 2.1.2. The second term includes the mass-velocity and Darwin contributions which are invariant for rotations in spin space [94]. These terms are included in the scalar-relativistic approximation, where nearly every DFT code takes into account at the lowest level.

The next correction is the so-called spin-orbit coupling [81] and is written as,

$$\mathcal{H}_{SO} = \frac{1}{c^2}\boldsymbol{\sigma} \cdot ((V_{eff}) \times \mathbf{p}). \quad (2.25)$$

Contrary to the other terms, \mathcal{H}_{SO} is not invariant for rotations in spin space. This term contribution is substantial for large gradients where atomic number is large and in the proximity of the nucleus. In the vicinity of the nucleus one can approximate the potential as spherical,

$$\nabla V(\mathbf{r}) \approx \sum_{\mu} \frac{\partial \tilde{V}(r^\mu)}{\partial r^\mu} \frac{\mathbf{r}^\mu}{r^\mu}, \quad (2.26)$$

here $\tilde{V}(r^\mu)$ is a spherically averaged potential centered at $\mathbf{r}^\mu = \mathbf{r} - \mathbf{R}^\mu$ for the μ th nucleus in real space coordinates. This leads to an analytic expression for the spin-orbit operator in first principle calculations,

$$\mathcal{H}_{SO} = \sum_{\mu} \xi^{\mu}(r^{\mu}) \boldsymbol{\sigma} \cdot \mathbf{L}^{\mu} = \sum_{\mu} \xi^{\mu}(r^{\mu}) \begin{pmatrix} L_z^{\mu} & L_-^{\mu} \\ L_+^{\mu} & -L_z^{\mu} \end{pmatrix}, \quad (2.27)$$

where $\xi^{\mu}(r^{\mu}) = \frac{1}{c^2 r^{\mu}} \frac{\partial \tilde{V}(r^{\mu})}{\partial r^{\mu}}$ is the spin orbit coupling constant proportional to the atomic number Z and quickly decays as a function of r^{μ} . Lastly, the angular momentum is denoted by \mathbf{L}^{μ} , where L_z^{μ} is the z -component and $L_{\pm}^{\mu} = L_x^{\mu} \pm iL_y^{\mu}$.

In collinear magnets without SOC the spin-quantization axis (SQA) is arbitrarily chosen along the z -axis. When SOC is included, the matrix of Eq. 2.27 must be rotated with a spin-rotation matrix \mathcal{U} . This leads to non-vanishing expectation values of the orbital moments $\langle \mathbf{L}^{\mu} \rangle$.

2.4 DFT Results in B20 Compounds

At the start of this dissertation there were many first principle calculations on B20 compounds. However, most have been for collinear magnetic compounds and insulating compounds with out much attention on Berry-Phase effects. Most of these studies have been on MnSi spin fluctuations in this system [67]. There have been some studies on the pressure-induced phase transitions in FeGe [118, 132]. Also there are studies on the insulating to magnetic phase transition in $\text{FeSi}_{1-n}\text{Ge}_n$ [175]. Until now there has not been any significant study comparing different codes and XC functionals.

In figure 2.2 the crystal structure of the B20 structure is shown with the magnetization direction point perpendicular to the $\langle 111 \rangle$ direction. The figure shows the right and left-handed crystal chiralities of the B20 compound side by side, which are

just mirror images of the each other. From the image it is clear that the system breaks inversion symmetry.

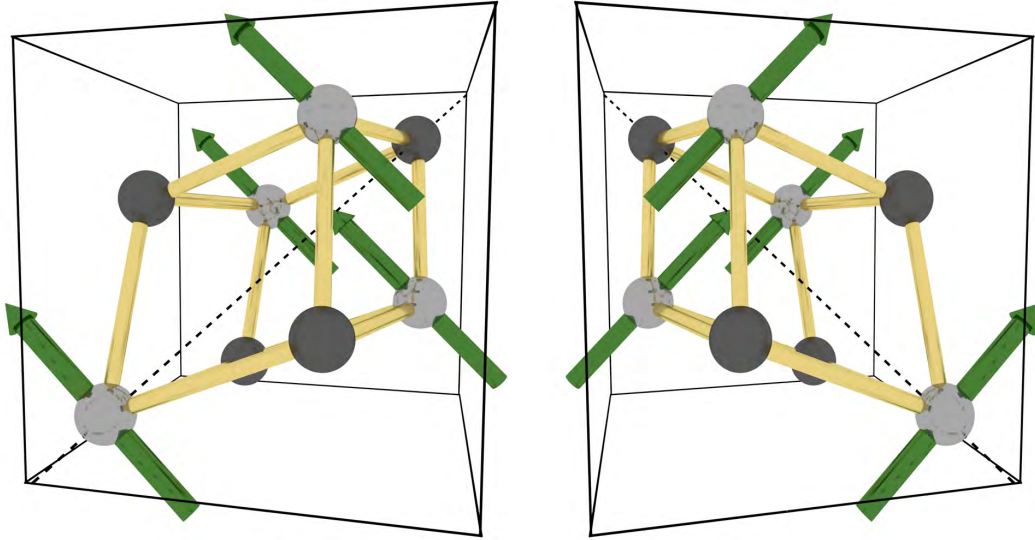


Figure 2.2: Right and left-handed crystal chiralities of the B20 compound. The green arrows show an arbitrary magnetization direction.

In table 2.1 a comparison of four different types of DFT codes are compared for xc-functionals of the LDA and GGA type in the B20 compound FeGe at the experimental lattice constant. In addition, the total energies are compared for differences in the antiferromagnetic and ferromagnetic states. The two magnetic states are compared because they represent different limits for high symmetries of spin-spirals and points in between can be considered as a mixture of the two states.

Firstly, the code that shows the most discrepancies for the B20 compounds is the LCAO of the SIESTA program. In the case of the GGA calculation the code over predicts the total magnetic moment and the moment on the Fe ions. In both the LDA

and the GGA cases of the SIESTA code, the moments on the Fe ion vary drastically on the each of the four transition metal ions in the unit cell. The AFM calculations could not be converged with sufficient accuracy. In the case of the TB-LMTO code the FM calculations reproduce previous computational work [175]. However, the antiferromagnetic calculations results in a non-magnetic state with zero magnetic moment where no fixed-spin-moment restraints were applied, and the energy is relaxed from an initial AFM state.

The calculations of the FM state in the PP code Quantum Espresso and FLEUR show results that agree with previous work [118, 132]. The TB-LMTO and FLEUR codes are nearly exactly the same for the FM moment, which is due to the similar treatment of the muffin-tin core. Whereas in Quantum Espresso the radii of the core potential are smaller, which may lead to smaller moments. The codes differ in the case of the AFM moments. Where the FLEUR code shows the largest moment for the GGA AFM moment. In addition, Quantum Espresso shows that the AFM is a lower energy state for the GGA xc-functional. The most reliable xc-functional

Table 2.1: Magnetic moments in μ_B for the Fe ion and total per bond in the experimental volume. Energy difference between the FM and AFM states.

		$m_{Fe}(m_{tot})$ -FM	$m_{Fe}(m_{tot})$ -AFM	$E_{AFM}-E_{FM}$ (meV)
FLEUR	LDA	1.11 (1.05)	0.20950 (0)	735
	PBE	1.20 (1.14)	1.03 (0)	201
TB-LMTO	LDA	1.13 (1.01)	0	74
	PW91	1.21 (1.06)	0	194
SIESTA	LDA	1.182 (1.08)		
	PBE	1.857 (1.962)		
Quantum Espresso	LDA	1.03 (0.99)	0.03 (0)	94
	PBE	1.0 (0.96)	0.55 (0)	-25
Exp [93]		1		

is the GGA within the FLEUR code. The rest of this dissertation will focus all calculations using this functional, to reproduce experimentally comparable results. The convergence criterion for the FeGe can be found in the appendix.

In figure 2.3 the spin- and orbitally-resolved density of states (DOS) is plotted for several concentrations of $x=0, 0.4, 0.8$ and 1, in $\text{Mn}_{1-x}\text{Fe}_x\text{Ge}$ using the virtual crystal approximation (discussed in the next section). In this figure the FLEUR code is used for collinear magnetic structures without SOC. For all concentrations the orbitally-projected p -states of the Ge ions are shown in purple. In the figure the peaks of the p_x -states (below and above 1 eV) are relatively unchanged with varying concentration. In the B20 compound the p_x, p_y and p_z state hybridize with the d states and show the some DOS, so only one is plotted and multiplied by ten. This can be seen where there are large peaks for the p -states that coincide with that of the d -states. All p states are partially occupied.

In the case of the d states the DOS is projected onto the e_g and t_{2g} states. The e_g are plotted in the dashed blue and the t_{2g} are in solid red. Here with the increase in concentration of x the peaks of the d -states move closer to the Fermi energy. In the case of $x=0.4$ the e_g and t_{2g} strongly hybridize at the Fermi energy. Whereas, in the case of $x=0.8$ the e_g and t_{2g} are separated by the Fermi energy. Lastly in the case of FeGe the two types of d orbitals hybridize below the Fermi energy. The reordering of of states with varying concentration gives some information for why there is a change in the behavior of the Berry-Phase effects.

2.4.1 Alloy Calculations

To capture the effect of alloying we use the virtual crystal approximation (VCA) [10]. Within the all-electron FLPAW method this is done by averaging the fractional atomic charges of two elements at a single site. The total electron density must

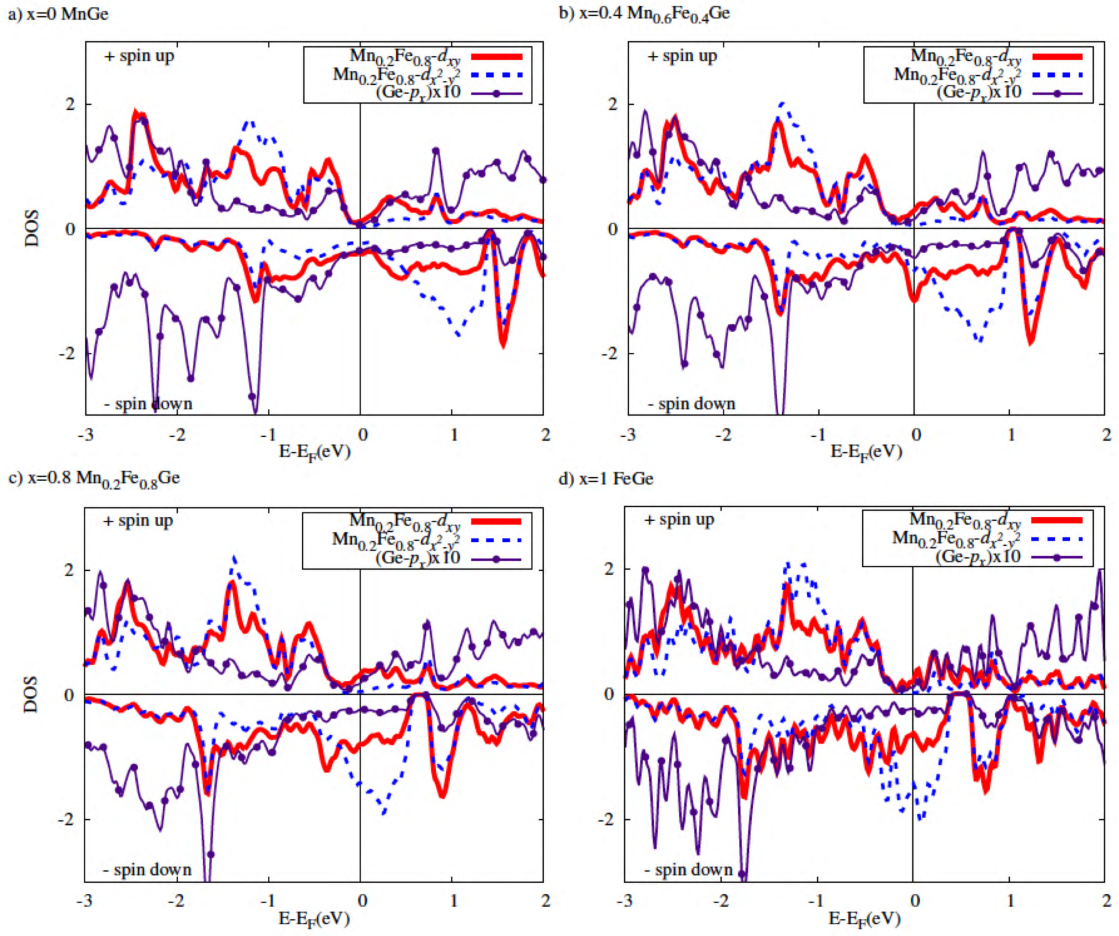


Figure 2.3: First principles collinear ferromagnetic spin- and orbitally-resolved DOS at a given concentration x of a) 0 for MnGe, b) 0.4, c) 0.8, d) 1.0 for FeGe, for the d_{xy} (solid red), $d_{x^2-y^2}$ (dashed blue), and p_x (purple with dots) orbitals, computed without SOC.

equal the total nuclear charge to satisfy a neutral charge environment. Therefore the alloying effectively modifying the electronic structure and Fermi surface topology of two pure B20 compounds into an average effective potential. There are two major disadvantages for this approximation: *i*) The two alloying materials must have the same crystal structure, *ii*) the details of microscopic electron scattering off impurities are not taken into account. Lastly, in all-electron methods due to the averaging of nuclear charges, only neighboring elements make use of the VCA approximation. Pseudo-Potential methods are not limited in this regard, in that any two pseudo-potentials can be averaged. However, in this dissertation we are concerned with smoothly modifying the electronic structure to see the extent the intrinsic Berry curvature changes.

In the pure B20 compounds we take the experimental lattice constants and basis [28]. The lattice constants and positions of the alloy compounds are computed using Vegard's law, i.e. $a_x = \{1-x\}a_1 + \{x\}a_2$. For example, in $\text{Fe}_{1-y}\text{Co}_y\text{Ge}$, a_1 the lattice constant of FeGe and a_2 is that of CoGe where x is exchanged with y . In figure 2.4 we show the comparison of the lattice constant input into the *ab initio*, which is the blue curve. The experimental curve shown in red is the lattice constant for thin film samples prepared by the group in Leeds. The bottom curve shows the calculated and measured magnetic moment per formula unit. The thin films show a discrepancy of the lattice constant with that of the calculations in the Fe rich side. We attribute this behavior to the thickness of the thin films. Where the *ab initio* lattice constant taken from bulk experimental results [28], using the Vegard's lattice constant.

The results for figure 2.4 assures computationally accurate results for the use of the VCA approximation and Vegard's law in alloyed B20 compounds. In figure 2.6 the FM (blue closed square) and AFM (red open square) moment in $\text{Cr}_{1-w}\text{Mn}_w\text{Ge}$, $\text{Mn}_{1-x}\text{Fe}_x\text{Ge}$, $\text{Fe}_{1-y}\text{Co}_y\text{Ge}$ is plotted in the top graph as a function of alloying. The

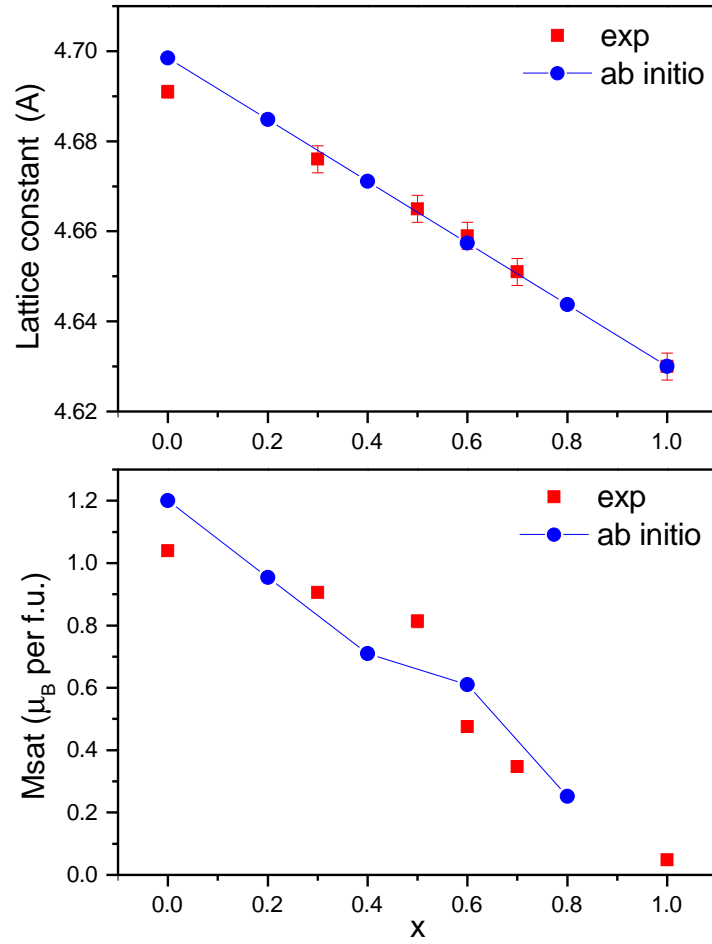


Figure 2.4: *top* *Ab initio* input of the lattice constant in $\text{Fe}_{1-y}\text{Co}_y\text{Ge}$ compared to thin film measurements (red) of the lattice constant. *bottom* Comparison of magnetic moment per formula unit (f.u.) for *ab initio* and experiment.

bottom curve shows the energy difference (green closed square) of the AFM and FM state. In addition, we include the DFT results for that of MnSi shown in circles. The upper graph shows a smooth behavior of the magnetic moment for the concentration w of Mn ions in CrGe, x of Fe ions in MnGe, and y of Co ions in FeGe.

In figure 2.5 the collinear band structure of three concentrations in $\text{Mn}_{1-x}\text{Fe}_x\text{Ge}$ without SOC is compared of $x=0.1$, 0.8 and 0.9. These concentrations are shown, because $x=0.1$ and 0.9 are close to the pure concentrations of MnGe and FeGe respectively. The concentration at $x=0.8$ is where experimentalists see a transition in the magnetic properties of $\text{Mn}_{1-x}\text{Fe}_x\text{Ge}$ [145, 49]. In the figure the concentration at $x=0.8$ is plotted for the majority (maj) in solid blue and the minority (min) in solid green. In the top (bottom) graph the collinear band structure is plotted for $x=0.1$ (0.9) with the majority as dashed black and the minority as dashed red.

In figure 2.5 the energy range is only from -2 eV to + 2 eV to emphasize the change around the Fermi energy. In the top graph the minority channel is shifted nearly a half of an eV up above the Fermi energy comparing the green solid bands (0.8) to that of the red dashed bands (0.1). This is clearly seen at the high symmetry point of $\mathbf{k} = \text{R}$. In addition, comparing the majority bands blue (0.8) and black (0.1) there is a shift upwards of nearly 50 meV at the high symmetry point of $\mathbf{k} = \text{R}$. On the contrary the bottom curve shows the minority channel shifts down slightly, where as the majority curve also shifts up as in the previous comparison. From the actual calculations, there is not only a rigid shift of the bands, but in addition the curvature of the bands change.

The Stoner model is one the simplest models to describe ferromagnetism in a single-particle picture [100, 99]. Although ferromagnetism arises from the electron-electron interactions, in a single-particle band picture ferromagnetism is energetically favored over paramagnetism when the density of states, $g(E_F)$, causes an increase

in the energy for the electrons to move from one spin channel to the other. The Stoner model is written as $E(k)_{\uparrow,\downarrow} = \varepsilon(k) \pm I \frac{N_{\uparrow} - N_{\downarrow}}{N}$, where I is the Stoner parameter, $\frac{N_{\uparrow}}{N}$ ($\frac{N_{\downarrow}}{N}$) is the spin up (down) density and $\varepsilon(k)$ is the spin-less dispersion relation. When $Ig(E_F) > 1$ the system prefers a polarized state. In $\text{Mn}_{1-x}\text{Fe}_x\text{Ge}$ we see that the Stoner parameter is approximately 1 eV for all concentrations of x . This leads to the fact that the change in magnetism in these systems is due to the electronic density of states at the Fermi energy.

The results in $\text{Mn}_{1-x}\text{Fe}_x\text{Ge}$ show the largest magnetic moments and the most monotonous behavior of the magnetic moment as a function of concentration. Experimentally, the $\text{Mn}_{1-x}\text{Fe}_x\text{Ge}$ are known to be ferromagnetic helimagnets with some of the highest transition temperature from an ordered magnetic state to a paramagnetic state [145]. Both CrGe and CoGe are paramagnetic in the ground state [28]. However, the first principle calculations in CrGe show a ferromagnetic ground state at the experimental volume. The paramagnetic ground state is recovered in the *ab initio* minimal volume. An interesting feature of this curve is where the antiferromagnetic moment is larger than that of the ferromagnetic moment for $\text{Cr}_{0.4}\text{Mn}_{0.6}\text{Ge}$. To understand this better we can look for the exchange interactions in these systems.

Within the simplest MFA [96] we can calculate the Curie temperature as $T_c = \frac{2}{3k_B} J_0$. As can be seen in the bottom graph of figure 2.6 the plotted green curve of $J_0 = E_{AFM} - E_{FM}$ should give information on the magnetic ordering of these materials. Using this approximation we can calculate J_0 for MnSi, MnGe and FeGe to be 4 meV, 22 meV and 36 meV for the experimental T_C of 29.5, 170 and 278.2 K respectively. It can be seen at this level of approximation that the experimental results differ from the computational results in figure 2.6 by orders of magnitude. The failure of this MFA is due to the *i*) treating the four magnetic sub-lattices as one, *ii*) treating the system as ferromagnetic *iii*) more specifically in MnSi there

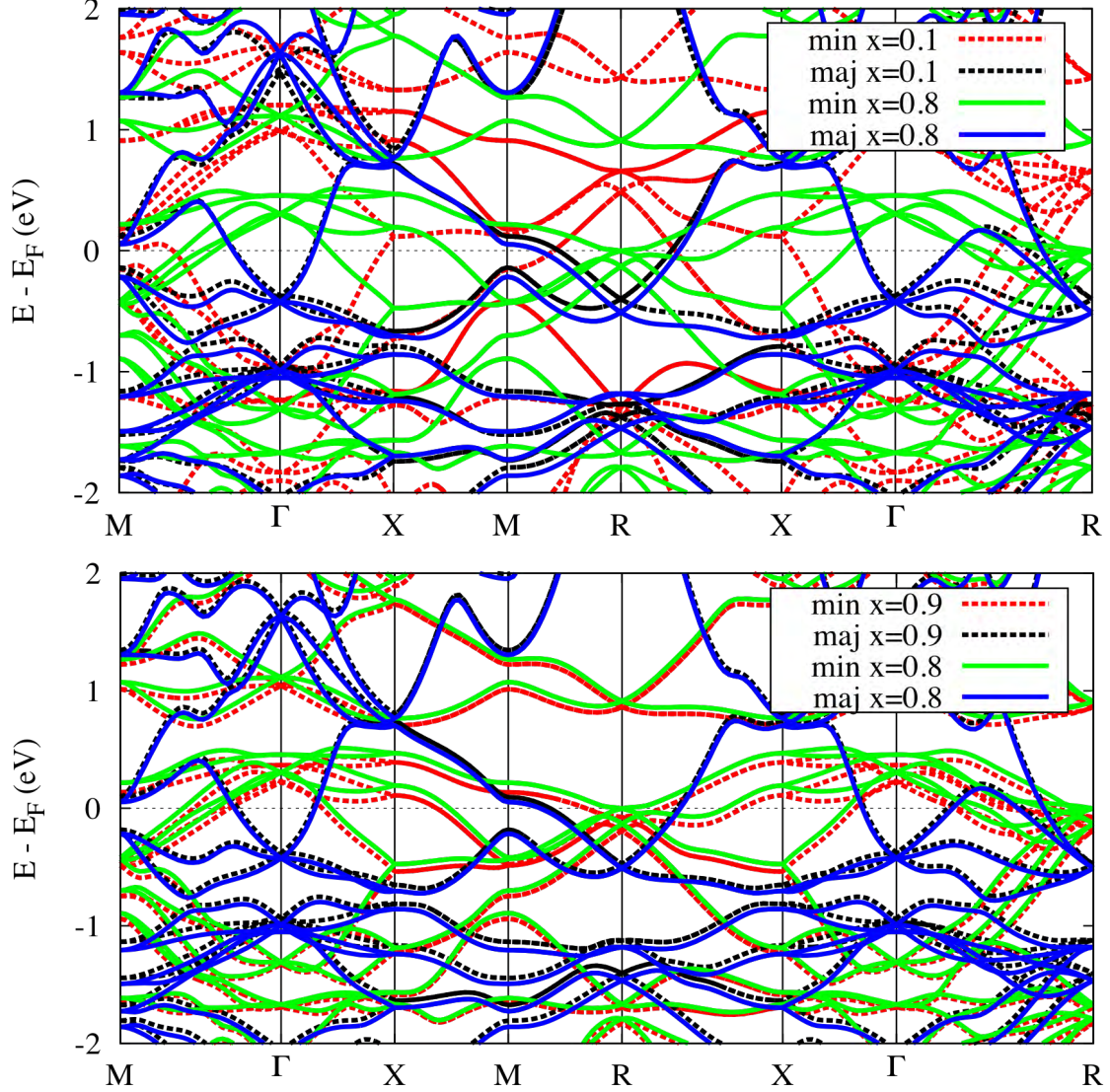


Figure 2.5: *Top* Collinear ferromagnetic *ab initio* band structure comparison in $\text{Mn}_{1-x}\text{Fe}_x\text{Ge}$ with $x=0.1$ and $x=-0.8$ using the VCA approximation for the majority (maj) and minority (min) spin channels. *Bottom* Collinear ferromagnetic *ab initio* band structure comparison in $\text{Mn}_{1-x}\text{Fe}_x\text{Ge}$ with $x=0.9$ and $x=-0.8$ using the VCA approximation.

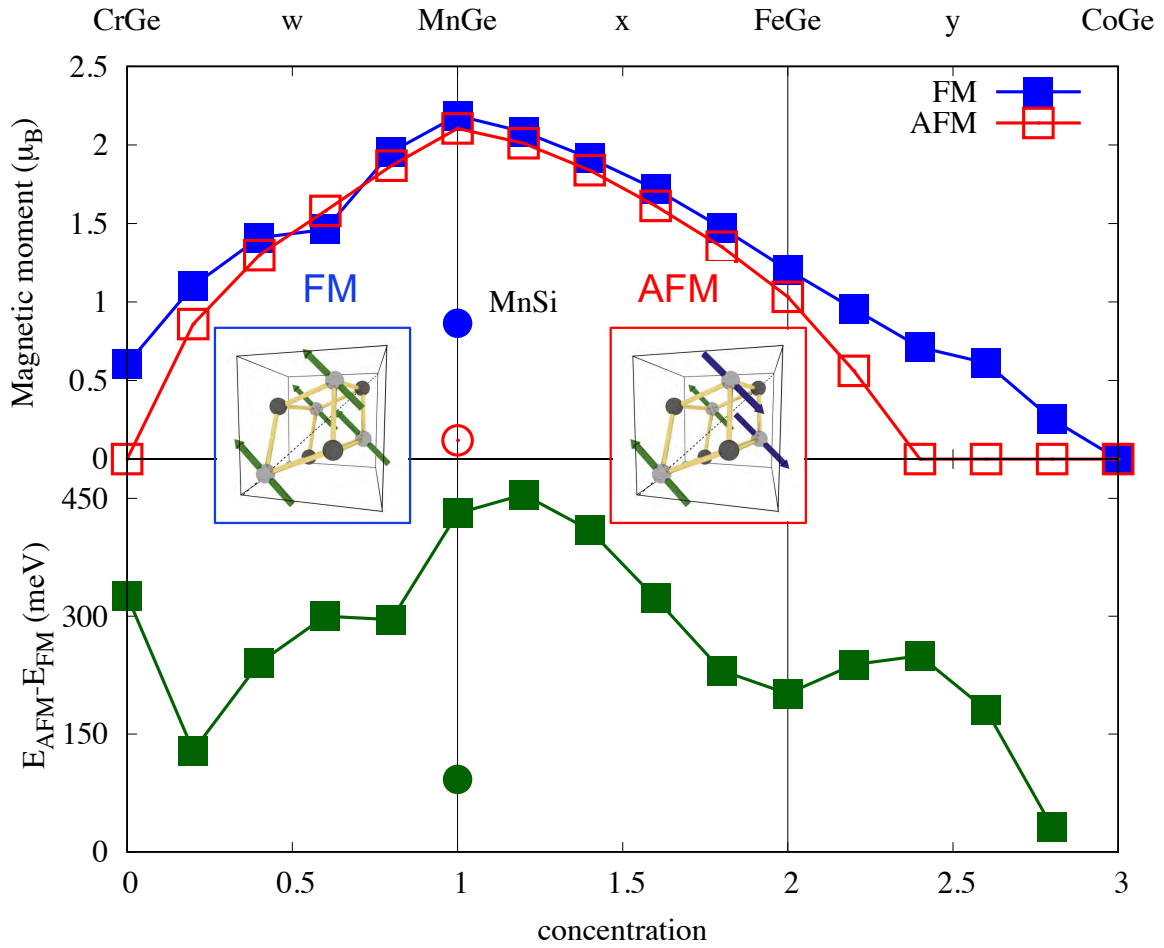


Figure 2.6: *Top* VCA calculations of the FM (blue closed) and AFM (red open) of $\text{Cr}_{1-w}\text{Mn}_w\text{Ge}$, $\text{Mn}_{1-x}\text{Fe}_x\text{Ge}$, $\text{Fe}_{1-y}\text{Co}_y\text{Ge}$ magnetic moment shown as squares and that of MnSi shown as circles. *Bottom* Difference in energy of the AFM and FM state.

moments in the first principle calculations are predicted to be $0.9 \mu_B$ as compared to the experimental value of $0.4 \mu_B$.

In the first case the, we only take the simplest MFA approximation, which works well for simple cubic compounds such as Iron, Nickel, and Cobalt [96]. However, already at this level the MFA approximation overestimated the T_C compared to that of the experiment. In the B20 compounds there are 4 magnetic sub-lattices (see Fig. 2.6), which is not taken into account for this level of the MFA. One can take into account the multiple sub-lattices [5, 24, 25] in calculating the T_C , however this still gives a miss representation of the magnetic ordering temperature as can be seen for calculations in MnSi [63]. This can be remedied by taking into account spin-spiral solutions as the ground state of the B20 compounds, which is the solution to the second failure of the MFA. This can be taken into account in the random phase approximation (RPA) which is discussed in the following section [165, 35]. Lastly, as discussed earlier in MnSi the spin fluctuations cause the magnetic moment to be smaller experimentally [67], which will not be discussed in this dissertation.

2.4.2 Spin-Orbit Coupling in B20 Compounds

In figure 2.7 the orbital projected bands are plotted for FeGe (MnGe) on the left (right). The red (blue) circles shows states mostly with d (p) character. In the calculations, the SQA is along the [001] direction. The size of the circles is determined by the strength of the spin-orbit interaction which is multiplied by 15 to enhance the quality of the graph.

In the figure one can see in both band structure plots that around ± 2 eV around the Fermi energy that the d -states give the largest contribution. The d -states are directly due to the transition metal ions Fe and Mn. The occupied p -states in red lie below the Fermi energy from -7 eV to -2 eV, which is due to the Ge ions. Below

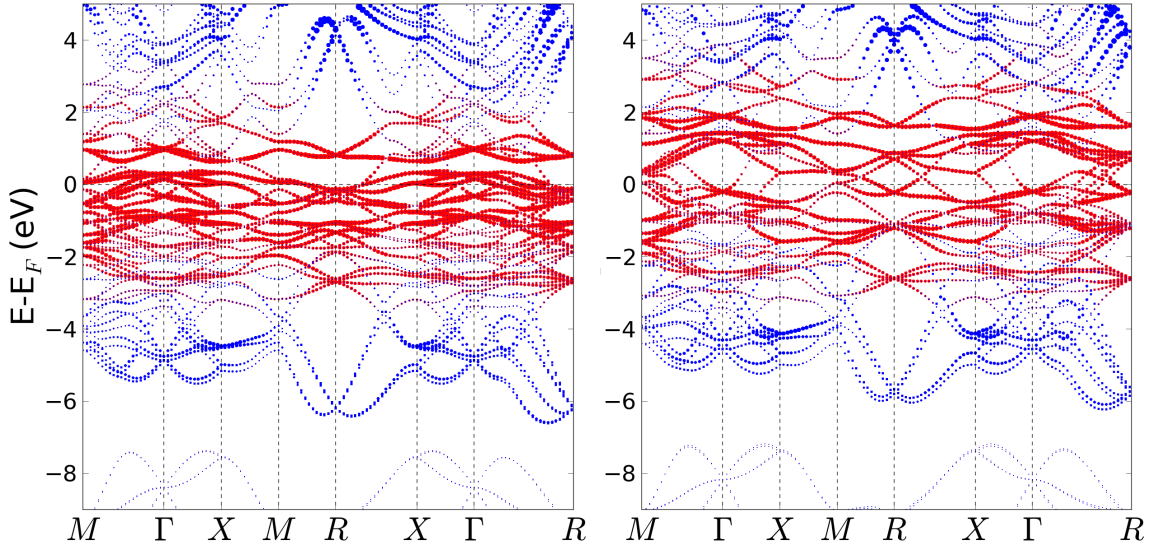


Figure 2.7: *Left* Orbital projected bands of FeGe with SOC. *Bottom* Orbital projected bands of MnGe with SOC. The red (blue) circles show the d (p) character of the bands and the size of the circles show the amount of the $\text{SOC} \times 15$.

-7 eV there is a gap between the occupied p -states and the s -states of the Ge ions, where the s -states do not have any SOC contribution. However, there is some small hybridization of the s and p -states. Above the Fermi energy there are also unoccupied p -states from the Ge ions that hybridize with the d -states of the transition metal ions. This can be seen on some bands that are colored both red and blue at certain points in the Brillouin zone.

Most of the effects due to spin-orbit coupling determined by Berry-phases are determined by the Fermi occupation (see 3.11). In figure 2.7 one can see that band structures of the two pure B20 compounds MnGe and FeGe, show many resemblances. This can especially be seen at the high-symmetry point R . MnGe has four less electrons than FeGe, so there are more unoccupied d -states for the transition metal ion. From the previous section, the affect of alloying would *effectively* shift the bands and hence change the Fermi surface. From figure 2.5 the minority states

have the largest shift causing a change in the number of crossing points with SOC around the Fermi energy. Around the high-symmetry point R there is only one crossing point in MnGe of the majority state, where in FeGe there is a mixture of crossing points for minority and majority states. However, simply looking at the band structure does not tell the full story of the Berry-phase effects and this will be discussed in more detail in section 3.11. Lastly, it is important to note the effects of

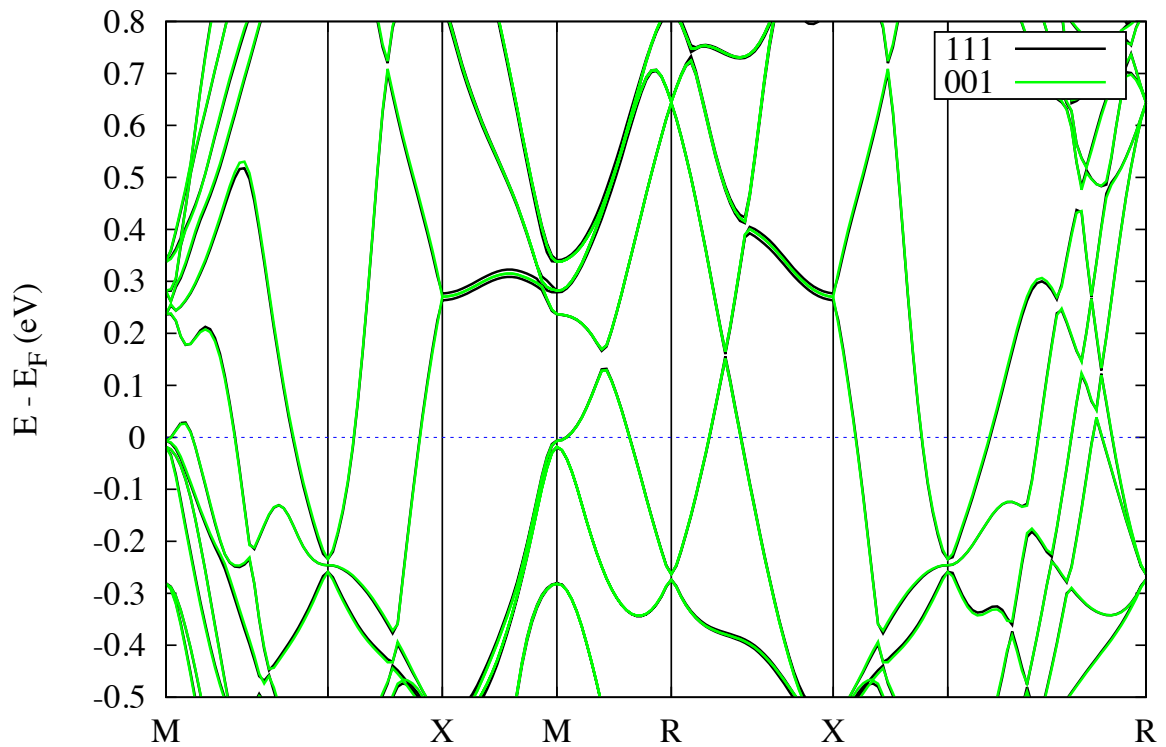


Figure 2.8: Band structure of MnGe with SOC for the SQA in the 001 (green) and the (111).

the choice of the SQA has on the band structure. In figure 2.8 the band structure of MnGe is plotted in a small energy window (-0.5–0.8 eV) around the Fermi energy for the SQA along the [001] and the [111] directions, in green and black respectively.

Here it is seen that there are very small differences in the band structure for the different directions. In addition, at the Fermi level there is little to no difference in the eigenenergies of the band structure. The small difference is due to the cubic symmetry of the B20 compound, where the cubic directions $\langle 100 \rangle$, $\langle 110 \rangle$ and $\langle 111 \rangle$ display the lowest total energies. For the SQA along these high-symmetry directions the total energy difference is on the order of $1 \mu\text{eV}$, which is beyond the accuracy of the DFT method.

The usual method to calculate the magnetocrystalline anisotropy is to take the difference in energies of two magnetic directions [21]. In section 3.1.4 the magnetocrystalline anisotropy will be discussed in more detail. In the next section we will also discuss the Heisenberg interactions in respect to DFT calculations.

3. HEISENBERG INTERACTIONS AND NON-COLLINEAR MAGNETISM

Non-collinear magnetism arises in many forms and from many types of interactions. In some cases it arises due to frustration of the lattice or reduction of the dimension of the lattice. It can be caused by finite temperature effects producing spin waves. In other cases it is due to the competition of exchange interactions. For instance, if the exchange interaction of the first and second nearest neighbor are of the same order with different sign, this may cause a twisted helicoidal state [26]. This work is interested in long wavelength non-collinear spin states caused by the interaction of the exchange interaction and the DMI. *

3.1 Classical Spin Hamiltonian

Here, we are interested in the classical ground state of a spin Hamiltonian of the form,

$$\mathcal{H} = \mathcal{H}_{exch} + \mathcal{H}_{ani} + \mathcal{H}_{app} \quad (3.1)$$

Where \mathcal{H}_{exch} is the exchange energy \mathcal{H}_{ani} is the anisotropy energy and \mathcal{H}_{app} is the due to applied fields. This Hamiltonian captures the essential physics of spin interactions at an atomic scale without non-magnetic effects. The dominant term in the Hamiltonian is \mathcal{H}_{exch} , due to the symmetry of the electronic wave function and the Pauli exclusion principle, where it gives the energy between relative orientations of two Heisenberg linked spins. The typical interactions scale of these energies are on the order of electron Volts and orders of magnitude larger than the next largest contributions. The exchange interaction dominates the magnetic ordering temperature.

*Reprinted with permission from "Dzyaloshinskii-Moriya Interaction and Hall Effects in the Skyrmion Phase of $Mn_{1-x}Fe_xGe$ " J. Gayles, F. Freimuth, T. Schena, G. Lani, P. Mavropoulos, R. A. Duine, S. Blügel, J. Sinova, and Y. Mokrousov. Physical Review Letters, 115(3):1-6, 2015. Copyright 2016 by Copyright Clearance Center

3.1.1 Symmetric Exchange

The exchange interaction dominates the magnetic ordering temperature. The symmetric exchange described in Eq. 3.3 is due to the direct exchange energy of two electronic wave functions being interchanged for two atomic sites. For two atomic sites the energy only decreases when the exchange energy decreases the total energy of the system. In metallic systems the exchange interactions is mediated by the itinerant electrons over large distances, which is commonly referred to as the RKKY interaction [139, 74, 178]. There are other forms of exchange that cause magnetic ordering, i.e. double [180] or super exchange [86, 4] which is not the case in the B20 compounds. For the helimagnetic systems of study in this dissertation the symmetric exchange is the leading term to cause magnetic ordering. With the exception of CrGe and CoGe which have paramagnetic ground states. The form of the exchange interactions is,

$$\mathbf{J}_{ij}^M = \begin{bmatrix} J_{xx} & 0 & 0 \\ 0 & J_{yy} & 0 \\ 0 & 0 & J_{zz} \end{bmatrix}, \quad (3.2)$$

and the Hamiltonian,

$$\mathcal{H}_{exch} = - \sum_{i \neq j} J_{ij} \mathbf{S}_i \cdot \mathbf{S}_j \quad (3.3)$$

where J_{ij} is the exchange interaction linking atomic sites i and j for the atomic spin $\mathbf{S}_{i,j}$. The sign of J_{ij} determines the preferential alignment of linked spins where $J_{ij} > 0$ is ferromagnetic (FM) and $J_{ij} < 0$ is antiferromagnetic (AFM).

In principle J_{ij} can extend to many distance of \mathbf{r}_{ij} but quickly drops off due to the RKKY interaction. In many simple cases J_{ij} takes the form of an isotropic

interaction,

$$J_{ij}^M = \begin{bmatrix} J & 0 & 0 \\ 0 & J & 0 \\ 0 & 0 & J \end{bmatrix} \quad (3.4)$$

Due to the cubic symmetry of the B20 compounds, the exchange interaction does take this form for cubic directions along $\langle 100 \rangle$ planes. However the exchange for the $\langle 100 \rangle$, $\langle 110 \rangle$ and $\langle 111 \rangle$ planes is anisotropic as expected. Due to the weak crystalline anisotropy energy of these compounds, one can simply rotate the magnetic ordering in different planes with an external magnetic field.

3.1.2 Antisymmetric Exchange

However the exchange interaction can be more complex and take into account anisotropic terms and antisymmetric terms (Dzyaloshinskii-Moriya interaction or DMI) which is also anisotropic in our systems for different sets of crystal planes. The full tensor for the exchange interaction will then take the form,

$$\mathbf{J}_{ij}^M = \begin{bmatrix} J_{xx} & J_{xy} & J_{xz} \\ J_{yx} & J_{yy} & J_{yz} \\ J_{zx} & J_{zy} & J_{zz} \end{bmatrix} \quad (3.5)$$

Here the DMI is represented by the off-diagonal terms such as $D_z = 1/2(J_{xy} - J_{yx})$ and the interaction energy, $\mathcal{H}_{DMI} = \mathbf{D}_{ij} \cdot (\mathbf{S}_i \times \mathbf{S}_j)$ preferring spins to point perpendicular on connecting sites. The DMI arises in magnetic systems breaking inversion symmetry that also include spin-orbit coupling. Recently, it has been noted as a crucial interaction to stabilize chiral structures, more specifically skyrmions. In

general, The DMI is a tensor with a directional preference,

$$\mathbf{D}_{ij}^M = \begin{bmatrix} 0 & D_z & D_y \\ -D_z & 0 & D_x \\ -D_y & -D_x & 0 \end{bmatrix}_{ij} \quad (3.6)$$

The DMI gives a chiral ground state and when coupled with a strong Heisenberg interaction a long wavelength spin-spiral is expected. There are many ways to calculate the DMI from first-principle calculations such as the spin-cluster expansion technique [154, 30] or the relativistic torque method [92, 33]. We make use of *ab-initio* methods to calculate D along the $\hat{e}_{[111]}$ direction (discussed in the next section). The DMI vector along different planes is anisotropic for different cubic planes, but largest in the $\hat{e}_{[111]}$ direction. With the full information of the exchange interaction from the *ab-initio* calculations we can move forward with the form of the exchange energy where we only consider the DMI acting on nearest neighbors. Within our *ab-initio* method we make use of the frozen magnon calculations which implement spin-spiral formalism to calculate the symmetric exchange parameters. For the DMI interaction we calculate the first order perturbative spin-orbit coupling (SOC) energy added to the spin-spiral state.

3.1.3 Symmetry of the DMI

Including SOC, inversion symmetry must be broken in order for the DMI to arise. In bilayer systems such as Co/Pt and Mn/W this inversion symmetry is broken at the surface [162, 45, 58]. For three dimensional materials the symmetry must be broken in the bulk, and in the case of the B20 compounds the crystals either have a right- or left-handed chirality. The direction of the DMI can be determined for spin-spirals in an isotropic system. However other mechanisms can also break the symmetry such as

dislocations, impurities, etc. The direction of the DMI can be found from the rules first stated by Moriya [109].

If one takes two spins located at \mathbf{R}_1 and \mathbf{R}_2 where the center is at $\mathbf{R}_{inv} = (\mathbf{R}_1 + \mathbf{R}_2)/2$ then:

- The center of inversion is at \mathbf{R}_{inv}
 $\mathbf{D}=0$.
- A mirror plane, A perpendicular to \mathbf{R}_1 and \mathbf{R}_2 and passes through \mathbf{R}_{inv} ,
 $\mathbf{D} \parallel A$ or $\mathbf{D} \perp (\mathbf{R}_1 - \mathbf{R}_2)$.
- A mirror plane B including \mathbf{R}_1 and \mathbf{R}_2 ,
 $\mathbf{D} \perp B$.
- A two-fold rotation axis c perpendicular to $(\mathbf{R}_1 - \mathbf{R}_2)$ and passes through \mathbf{R}_{inv} ,
 $\mathbf{D} \perp c$.
- A n-fold axis d along $(\mathbf{R}_1 - \mathbf{R}_2)$ for $n \geq 2$,
 $\mathbf{D} \parallel (\mathbf{R}_1 - \mathbf{R}_2)$.

In the B20 compounds the crystal symmetry is $P2_13$, where there is a 3-fold rotation axis along the [111] direction. This allows for a DMI in the [111] direction as stated by the last rule.

3.1.4 Anisotropy

Another important interaction due to SOC is the magnetic anisotropy, that prefers moments to point along a particular direction in the crystal, stabilizing the magnetic structure. The leading effect of anisotropy is the magnetocrystalline anisotropy due to the interaction of electron orbitals with the local crystal environment. For our systems the most important form is the uniaxial anisotropy that acts

on single ions independently and forces them to align along a single axis, and has also shown to be crucial in the formation of skyrmions. Uniaxial anisotropy is usually found due to the shape of the crystal such as in hcp Co or L1₀ ordered FePt [106]. The energy for the anisotropy follows,

$$\mathcal{H}_{ani}^{uni} = -k_i \sum_i (\mathbf{S}_i \cdot \mathbf{e})^2 \quad (3.7)$$

Here k_i is the anisotropy per atom. Secondly, and much weaker is the cubic anisotropy, generally seen in cubic systems like bcc Fe and fcc Ni. The Cubic anisotropy has three directions that are easy, hard and very hard. The energy can be described as,

$$\mathcal{H}_{ani}^{cub} = k'_i \sum_i (S_x^4 + S_y^4 + S_z^4) \quad (3.8)$$

where k'_i is the cubic anisotropy energy per atom.

Lastly there is the applied field energy which is also important in stabilizing exotic magnetic structures. This can come from an external magnetic field or an electric current that produces a non-equilibrium field. The energy added to the system by an external field is detailed as,

$$\mathcal{H}_{app} = - \sum_i \mu_s \mathbf{S}_i \cdot \mathbf{H}_{app}. \quad (3.9)$$

3.1.5 Higher Order Exchange

In principle there can be higher order exchange interactions other than the DMI and the two-spin Heisenberg exchange. Upon expanding the Heisenberg Hamiltonian the two most relevant leading terms are the bi-quadratic and the four-spin exchange [61, 3]. These interactions have shown to stabilize skyrmions in two dimensions [59, 31], yet at the knowledge of this dissertation there have not been many studies

of these interactions in bulk materials. The bi-quadratic exchange takes the form,

$$\mathcal{H}_{BI} = - \sum_{ij} B_{ij} (\mathbf{S}_i \cdot \mathbf{S}_j)^2, \quad (3.10)$$

and the four-spin exchange interaction,

$$\mathcal{H}_{4S} = - \sum_{ijkl} K_{ijkl} [(\mathbf{S}_i \cdot \mathbf{S}_j)(\mathbf{S}_k \cdot \mathbf{S}_l) + (\mathbf{S}_j \cdot \mathbf{S}_k)(\mathbf{S}_l \cdot \mathbf{S}_i) - (\mathbf{S}_i \cdot \mathbf{S}_k)(\mathbf{S}_j \cdot \mathbf{S}_l)] \quad (3.11)$$

These terms tend to be quite small compared with the two-spin term and the DMI. In addition for vanishing magnetic moments the higher-order exchange is less dominant, which is a reasonable approximation in the case of FeGe with a moment of $1.2 \mu_B$. Whereas in MnGe the magnetic moment is on the order of $2.3 \mu_B$. However, the four-spin and the bi-quadratic exchange do not directly relate to Berry-Phase effects and are beyond the scope of this dissertation.

3.2 First-Principles approach to Non-Collinear Magnetism

In the previous section (2) we described the energy functional in terms of the charge density \mathbf{n} and the magnetization density \mathbf{m} . However, for non-collinear systems it is more advantageous to equivalently describe the functionals in terms of a 2×2 hermitian density matrix $\boldsymbol{\rho}$. The density matrix and the potential matrix can be expressed in a similar form,

$$\boldsymbol{\rho} = \frac{1}{2} \mathbf{n} \mathbb{1} + \boldsymbol{\sigma} \cdot \mathbf{m} = \begin{pmatrix} n + m_z & mx - im_y \\ mx + im_y & n - m_z \end{pmatrix} \quad (3.12)$$

and

$$\boldsymbol{\rho} = V \mathbb{1} + \mu_B \boldsymbol{\sigma} \cdot \mathbf{B} = \begin{pmatrix} V + \mu_B B_z & \mu_B (B_x - iB_y) \\ \mu_B (B_x + iB_y) & V - \mu_B B_z \end{pmatrix}. \quad (3.13)$$

The components of the density matrix are determined by the KS states, $\rho_{\alpha\beta} = \sum_{i=1}^N \phi_{i,\alpha}^* \phi_{i,\beta}$. When, solving the KS equation (Eq. 2.3) the kinetic energy is diagonal in the two spin directions. The off diagonal components of the potential matrix couple the two components of the Pauli spinor for finite values of B_x and or B_y . In the case when both B_x and B_y are zero, one considers the collinear case and solves the KS equation independently for each spin. In the case of non-collinear calculations the Hamiltonian matrix is always complex, due to the complex Pauli matrix σ_y . This increases the time for calculation where the full Hamiltonian matrix must be solved and the amount of memory needed to store the matrix. Lastly, in systems that lack inversion symmetry, i.e B20 compounds, the Hamiltonian and the overlap matrix are complex hermitian.

In the absence of spin-orbit coupling or dipole interactions, the relation between spin and spatial coordinates are decoupled in the Hamiltonian. The two different spatial systems can be treated independently. Here we can act the spin space group operator on the two component spinor $\{\alpha_S|\alpha_R|\mathbf{t}\}\psi(\mathbf{r}) = \mathcal{U}(\alpha_S)\psi(\alpha_R^{-1}\mathbf{r} - \alpha_R^{-1}\mathbf{t})$ [19, 140, 141]. Where α_S and α_R are the spin and space rotation and \mathbf{t} is the space translation. Lastly, \mathcal{U} is the spin 1/2 rotation matrix. In the presence of SOC, α_S is restricted to equal α_R in order to leave the Hamiltonian invariant for transformations. However, in the absence of SOC, α_S and α_R are allowed to differ. This is an essential feature of the spin space group and necessary for the treatment of spin-spiral calculations.

In the case homogenous and incommensurate spin-spiral calculations the periodicity is lost with respect to lattice translations along the spin-spiral direction \mathbf{q} . However in the absence of SOC, the unit cells of the spin-spiral structure are equivalent. That is the magnitude of the magnetization in each cell and the relative angle

between neighboring cells is the same. This leads to the generalized Bloch Theorem [60, 142], which is valid for spin-spiral solutions without SOC (See Appendix). The generalized Bloch theorem combines a spin rotation and a lattice translation that leaves the Hamiltonian invariant under actions. This allows for the calculations of spin-spiral structures that are computationally less expensive, in a single unit cell.

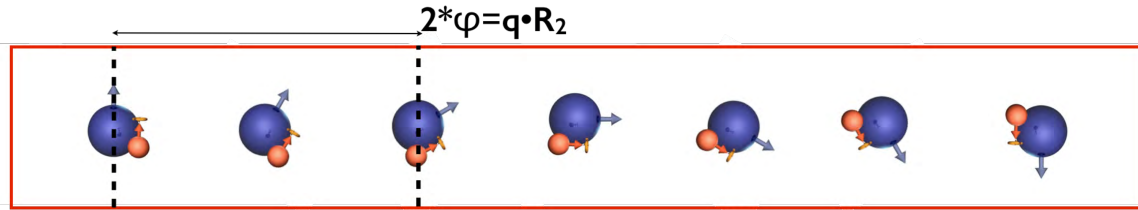


Figure 3.1: Half of a homogeneous spin-spiral state on a mono-atomic 1D magnetic lattice with φ being the rotation angle between neighboring unit cells.

An incommensurate spin-spiral has a lattice length that is different than that of the crystal lattice structure, where a homogenous spin-spiral has a constant angle between neighboring magnetic unit cells. In this case, it is simple to describe a magnetic spin-spiral in each unit cell without SOC as,

$$\mathbf{m}^{n,\mu} = m \begin{pmatrix} \cos(\mathbf{q} \cdot (\mathbf{R}^n + \tau^\mu) + \phi^\mu) \sin \theta^\mu \\ \sin(\mathbf{q} \cdot (\mathbf{R}^n + \tau^\mu) + \phi^\mu) \sin \theta^\mu \\ \cos \theta^\mu \end{pmatrix}. \quad (3.14)$$

In the above equation, \mathbf{R}^n is a lattice vector pointing from the unit cell to cell n , $\tau^\mu u$ is the vector to the basis atom μ , θ^μ is the cone angle between the rotation axis and the magnetic moment at μ , ϕ^μ is the phase shift associated with atom μ , and \mathbf{q} is the spin-spiral vector with the rotation axis set parallel. Due to the generalized

Bloch theorem the spinor wavefunction takes the form,

$$\Psi_{\mathbf{q},\mathbf{k}}(\mathbf{r}) = \begin{pmatrix} e^{i(\mathbf{k}-\mathbf{q}/2)\cdot\mathbf{r}} u_{\mathbf{k}}^{\uparrow}(\mathbf{r}) \\ e^{i(\mathbf{k}+\mathbf{q}/2)\cdot\mathbf{r}} u_{\mathbf{k}}^{\downarrow}(\mathbf{r}), \end{pmatrix} \quad (3.15)$$

here the Bloch phase factor consists of the real-space translation $e^{i\mathbf{k}\cdot\mathbf{r}}$ and the spin rotation around the z -axis $e^{\pm i\mathbf{q}\cdot\mathbf{r}}$ for the two respective spin components. Spin-spirals are sometimes called frozen magnons because they are a snapshot of a magnon at a given time. For this reason spin-spiral calculations are used to simulate finite temperature effects on a magnetic system as well as domain walls. The calculations of spin-spiral ground states in fcc iron [160] and $4f$ and $5f$ metals [121] has lead to many theoretical calculations of spin-spiral systems [112, 161]. Spin-spiral calculations have also lead to more accurate calculations of the exchange parameters and curie temperatures [54].

3.2.1 Spin-Stiffness

Many times it is more advantageous to describe the magnetization as continuous vector $\mathbf{m}(\mathbf{r})$ instead discrete magnetic moments \mathbf{S}_i with $|\mathbf{m}| = 1$. This assumption is valid when the magnetization varies slowly compared to that of the distance between unit cells. If the magnetization rotates along a high-symmetry line for a homogenous spin-spiral, one can adopt a quasi one-dimensional model where the energy is only a function of one variable, the spatial period length $\lambda=2\pi/|\mathbf{q}|$. In this micromagnetic model the discrete spins of a classical Heisenberg-like Hamiltonian are mapped to continuum limit where the magnetization changes very smoothly in space. When the magnetization is constant in magnitude the total energy of the spin-spirals is only

dependent on the parameter \mathbf{q} , and can be written as

$$E(\mathbf{q}) = A\mathbf{q}^2 + D(\mathbf{q} \cdot \hat{e}_{[111]}) + \bar{K}, \quad (3.16)$$

where \bar{K} is the magneto-crystalline anisotropy tensor, which we neglect for the studied cubic B20 compounds, $\hat{e}_{[111]}$ is the unit vector in the high symmetry direction for the DMI D , and A is the spin-stiffness parameter. This is termed the micromagnetic model.

The spin-stiffness constant A is calculated from the local values of J_{ij} and the interatomic distances as [80, 29, 6],

$$A = 4\pi^2 \frac{\Delta}{2b} \sum_{j>0} j^2 J_{0j}. \quad (3.17)$$

In the above, $4\pi^2$ is a normalization factor for one period length of the spin rotation, Δ is the nearest-neighbor distance for magnetic sites parallel to the spiral direction \mathbf{q} , and b is the nearest-neighbor distance for magnetic sites perpendicular to the spiral direction \mathbf{q} . In our calculations we calculate the spin-stiffness directly from the converged self-consistent spin-spiral calculations. Here we fit the energy of the spin-spiral as $E(\mathbf{q}) = A\mathbf{q}^2$ for long wavelength spirals close to the Γ ($\mathbf{q}=(0,0,0)$) point in the spin-spiral Brillouin zone. The calculated spin stiffness changes from 280 for MnGe to 500 meVÅ² for FeGe.

In figure 3.2 the spin-spiral dispersion relation is plotted for $\text{Mn}_{1-x}\text{Fe}_x\text{Ge}$ for $x=1$ (black), $x=0$ (red) and $x=0.8$ (green) on the left and for different high symmetry directions at $x=0.8$ on the right. The graph on the right shows the spin-stiffness changes for flat helical spirals as the electronic structure is changed. The concavity of the FeGe (black curve) is the largest of the B20 compounds of interest. In FeGe the

magnetic transition temperature is also the highest for the B20 compounds studied in this dissertation, at ~ 280 K [36, 170]. The next curve at $x=0.8$ (green) is the critical concentration where experimentally it has been seen that the skyrmion size goes to zero [145, 49]. From the analysis there is no discontinuity between in the spin-stiffness which would cause the skyrmion size to vanish as a function of concentration. Furthermore the spin-spiral dispersion relation is also plotted for MnGe in red, and the concavity is less than that of FeGe. The spin-stiffness for the entire range of x shows a monotonous behavior. Given that the spin-stiffness is directly related to the ordering temperature, these values compare well with experimental results if SOC is neglected [145]. This plot explains the discrepancy in the curve shown in figure 2.6. In these helimagnetic materials the concavity close the Γ point is can be large while the energy difference of the FM and AFM states are small, and vice versa.

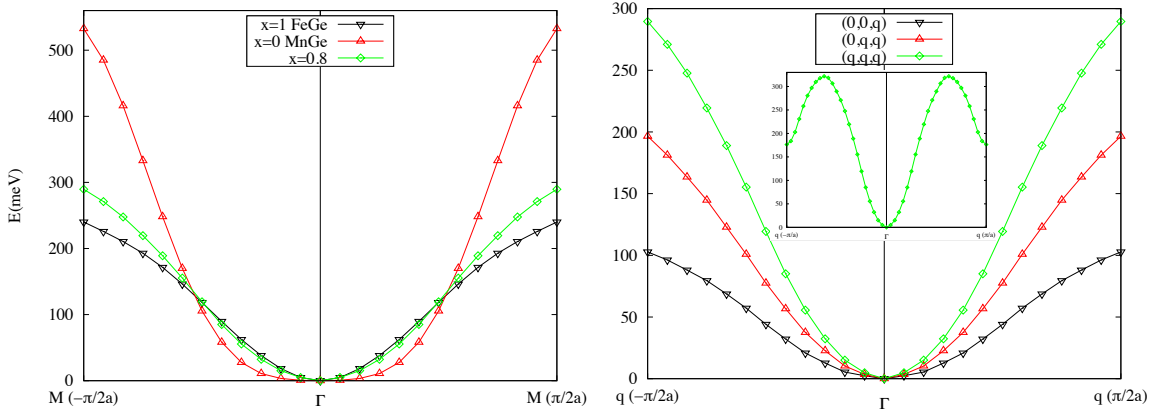


Figure 3.2: *Left* Spin-spiral dispersion relation for $Mn_{1-x}Fe_xGe$ for $x=1$ (black), $x=0$ (red) and $x=0.8$ (green) up to half of the spin-spiral Brillouin zone, M , along the high symmetry direction (q,q,q) . *Right* Spin-spiral dispersion relation for $Mn_{0.2}Fe_{0.8}Ge$ for high symmetry spin spiral directions along $(0,0,q)$ in black, $(0,q,q)$ in red, and (q,q,q) in green. The inset shows the spin spiral direction up to the edge of the Brillouin zone.

In the second figure (3.2) on the right the spin-spiral dispersion relation is shown for the concentration of $x=0.8$ at three different high symmetry directions up to half of the Brillouin zone. The three directions are along the (q,q,q) in green, the $(0,q,q)$ in red, and the $(0,0,q)$ in black. In this curve the spin-stiffness is anisotropic for the three high-symmetry directions but isotropic for equivalent planes, i.e. $J_{xx} = J_{yy} = J_{zz}$. The largest exchange interaction is in the (q,q,q) direction for long-wavelength spin-spirals. In the inset there is the spin-spiral for the (q,q,q) direction up to the edge of the Brillouin zone. The Γ point is a ferromagnetic spin-spiral, however the edge of the Brillouin zone is the antiferromagnetic point. In the inset the AF point is a metastable point in the dispersion curve. This metastable point could be due to higher energy dispersion curves that cross the lowest curve, however this is beyond the scope of this work.

Lastly, in figure 3.3 the spin-stiffness (blue) on a log scale and the magnetic moment (green) as a function of concentration in $\text{Fe}_{1-y}\text{Co}_y\text{Ge}$. At the concentration of $y=1.0$ there is no spin-spiral where CoGe shows paramagnetic behavior. The green curve is the magnetization per transition-metal Ge bond, which is reproduced from figure 2.6. The blue curve shows a monotonous trend of the spin-stiffness for the (q,q,q) direction. This can be directly related to experimental transition temperatures [50] by using the random phase approximation [165, 35].

From the above results (see Figs. 3.2 and 3.3) it is clear that the symmetric Heisenberg exchange interaction does not cause the sign change in skyrmion textures in this systems. The monotonous behavior is consistent with experimental results [145, 49, 50]. It is also clear that the magnetization is quite smooth in the concentration of alloying, not giving any rise to discontinuities. So far we have only considered interactions that are weakly based on SOC. It is well known that the MCA interactions in cubic B20 compounds is quite small

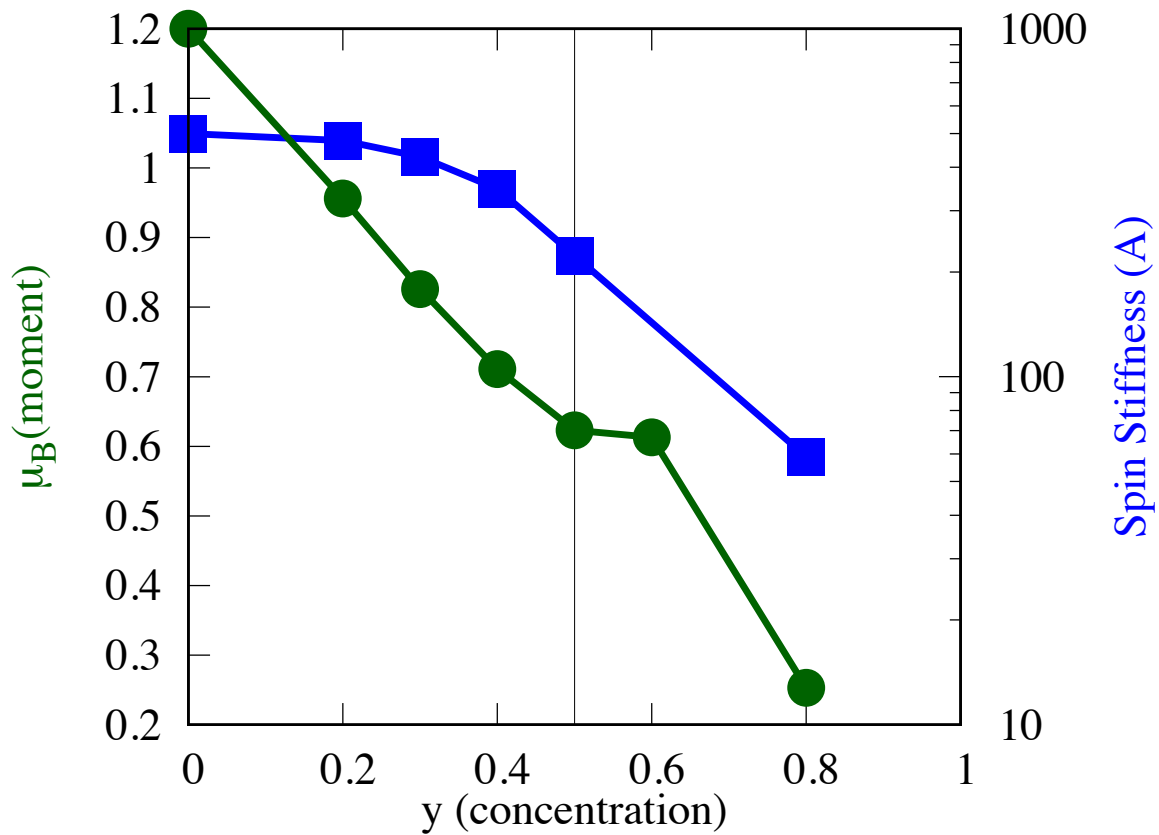


Figure 3.3: Plot of the spin-stiffness (blue) on a log scale and the magnetic moment (green) in $\text{Fe}_{1-y}\text{Co}_y\text{Ge}$. The line at $x=0.5$ is the value with the lowest DMI where one would expect the size of the skyrmions to increase to a ferromagnetic state with no chirality.

3.2.2 Dzyaloshinskii-Moriya Interaction

The linear term in Eq. 3.16 is due to the DMI, with D as the DMI strength. Thus, we compute the D as the slope of the flat spin-spiral energies in the vicinity of $\mathbf{q}=0$ upon including the perturbative effect of SOC [57]. We include the effect of spin-orbit on the energy of spin-spiral states by treating the spin-orbit Hamiltonian

$$H_{SO} = \sum_{\mu=\text{atoms}} \xi_{\mu} \boldsymbol{\sigma} \cdot \mathbf{L}_{\mu} \quad (3.18)$$

within the first order perturbation theory, with μ marking the atoms in the lattice, ξ_{μ} as the SOC strength of atom μ , and L_{μ} as the orbital momentum operator with respect to atom μ . The vector of Pauli spin matrices is denoted by $\boldsymbol{\sigma}$. The first order correction to the energy of a spin-spiral, or, the DMI energy, is given by

$$E_{DM}(\mathbf{q}) = \sum_{\mu} \sum_{n=occ} \sum_{\mathbf{k}} \langle \psi_{\mathbf{kq}n} | H_{SO} | \psi_{\mathbf{kq}n} \rangle = \sum_{\mu} \delta\varepsilon_{\mu}(\mathbf{q}) \quad (3.19)$$

with

$$\delta\varepsilon_{\mu}(\mathbf{q}) = \sum_{n=occ} \sum_{\mathbf{k}} \langle \psi_{\mathbf{kq}n} | \xi_{\mu} \boldsymbol{\sigma} \cdot \mathbf{L}_{\mu} | \psi_{\mathbf{kq}n} \rangle \quad (3.20)$$

as the contribution to $\delta\varepsilon(\mathbf{q})$ from atom μ , and $\psi_{\mathbf{kq}n}$ as the eigenstates of the spin-spiral Hamiltonian without SOC. The last two expressions are used to determine the strength of the total DMI and its atomic decomposition.

The index free description of the DMI is described by an effective constant as the averaged contribution to the energy,

$$D = 2\pi \frac{1}{b} \sum_{j>0} j D_{0j}. \quad (3.21)$$

In this case the DMI is calculated as an effective field. In figure 3.4 the total DMI is plotted for $\text{Mn}_{1-x}\text{Fe}_x\text{Ge}$ (left) and $\text{Fe}_{1-y}\text{Co}_y\text{Ge}$ (right) as the green curve. In addition the DMI for MnSi is plotted as the black dot at the concentration $x=0$. The graph on the left separates the DMI contribution of the transition metal ion, $\text{Mn}_{1-x}\text{Fe}_x$ (blue squares) and the Ge ion (red open squares). The inset on the right is the B20 compound with right-handed chirality with transition ions in light grey and Ge in dark grey.

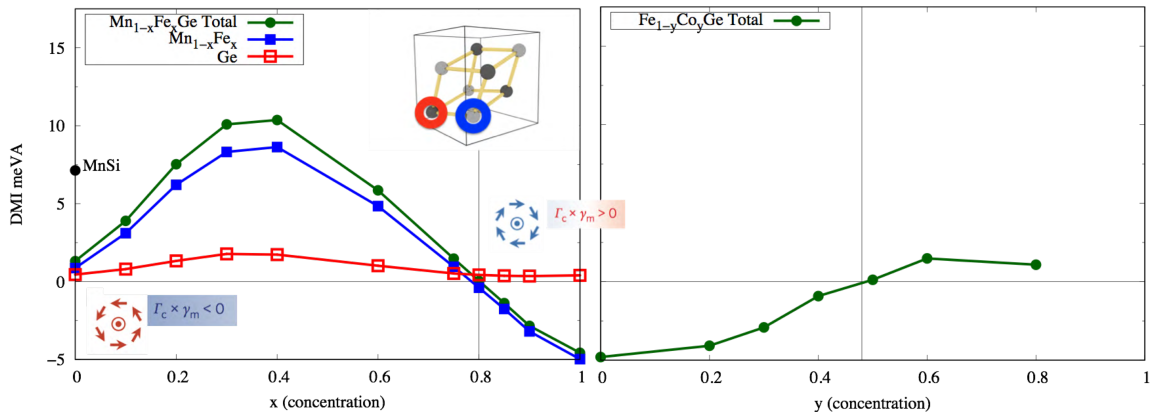


Figure 3.4: *Left:* *Strength of the DMI as a function of concentration x in $\text{Mn}_{1-x}\text{Fe}_x\text{Ge}$ alloys. The total value of the DMI (filled squares) is decomposed into the contributions coming from the transition-metal (red dots) and Ge (blue dots). The inset depicts the crystal structure of the studied B20 compound, with light grey and dark grey spheres representing the transition-metal (TM) and Ge atoms, respectively. *Right:* Strength of the DMI as a function of concentration x in $\text{Fe}_{1-y}\text{Co}_y\text{Ge}$ alloys.

The above figure shows that the DMI in these B20 compounds primarily comes from the transition metal ions. This is due to the bands around the Fermi energy, which are dominated by the magnetic d -states (see fig. 2.7). The SOC from the Ge p -states approximately add a constant background to the DMI and do not cause any discontinuity. At the concentration of $x=0.8$ the value of D rapidly increases with

alloying, and reaches a value of 10 meVÅ at $x = 0.4$. In addition the experimental results show a rapid decrease in the size of skyrmions as the concentration approaches the critical concentration where this $\sim 1/D$ is fulfilled. However, upon approaching the Mn rich alloying, the DMI decreases to a value of 1.2 meV Å. Thus, the theoretical findings of the DMI in MnGe is not in agreement with the experimental findings observation of ultra-small skyrmions in MnGe, on the order of 3 nm [71]. It is assumed that the *ab-initio* description of the electronic structure of MnGe is reliable. Then the discrepancy with experimental findings can be attributed to the breakdown of adiabatic approximation for slowly varying magnetic textures, used to evaluate the D. Another possible explanation for this discrepancy could be that the real spin structure in MnGe is more complex than a simple skyrmion lattice [138, 156]. The very small value of skyrmion size makes current experimental measurements challenging and leaves ambiguity in the structure of the spin lattice in MnGe [145, 70]

3.2.3 Band Structures of Spin-Spiral States

Lastly, as stated above spin-spiral states break the symmetry, where $\mathbf{k} \neq -\mathbf{k}$. In figure 3.5 the electronic band structure of selected spin-spiral states in pure MnGe (top) and FeGe (bottom) is shown as the black lines. In addition, we plot the SO correction at each k-point and energy as the positive (negative) shift with respect to the unperturbed state in blue (red) dots whose size depends on the strength of the interaction. The plots on the right show the density of such energy shifts as a function of energy for the pure MnGe and FeGe on top and bottom, respectively. Integrating the latter SOC-correction energy density up to a certain energy allows us to plot the total DMI energy $E_{DM}(\mathbf{q})$ for a given spin-spiral state as a function of the chosen Fermi energy (see Eq. 3.19).

The above plot shows the effect of the SOC on the spin-spiral bands in MnGe and

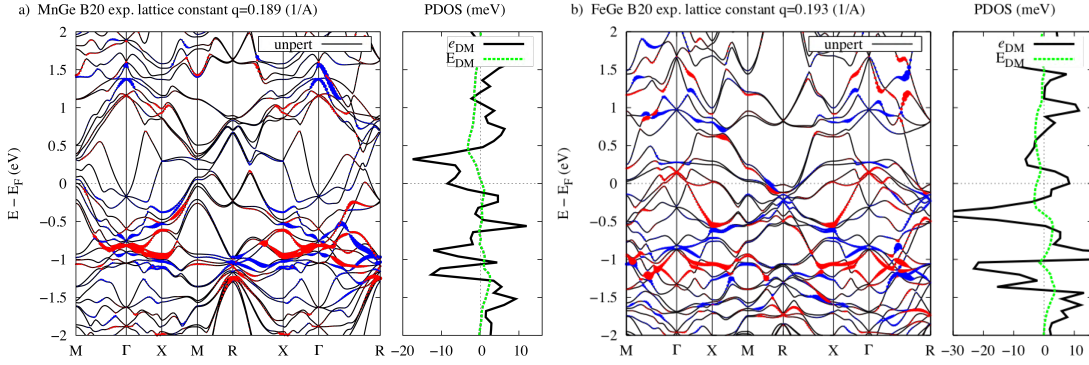


Figure 3.5: Left panels: the unperturbed spin-spiral bands for a) MnGe and b) FeGe with the spin-orbit correction to them displayed with blue (positive) and red (negative) dots. Right panels: the density of SOC-induced energy correction to the eigenvalues at a given energy, e_{DM} , and the value of the total DMI energy as a function of Fermi energy E_F , E_{DM} , obtained as an integral of all e_{DM} below E_F .

FeGe. In the MnGe there are very linear bands at the Fermi energy with positive spin-orbit correction to the states, leading to a small and positive DMI. Whereas, in FeGe the spin-orbit correction is mostly negative close to the Fermi energy. The DMI is a summation of the negative and positive spin-orbit contributions up to the Fermi energy as seen in the energy projected DOS. This causes an oscillatory DOS that changes sign based on the Fermi energy, or occupation level. However the details of the band structure are not completely intuitive, therefore in the next section we develop a simple model to estimate the DMI in B20 compounds derived from our *ab-initio* results.

3.3 TIGHT-BINDING CALCULATIONS OF THE DMI

In this section, I will discuss localized orbitals in the tight-binding (TB) method [13], which was theorized more than 80 years ago for a simple picture of the electronic structure in solids. Then I will briefly discuss the Slater-Koster (SK) two center approximation [150] which improved upon the TB approximation and allowed for a more accurate calculation of the electronic structure by taking into account the orientation of atomic orbitals. Lastly, I will describe our simple TB model on a trimer-type molecule which uses the TB and SK approximations for the electronic structure. Our model compares to the Fert-Levy picture [38] of the DMI. In this section I will primarily focus on the describing the TB approximation for the trimer model (See Fig. 3.8) and later I will discuss a 2-D TB model for the calculation of the AHE and THE in section 7. *

3.4 Tight-Binding Approximation

The TB approximation is considered the simplest approximation to calculate electronic band structures of crystals, and the eigenstates of molecular systems. The method is computationally inexpensive and also allows for a simple intuitive picture of the electronic structure. The TB method can sometimes be referred to as the Linear Combination of Atomic Orbitals (LCAO), where one s the assumption that the crystal basis functions, $\chi_{\mathbf{k}l}(\mathbf{r})$, can be expanded from a basis of atomic like orbitals, $\varphi_l(\mathbf{r} - \mathbf{t}_i)$, that are tightly-bounded to the atoms [77, 100, 99]. Where \mathbf{k} is the crystal momentum, l is the usual angular momentum characters of an atom s, p, d, \dots and \mathbf{t}_i is the position of the i -th atom in the PUC. One must take at least

*Reprinted with permission from "Dzyaloshinskii-Moriya Interaction and Hall Effects in the Skyrmion Phase of $\text{Mn}_{1-x}\text{Fe}_x\text{Ge}$ " J. Gayles, F. Freimuth, T. Schena, G. Lani, P. Mavropoulos, R. A. Duine, S. Blügel, J. Sinova, and Y. Mokrousov. Physical Review Letters,115(3):1-6, 2015. Copyright 2016 by Copyright Clearance Center

the number of valence states on a given atom for the number orbitals to consider in a practical calculation of the LCAO method.

The $\chi_{\mathbf{k}li}(\mathbf{r})$ serve as a basis for expansion of the crystal single-particle eigenstates, $\Psi_{\mathbf{k}}^{(n)}(\mathbf{r})$, where both can be written as;

$$\begin{aligned}\chi_{\mathbf{k}li}(\mathbf{r}) &= \frac{1}{\sqrt{N}} \sum_{\mathbf{R}'} e^{i\mathbf{k}\cdot\mathbf{R}'} \varphi_l(\mathbf{r} - \mathbf{t}_i - \mathbf{R}'), \\ \Psi_{\mathbf{k}}^{(n)}(\mathbf{r}) &= \sum_{l,i} c_{\mathbf{k}li}^{(n)}(\mathbf{r}) \chi_{\mathbf{k}li}(\mathbf{r}).\end{aligned}\tag{3.22}$$

In the appendix A confirm that the crystal basis functions are periodic and Bloch-like in nature. The coefficients $c_{\mathbf{k}li}^{(n)}$, for each band n , are to be determined, for a single particle equation [77],

$$\mathcal{H}\Psi_{\mathbf{k}}^{(n)}(\mathbf{r}) = \epsilon_{\mathbf{k}}^{(n)}\Psi_{\mathbf{k}}^{(n)}(\mathbf{r}) \Rightarrow \sum_{l,i} \left[\langle \chi_{\mathbf{k}mj} | \mathcal{H} | \chi_{\mathbf{k}li} \rangle - \epsilon_{\mathbf{k}}^{(n)} \langle \chi_{\mathbf{k}mj} | \chi_{\mathbf{k}li} \rangle \right] c_{\mathbf{k}li}^{(n)} = 0 \tag{3.23}$$

Where we only consider matrix elements of states with the same \mathbf{k} index, $\langle \Psi_{\mathbf{k}}^{(n)} | \Psi_{\mathbf{k}'}^{(n')} \rangle \sim \delta(\mathbf{k} - \mathbf{k}')$ with \mathbf{k} and \mathbf{k}' restricted the IBZ. The secular Eq. 3.23 at each \mathbf{k} -point has a finite number of solutions (bands, n), which is equal to the number for each different atom type. One can solve Eq. 3.23 by evaluating the integrals $\langle \chi_{\mathbf{k}mj} | \chi_{\mathbf{k}li} \rangle = \sum_{\mathbf{R}} e^{i\mathbf{k}\cdot\mathbf{R}} \langle \varphi_m(\mathbf{r} - \mathbf{t}_j) | \varphi_l(\mathbf{r} - \mathbf{t}_i - \mathbf{R}) \rangle$, which are called the *overlap matrix elements* between atomic states. In a similar way we can solve for the *Hamiltonian matrix elements*.

In the TB method it is common to take an orthogonal basis as an approximation for the overlap matrix elements, $\langle \varphi_m(\mathbf{r} - \mathbf{t}_j) | \varphi_l(\mathbf{r} - \mathbf{t}_i - \mathbf{R}) \rangle = \delta_{lm}\delta_{ij}\delta(\mathbf{R})$, where elements are only non-zero for the same orbitals on the same atom. In a similar fashion we can have the so called *on-site energies* for orbitals on the same atoms as,

$\langle \varphi_m(\mathbf{r} - \mathbf{t}_j) | \mathcal{H} | \varphi_l(\mathbf{r} - \mathbf{t}_i - \mathbf{R}) \rangle = \delta_{lm} \delta_{ij} \delta(\mathbf{R}) \epsilon_l$. The Hamiltonian matrix elements of different orbitals on the same site are zero, which can be seen from the symmetry of the atomic orbitals (see Fig. 3.6). On the contrary the interactions between nearest neighbor sites, \mathbf{d}_{nn} is called the *hopping* matrix elements, which can be non-zero for two sites in the same unit cell or neighboring unit cells. The hopping matrix elements are defined as, $\langle \varphi_m(\mathbf{r} - \mathbf{t}_j) | \mathcal{H} | \varphi_l(\mathbf{r} - \mathbf{t}_i - \mathbf{R}) \rangle = \delta((\mathbf{t}_j - \mathbf{t}_i - \mathbf{R}) - \mathbf{d}_{nn}) V_{lm,ij}$. In Fig. 3.6 the non-zero hopping elements are shown for s , p and d orbitals. These bonds are detailed as: 1) A σ if there is a head to head bonding. 2) π if two orbitals have the same orientation through a plane. 3) Lastly a δ bond is only seen for two d orbitals with four lobes. The nomenclature comes from molecular bonding in chemistry.

With these elements, this is the simplest approximation in the TB method, and only the values of the matrix elements need to be calculated. One of the most common methods, and still an active area of research [103], is to consider these elements as parameters to be obtain from usually fitting first principle calculations. However, it is not always common that orbitals are oriented on the on the same axis as in Fig. 3.6. In this case we take into account the Slater-Koster (SK) approximation, which is briefly described in the next section with references.

3.5 Slater-Koster Two-Center Approximation

Slater and Koster proposed a that the Hamiltonian matrix elements can be approximated with a two-center form [150], which can be used as to simplify electron band structure calculations. In the two-center approximation, interactions only only involve two orbitals on neighboring sites, which is the same as cylindrically symmetric diatomic molecule in free space [100]. In Fig. 3.7, the line, \mathbf{R} , between the center of two p -orbitals determines the values of m with respect tot he azimuthal angular momentum. The figure shows the how the interaction between a p_x and p_z orbital

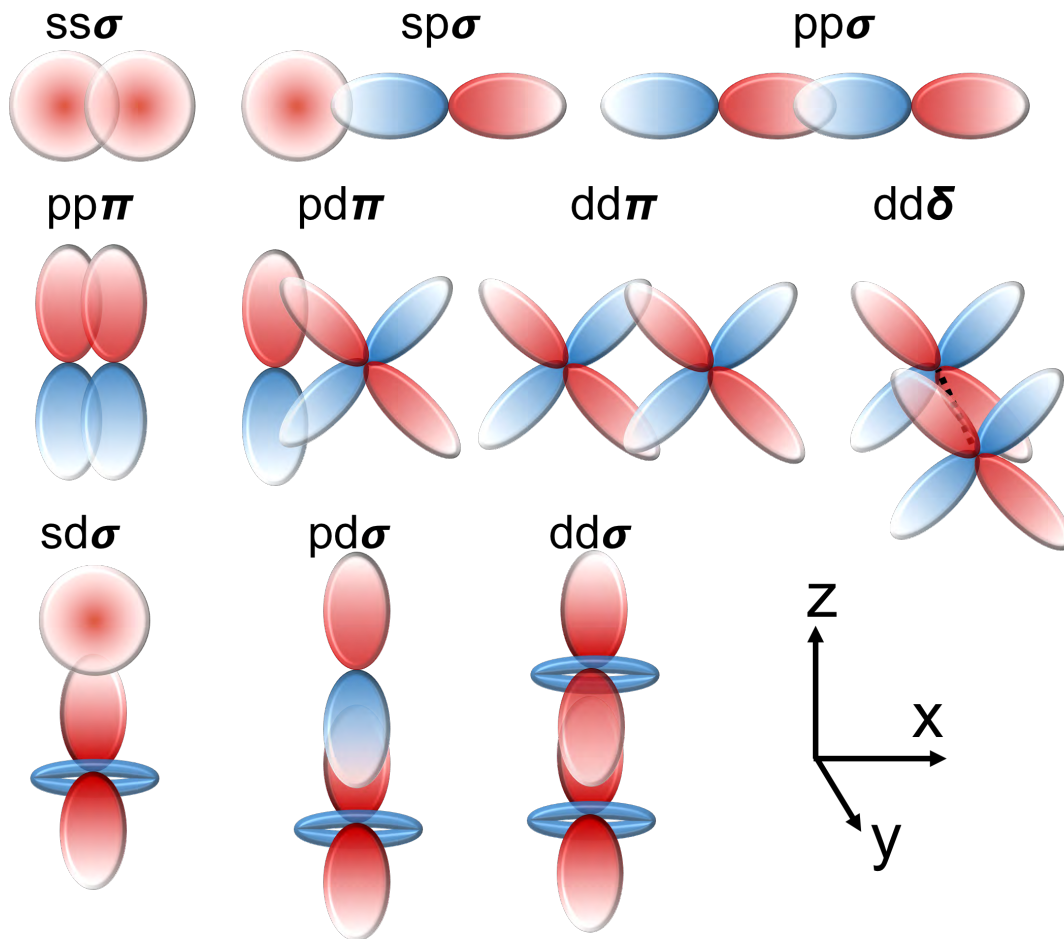


Figure 3.6: Hamiltonian hopping matrix elements between s , p and d states. Where red(blue) lobes are positive(negative).

can be expressed in terms of the irreducible matrix elements. In a similar fashion this can be carried out for all s, p and d orbitals with analytical expressions for the matrix elements [150]. In general one can consider three-center integrals and higher which are smaller, but sometimes not negligible.

The advantage of the SK approach is calculating the electronic bands of complex systems. In order to calculate total energies and forces for different structures the two-center integrals are not sufficient. In addition the integrals must be known as a function of distance. In our tight-binding model we are only interested in the electronic state for the purpose of calculating the DMI, and not structural changes or forces.

3.6 Trimer Model for B20 Compounds

In the previous sections I have neglected the concept of spin in describing the TB approximation. Within our model we will take exchange and SOC into account, which will double the size of our Hamiltonian. The tight-binding model in this work is specifically designed to capture the essential aspects of the electronic structure of the B20 compounds MnGe and FeGe for the formation of the DMI. It is in the vein of the model described by Kashid *et al.* [73]. This model has many similarities to the Fert-Levy picture of DMI [38]. It differs in that the SOC is only present on the non-collinear magnetic sites and the inversion site is spin degenerate with no SOC.

In our model an atomic trimer has been used (of Fig. 3.8), which consists of two identical magnetic atoms A and B with the atomic orbitals d_{xy} and $d_{x^2-y^2}$ each, representing the transition metal (TM) atoms, and a non-magnetic atom C with a p_x orbital, representing the Ge atom. The B20 compound structure comprises of several of those trimers (see Fig. 2.2), and thus the DMI vector of the unit cell is a sum of the DMI vectors of each of these trimers. Since the *ab-initio* calculations

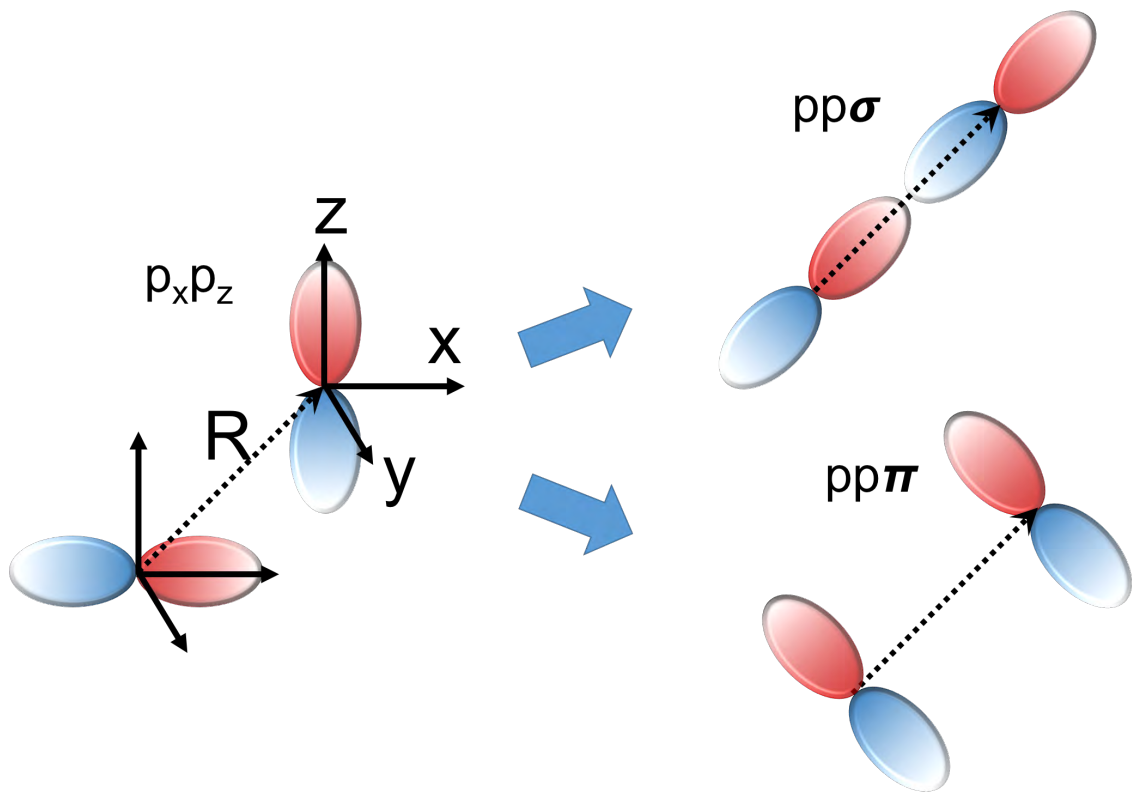


Figure 3.7: Schematic figures for two-center elements between $p-x$ and p_z for sites distance by vector \mathbf{R} .

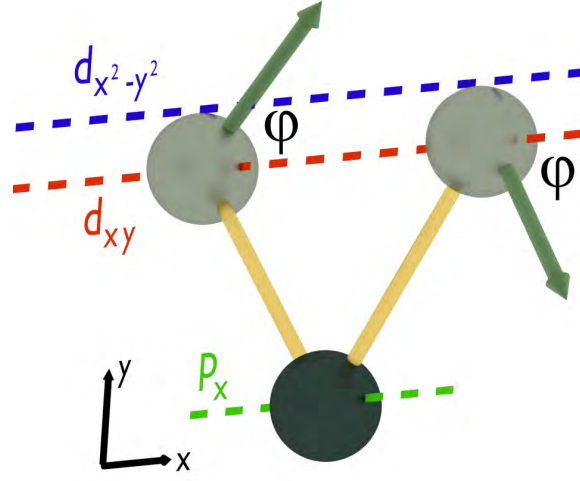


Figure 3.8: Schematic figure of the trimer model with grey sites as non-collinear magnetic sites with angle of 2φ between magnetic directions and $d_{x^2-y^2}$ (d_{xy})-states in blue(red). The dark site is contains the spin-degenerate p -state.

reveal that the sign change in the DMI depending on the concentration of Mn/Fe is solely caused by the spin-orbit coupling (SOC) of the TM atoms (see Fig. 3.4), SOC is only considered in the TM atoms in the model, whereas it is absent in the non-magnetic atom. In representation of the basis $(d_{xy}^A, d_{x^2-y^2}^A, d_{xy}^B, d_{x^2-y^2}^B, p_x^C)$, with the superscripts denoting the site index, we obtain a 10×10 Hamiltonian, which looks as follows with the z -axis as global spin-quantization axis:

$$\mathcal{H} = \left(\begin{array}{c|c} H_{\uparrow\uparrow} & H_{\uparrow\downarrow} \\ \hline H_{\downarrow\uparrow} & H_{\downarrow\downarrow} \end{array} \right), \quad (3.24)$$

$$H_{\uparrow\uparrow} = \begin{pmatrix} E_{A,xy} & i\xi & 0 & 0 & t_1 \\ -i\xi & E_{A,x^2-y^2} & 0 & 0 & t_2 \\ 0 & 0 & E_{B,xy} & i\xi & t_1 \\ 0 & 0 & -i\xi & E_{B,x^2-y^2} & -t_2 \\ t_1 & t_2 & t_1 & -t_2 & E_C \end{pmatrix}, \quad (3.25)$$

$$H_{\uparrow\downarrow} = \begin{pmatrix} -e^{-i\varphi}I_s\tilde{m}/2 & 0 & 0 & 0 & 0 \\ 0 & -e^{-i\varphi}I_s\tilde{m}/2 & 0 & 0 & 0 \\ 0 & 0 & -e^{i\varphi}I_s\tilde{m}/2 & 0 & 0 \\ 0 & 0 & 0 & -e^{i\varphi}I_s\tilde{m}/2 & 0 \\ 0 & 0 & 0 & 0 & 0 \end{pmatrix}, \quad (3.26)$$

$$H_{\downarrow\uparrow} = \begin{pmatrix} -e^{i\varphi}I_s\tilde{m}/2 & 0 & 0 & 0 & 0 \\ 0 & -e^{i\varphi}I_s\tilde{m}/2 & 0 & 0 & 0 \\ 0 & 0 & -e^{-i\varphi}I_s\tilde{m}/2 & 0 & 0 \\ 0 & 0 & 0 & -e^{-i\varphi}I_s\tilde{m}/2 & 0 \\ 0 & 0 & 0 & 0 & 0 \end{pmatrix}, \quad (3.27)$$

$$H_{\downarrow\downarrow} = \begin{pmatrix} E_{A,xy} & -i\xi & 0 & 0 & t_1 \\ i\xi & E_{A,x^2-y^2} & 0 & 0 & t_2 \\ 0 & 0 & E_{B,xy} & -i\xi & t_1 \\ 0 & 0 & i\xi & E_{B,x^2-y^2} & -t_2 \\ t_1 & t_2 & t_1 & -t_2 & E_C \end{pmatrix}, \quad (3.28)$$

where $E_{A,xy} = E_{B,xy}$ and $E_{A,x^2-y^2} = E_{B,x^2-y^2}$ are the onsite energies of the orbitals d_{xy} and $d_{x^2-y^2}$ of the TM site A and B, and E_C is the onsite energy of the non-magnetic site C. The hopping element t_1 describes the hopping between the d_{xy} and p_x orbital, and t_2 is the hopping element between the $d_{x^2-y^2}$ and p_x state, which also introduces the inversion-asymmetry in the system. Note that no direct hopping between the magnetic sites is needed to obtain non-vanishing DMI in this model, and thus only the hopping between the magnetic and non-magnetic sites are included to make the model as simple as possible. The magnetism is incorporated within a Stoner model with an exchange splitting energy $I_s\tilde{m}$, where I_s is the Stoner parameter of the TM sites and \tilde{m} their magnetic moment and φ , which is the mathematically positive/negative angle between the magnetic moment of the site A and B, respectively, and the x -axis. The d_{xy} and $d_{x^2-y^2}$ orbitals are coupled via the SOC

of the TM sites, where the parameter ξ is connected to the strength of the SOC.

The DMI energy E_{DMI} is calculated treating SOC within first order perturbation theory, as it is also done for the *ab-initio* calculations of the B20 compounds. Thus, the DMI energy is calculated from the energy corrections due to SOC $\delta\varepsilon_n$ as follows:

$$E_{\text{DMI}} = \sum_n \delta\varepsilon_n \cdot f(\varepsilon_n) = \sum_n \langle n | \mathcal{H}_{\text{SO}} | n \rangle \cdot f(\varepsilon_n), \quad (3.29)$$

where $f(\varepsilon_n)$ is the Fermi-Dirac occupation function, \mathcal{H}_{SO} is the SOC part of the Hamiltonian in Eq. (3.24) and $|n\rangle$ is the n^{th} eigenfunction of the non-collinear Hamiltonian without SOC.

The following parameters have been estimated from the orbitally-resolved DOS of the *ab-initio* calculation (see Fig. 2.3): $E_{A,xy} = -0.5$ eV, $E_C = -1.5$ eV, $t_1 = 0.5$ eV and $t_2 = 0.3$ eV. A Stoner parameter of $I_s = 1.0$ eV and a SOC parameter $\xi = 0.06$ eV have been used, which are close to the reported values of Fe in [52]. The maximally canted case of $\varphi = 45^\circ$ has been considered.

Furthermore, to properly model the situation of the sign change of the DMI when varying the concentration of Mn and Fe in the B20 compound, the onsite energy difference between the d_{xy} and $d_{x^2-y^2}$ states and the magnetic moment have been changed with the electronic occupation number. We varied the electronic occupation from a bit less than half-filled (4.2 electrons) to more than half-filled (5.2 electrons), and at the same time decreasing the onsite energy difference between the t_{2g} state d_{xy} and the e_g state $d_{x^2-y^2}$ linearly with the electronic occupation, as well as decreasing the magnetic moment quadratically with the electron occupation in accordance to the *ab-initio* results (see Fig. 2.3 and Fig. 3.10). The following equations have been used, with N_e as the electronic occupation number, $\Delta E = E_{A,x^2-y^2} - E_{A,xy}$ as the

onsite energy difference of the TM d states, and \tilde{m} as the magnetic moment:

$$\Delta E = 6.125 - N_e \quad (3.30)$$

$$\tilde{m} = -0.057(N_e - 4.625)^2 - 0.094(N_e - 4.625) + 1.3. \quad (3.31)$$

Note that the first-principles magnetic moment of $\text{Mn}_x\text{Fe}_{1-x}\text{Ge}$ ranges from about $2.2 \mu_B$ to $1.2 \mu_B$ depending on the concentration, but the maximal magnetic moment achievable with our tight-binding model is $2 \mu_B$. Hence, the magnetic moment in the model is varied only between $1.3 \mu_B$ and $1.1 \mu_B$ with respect to the electronic occupation. A non-zero difference in the onsite energies of the d_{xy} and $d_{x^2-y^2}$ state is necessary to obtain DMI, since otherwise the DMI vanishes due to the degeneracy in the eigenvalues.

The magnitude of the DM vector computed within this model, depending on the electronic occupation, is displayed in Fig. 3.9, showing a nice agreement with the *ab-initio* result. For the analysis of the maximum at about $4.7 e$ and the zero-crossing of the DMI energy at $4.95 e$, we plot the orbitally-resolved DOS of the trimer in the ferromagnetic state, broadened by using normalized Gaussian functions. The schematic representation of these computed DOS is presented as an upper panel of Fig. 3.9 and in Fig. 3.10 and 3.11. In Fig. 3.11 we also show the energy of the DMI, E_{DM} shown in green, in each occupation as a function of the Fermi energy. Where E_{DM} is the integral of the projected SOC energy density of states, e_{DM} shown in black.

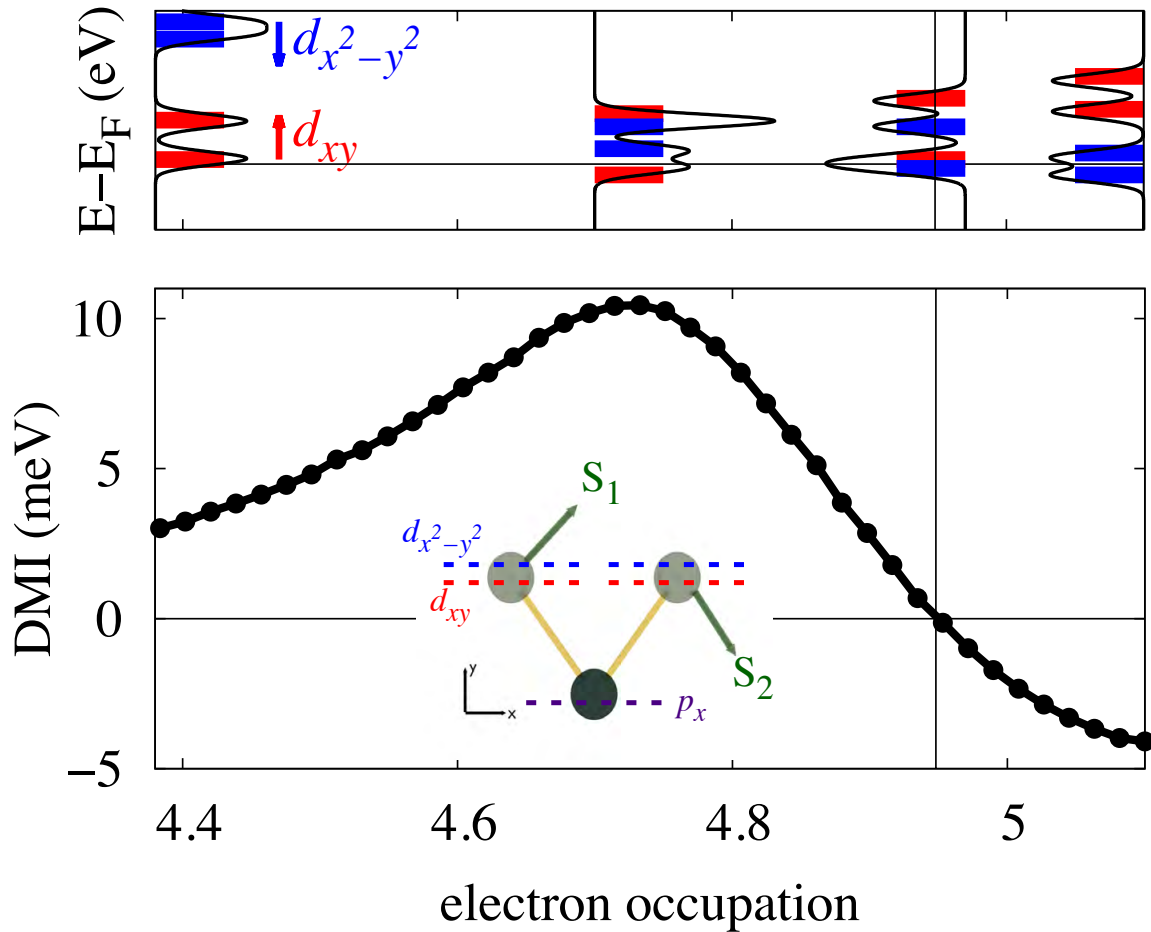


Figure 3.9: *Bottom: Strength of the DMI as a function of electron occupation computed from a simple tight-binding model of a finite trimer (structure shown in inset). Essential is the breaking of local inversion symmetry of the bond between the transition-metal (light gray) and Ge (dark gray). The direction of the left (S_1) and right (S_2) spin lies in the xy plane, and the DMI vector is pointing out of plane. Top: schematic evolution of the d states at the Fermi energy in the tight-binding model with electron occupation.

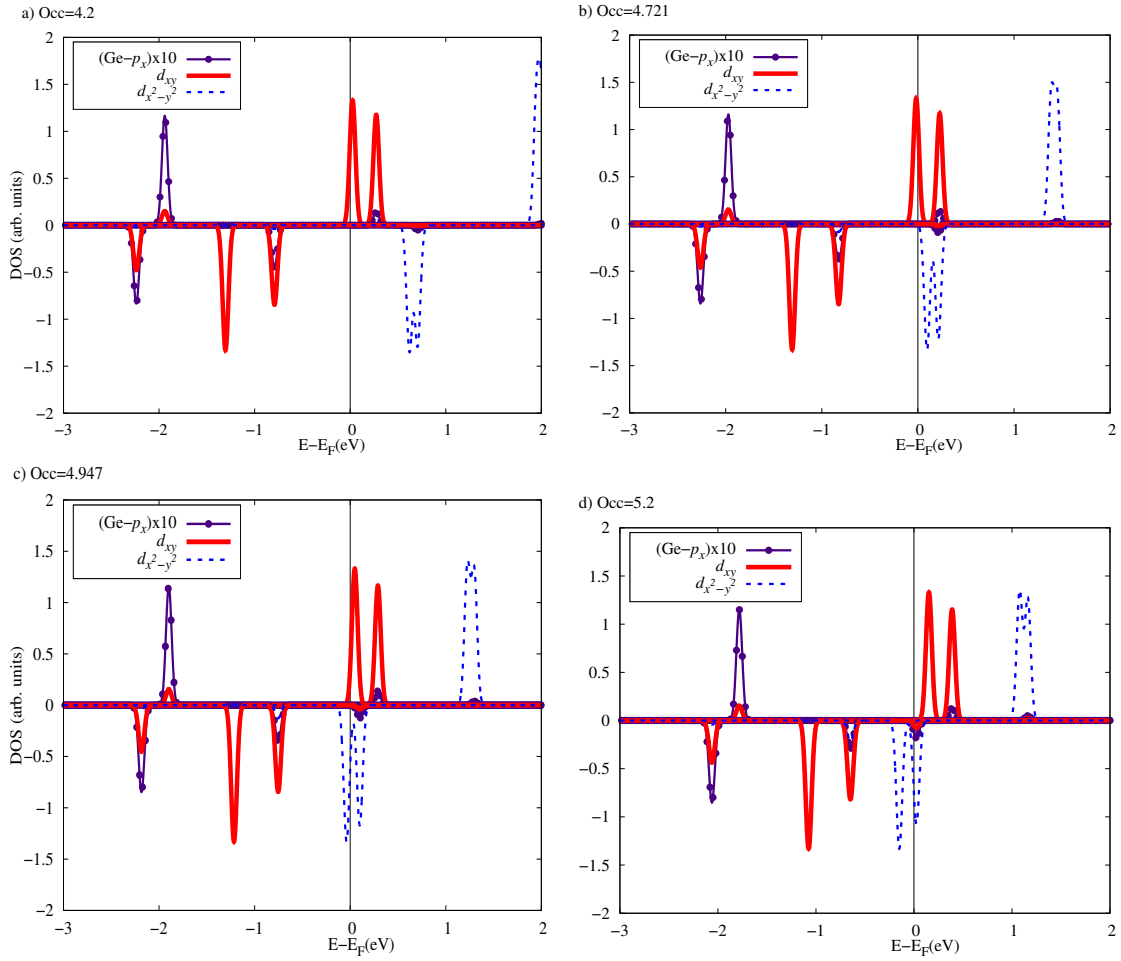


Figure 3.10: Spin and Orbital-resolved ferromagnetic tight-binding DOS at a given occupation of a) 4.2, b) 4.7, c) 4.9, d) 5.2 electrons for the d_{xy} (solid red), $d_{x^2-y^2}$ (dashed blue), and p_x (purple with dots) orbitals.

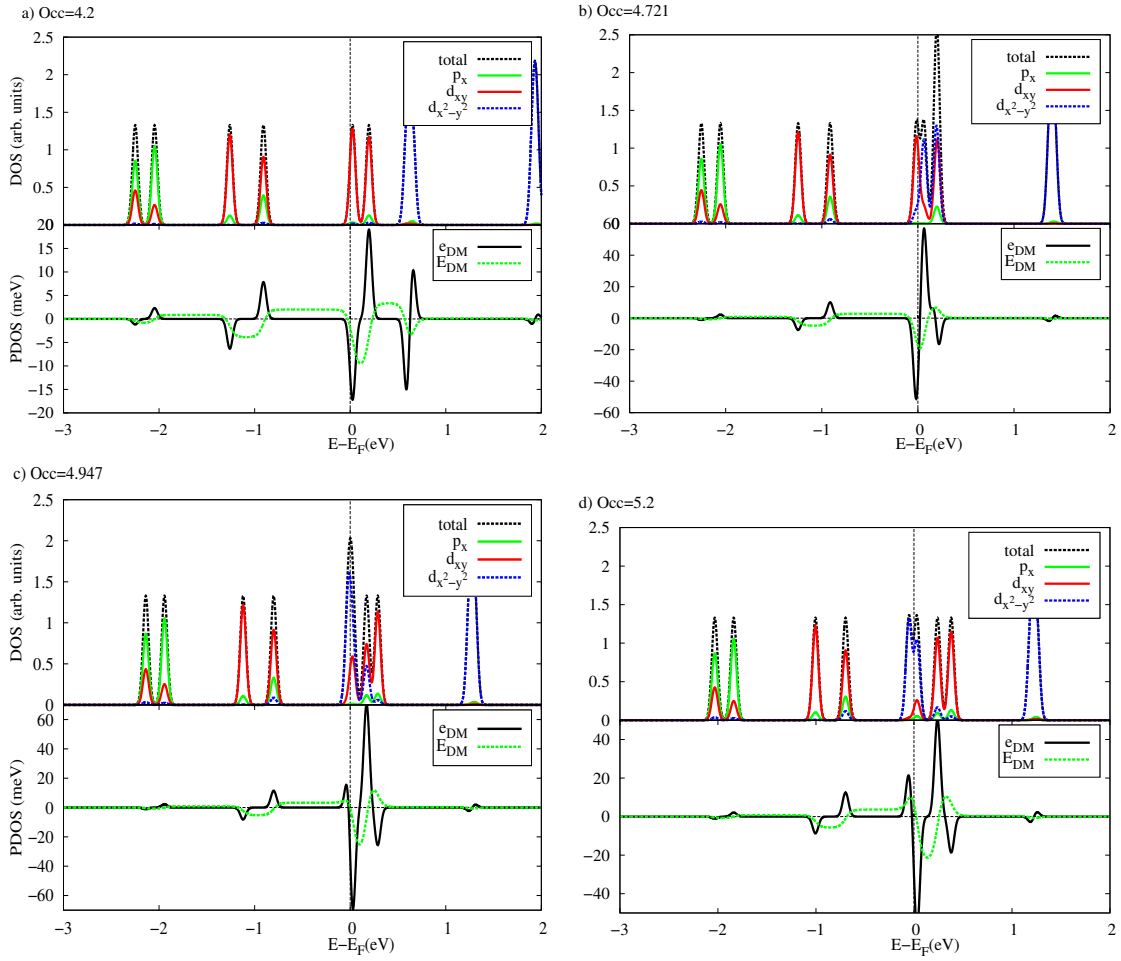


Figure 3.11: In the top panels Orbitaly-resolved ferromagnetic tight-binding DOS at a given occupation of a) 4.2, b) 4.7, c) 4.9, d) 5.2 electrons for the d_{xy} (solid red), $d_{x^2-y^2}$ (dashed blue), and p_x (green) orbitals. The bottom panels show the Fermi energy dependence of the DMI.

3.7 WANNIER FUNCTIONS FOR BERRY CURVATURE

First principle calculations have shown much promise in calculating the ground state properties of many materials over the years. To compare with experimental results one would like to calculate transport properties of the system. Theoretically the three most well-known methods are: the semiclassical Boltzmann formalism, the Kubo formalism, and the Landauer-Büttiker formalism [114]. The idea is to take accurate electronic ground states from the Kohn-Sham method (see section 2.1.2) and calculate observables, such as currents, linear responses to external fields, and correlations between two operators. Each of these methods have their strengths and weaknesses. In many cases these methods are equivalent in specific regimes. In this dissertation we consider only the semiclassical Boltzmann (SB) and the Kubo formalisms which give a more intuitive understanding of Berry-Phase effects [100].

The SB formula is the most intuitive from a pictorial point of view [114]. Although it may not be clear the correct result in certain regimes, and this requires checking with the other two approaches. In regards to the anomalous Hall effect, one can separate the contributions into intrinsic and extrinsic mechanisms, [146]. However, in this dissertation we are only interested in intrinsic effects, i.e. completely due to the band structure. Irregardless, these methods require some basis to in which the Hamiltonian must be determined.

In all three methods one can calculate the properties of the Hamiltonian in a real space or momentum space basis. Most first principle codes form the Hamiltonian in a momentum space basis in the form of Bloch functions, which is the case for the main code of use, FLEUR. Bloch functions are complex and delocalized and calculating velocity operators is generally not trivial, $v \neq \frac{\partial \epsilon}{\partial k}$ being the energy derivative of the band. Whereas, maximally localized Wannier functions (MLWF) are real valued

for collinear systems without SOC and easily relatable to the Bloch functions by a unitary transformation.

Wannier functions were introduced by Wannier as the Fourier transform of Bloch functions [167]. MLWF are advantageous to study local correlation effects, to see a pictorial view of the shape of the functions, hopping integrals, and center and spreads. Within a Wannier basis one can construct a Hamiltonian in real space basis, where the only k dependence is in the exponential factor $e^{i\phi(\mathbf{k})}e^{-i\mathbf{k}\cdot\mathbf{R}}$. In this basis, the velocity operators are simple k partial derivatives. The velocity operators act on the eigenstates of the Hamiltonian, which are the Wannier functions. In this section a general introduction to Wannier functions is shown. The subsequent section (3.11) focuses on calculating Berry-Phase effects from the results of this section.

3.8 Theory

Wannier functions are a set of localized orthonormal functions constructed from a combination of a set of Bloch states[167, 168]. There have been several well-written review of Wannier functions [168, 119, 102]. In addition, there are articles detailing the implementation for practical use[111, 43]. In this section we focus on a formal definition of Wannier functions, which is relevant for understanding the physical properties related to physical properties related the electronic structure of a material.

In the independent particle approximation, Bloch's theorem states that the eigenstates of a crystal are also eigenvalues of the translation operator (see appendix A). In this case each eigenstate extends throughout the crystal with the same magnitude in each unit cell and a different phase. Due to the arbitrary definition of the eigenstate phase, the Bloch functions are subject to gauge transformation which leaves all physical quantities unchanged. Wannier functions are Fourier transformations of

Bloch states for one band, n , centered at site R . They are defined as,

$$\langle \mathbf{r} | \mathbf{R} \rangle = w_n(\mathbf{R}, \mathbf{r}) = \frac{1}{\sqrt{N}} \sum_{\mathbf{k}} e^{-i\mathbf{k} \cdot \mathbf{R}} \psi_{n\mathbf{k}}(\mathbf{r}). \quad (3.32)$$

In the above, N is the number lattice site and the number of \mathbf{k} in the first Brillouin zone. From this it is quite clear how to compute the Bloch functions for known Wannier functions as

$$\psi_{n\mathbf{k}}(\mathbf{r}) = \frac{1}{\sqrt{N}} \sum_{\mathbf{R}} w_n(\mathbf{R}, \mathbf{r}) e^{i\mathbf{k} \cdot \mathbf{R}}. \quad (3.33)$$

One can see from Eq. 3.32 and 3.33 that the Bloch satisfy a periodic gauge for all reciprocal lattice vectors. This assumption is true only if the Bloch functions are periodic in reciprocal space.

The Bloch function for a single band defined as $\psi_{\mathbf{k}}(\mathbf{r}) = e^{i\mathbf{k} \cdot \mathbf{r}} u_{\mathbf{k}}(\mathbf{r})$ and $u_{\mathbf{k}}(\mathbf{r} + \mathbf{R}) = u_{\mathbf{k}}(\mathbf{r})$. From this each Wannier function, n , can be defined as a linear combinations of a set of Bloch functions labeled, i . The the Wannier Functions are then given by $u_{n\mathbf{k}} = \sum_i U_{in}^{\mathbf{k}} u_{i\mathbf{k}}^{(0)}$, where $U_{in}^{\mathbf{k}}$ is \mathbf{k} -dependent unitary transformation[100]. This formulation gives an intuitive interpretation of chemical bonding in crystals.

It is known that the eigenstates are orthonormal, and from this fact is straight forward to prove that the Wannier functions form an orthonormal set [99, 100]

$$\begin{aligned} \int_{all \ space} d\mathbf{r} w_m^*(\mathbf{R}', \mathbf{r}) w_n(\mathbf{R}, \mathbf{r}) &= \int_{all \ space} d\mathbf{r} \frac{1}{N} \sum_{\mathbf{k}} \sum_{\mathbf{k}'} e^{-i(\mathbf{k} \cdot \mathbf{R} - \mathbf{k}' \cdot \mathbf{R}')} \psi_{m\mathbf{k}'}^*(\mathbf{r}) \psi_{n\mathbf{k}}(\mathbf{r}) \\ &= \frac{1}{N} \sum_{\mathbf{k}\mathbf{k}'} e^{-i(\mathbf{k} \cdot \mathbf{R} - \mathbf{k}' \cdot \mathbf{R}')} \delta_{m,n} \delta_{\mathbf{k},\mathbf{k}'} \\ &= \delta_{\mathbf{R},\mathbf{R}'} \delta_{m,n} \end{aligned} \quad (3.34)$$

From here one can compute the matrix elements of the relevant position operators,

$\hat{\mathbf{r}}$ [14, 100]

$$\langle w_n(\mathbf{R}, \mathbf{r}) | \hat{\mathbf{r}} | w_m(0, \mathbf{r}) \rangle = i \frac{\Omega}{(2\pi)^3} \int d\mathbf{k} e^{-i\mathbf{k}\cdot\mathbf{R}} \langle u_{n\mathbf{k}}(\mathbf{r}) | \nabla_{\mathbf{k}} | u_{m\mathbf{k}}(\mathbf{r}) \rangle \quad (3.35)$$

and

$$\langle w_n(\mathbf{R}, \mathbf{r}) | \hat{\mathbf{r}}^2 | w_m(0, \mathbf{r}) \rangle = -\frac{\Omega}{(2\pi)^3} \int d\mathbf{k} e^{-i\mathbf{k}\cdot\mathbf{R}} \langle u_{n\mathbf{k}}(\mathbf{r}) | \nabla_{\mathbf{k}}^2 | u_{m\mathbf{k}}(\mathbf{r}) \rangle \quad (3.36)$$

Bloch functions are defined to be determined up to a constant phase in space. On the contrary, the disadvantage of Wannier functions is that they are not uniquely defined. They can strongly vary in shape and size due to variations in $U_{in}^{\mathbf{k}}$ changing the *relative* amplitude of the Bloch functions at different \mathbf{k} and band index n . It has been shown that the center of mass, which is the sum of all the centers of all Wannier functions, is invariant [14]. All higher order terms are gauge dependent. In addition, each Bloch function is determined within an overall phase factor, where the phase is completely arbitrary and real function of k .

The localization of Wannier function in a specific band is related to the energy gap that separates other bands. In degenerate cases it is impossible to construct localized Wannier functions from the entangled Bloch bands. The above description to the Wannier functions show non-analytic behavior for bands that cannot be disentangled. However, one can describe Wannier-functions for a subspace of bands that spans a desired range of energies.

There are two approaches for the computation of localized Wannier functions from a subspace of entangled bands. The first, termed the *maximally projected* Wannier functions, attempts to construct a reduced set of localized functions from each type of orbital in a given energy range [85, 82]. However this work, uses the second approach

of *maximally localized* Wannier functions [102] which is more appropriate for metallic systems such as the helimagnets of interest. This result is described in detail in the next section with regards to FLAPW formalism [43].

3.9 Computation

The most important quantity for maximally localized Wannier functions is the matrix $M_{mn}^{(\mathbf{k}, \mathbf{b})}$, which contains the all information of the center and the spread of the Wannier functions. The matrix $M_{nn}^{(\mathbf{k}, \mathbf{b})} \equiv \langle u_{\mathbf{k}n} | u_{\mathbf{k}+\mathbf{b}n} \rangle$ can be defined for wannier functions of the form,

$$w'_n(\mathbf{R}, \mathbf{r}) = \frac{1}{\sqrt{N}} \sum_{\mathbf{k}} e^{i\phi(\mathbf{k})} e^{-i\mathbf{k}\cdot\mathbf{R}} \psi_{n\mathbf{k}}(\mathbf{r}), \quad (3.37)$$

where $i\phi(\mathbf{k})$ is an arbitrary function, and restricted to be continuous in \mathbf{k} . These MLWF are non-unique where $i\phi(\mathbf{k})$ is determined up to a constant [43]. One can now write the relevant observables in terms of the matrices.

$$\begin{aligned} \langle \mathbf{r} \rangle_n &= -\frac{1}{N_k} \sum_{\mathbf{k}, \mathbf{b}} w_{\mathbf{b}} \mathbf{b} \text{Im} \ln \tilde{M}_{nn}^{(\mathbf{k}, \mathbf{b})}, \\ \langle r^2 \rangle_n &= \frac{1}{N_k} \sum_{\mathbf{k}, \mathbf{b}} w_{\mathbf{b}} \left[1 - |\tilde{M}_{nn}^{(\mathbf{k}, \mathbf{b})}|^2 + (\text{Im} \ln \tilde{M}_{nn}^{(\mathbf{k}, \mathbf{b})})^2 \right]. \end{aligned} \quad (3.38)$$

The matrix $\tilde{M}_{mn}^{(\mathbf{k}, \mathbf{b})}$ can be evaluated as,

$$\tilde{M}_{mn}^{(\mathbf{k}, \mathbf{b})} = \sum_{m_1} \sum_{m_2} (U_{m_1 m}^{(\mathbf{k})})^* U_{m_2 n}^{(\mathbf{k}+\mathbf{b})} M_{m_1 m_2}^{(\mathbf{k}, \mathbf{b})}, \quad (3.39)$$

which evolves on a uniform \mathbf{k} -grid during the minimization process due to the iterative fitting of $U_{mn}^{(\mathbf{k})}$. In the FLAPW method (see section 2.2.2) the potential is separated into two regions, the interstitial region and the muffin-tin sphere posi-

tioned at μ . Therefore the matrices are also partitioned as $M_{mn}^{(\mathbf{k},\mathbf{b})} = M_{mn}^{(\mathbf{k},\mathbf{b})}|_{INT} + \sum_{\mu} M_{mn}^{(\mathbf{k},\mathbf{b})}|_{MT^{\mu}}$. Within the muffin-tin the block functions are expanded into spherical harmonics that are the solutions of the scalar relativistic equation. In the interstitial the solutions of the Bloch functions already take the form of plane waves and this is a simple expansion to the MLWF, where a step function is introduced to separate the the muffin-tin area. This method can be extended to spin-dependent systems and systems with spin-orbit coupling. For a more extensive review of MLWF in the FLAPW method the reader is referred to the work of Freimuth [43].

One of the most concrete ways to maximally localize wannier functions is to minimize the mean square of the spread Ω , which is defined as,

$$\Omega = \sum_n^{N_{bands}} [\langle r^2 \rangle_n - \langle \mathbf{r} \rangle_n^2]. \quad (3.40)$$

The expectation is for the n -th Wannier function in the unit cell. It is useful to separate the spread (Eq. 3.40) in terms of a gauge invariant part, Ω_I that is the physical measure of the localization and a gauge dependent part $\tilde{\Omega}$ [101, 152, 100]. These two terms are positive and sum to the total spread,

$$\begin{aligned} \Omega &= \Omega_I + \tilde{\Omega} \\ &= \sum_n^{N_{bands}} \left[\langle r^2 \rangle_n - \sum_{\mathbf{R}m}^{N_{bands}} |\langle w_m(\mathbf{R}, \mathbf{r}) | \hat{\mathbf{r}} | w_n(0, \mathbf{r}) \rangle|^2 \right] \\ &+ \sum_n^{N_{bands}} \sum_{\mathbf{R}m \neq 0n}^{N_{bands}} |\langle w_m(\mathbf{R}, \mathbf{r}) | \hat{\mathbf{r}} | w_n(0, \mathbf{r}) \rangle|^2. \end{aligned} \quad (3.41)$$

This forces Ω_I to be both invariant and positive. Minimizing the spread leads to a set of MLWF for a given system, which is the $\tilde{\Omega}$ part since Ω_I is invariant. For a given set of Bloch functions one can take all possible unitary transformations as

seen in Eq. 3.39 and minimizing the matrices by varying $\mathbf{U}^{(\mathbf{k})}$ using the steepest descent method [101, 100]. Once the Wannier functions are maximally localized one can proceed with calculation of properties of the system of interest.

One of the significant properties of interest in this dissertation is the Hamiltonian in terms of the Wannier functions, which is represented in a real space basis. If the number of bands are equal to the number of MLWFs then the $\mathbf{U}^{(\mathbf{k})}$ will be unitary. From here we can write the Hamiltonian in the form,

$$\hat{H} = \sum_{\mathbf{R}_1 m} \sum_{\mathbf{R}_2 m'} H_{m,m'}(\mathbf{R}_1 - \mathbf{R}_2) |W_{\mathbf{R}_1 m}\rangle \langle W_{\mathbf{R}_2 m'}| \quad (3.42)$$

where

$$H_{m,m'}(\mathbf{R}_1 - \mathbf{R}_2) = \frac{1}{N} \sum_{\mathbf{k}n} \epsilon_n(\mathbf{k}) e^{i\mathbf{k}\cdot(\mathbf{R}_1 - \mathbf{R}_2)} [U_{nm}^{(\mathbf{k})}]^* U_{nm'}^{(\mathbf{k})}. \quad (3.43)$$

The hopping integrals are determined by $H_{m,m'}(\mathbf{R}_1 - \mathbf{R}_2)$ between to MLWFs and $\epsilon_n(\mathbf{k})$ are the eigenvalues of the diagonal Bloch Hamiltonian. With the Hamiltonian we can compute useful quantities such as the Berry curvature.

3.10 Band Structure Results

Many times after the minimization of MLWF one would like to check the quality of the Wannier functions. In insulating systems one can check the sum centers and the sum of the spreads of the Wannier functions. In metallic systems and systems with entangled bands MLWF have large spreads due to the electronic nature in metallic bands. One can also compare the band structures in k-space of the MLWF with that of the *ab-initio* electronic structure calculations.

In figure 3.12 the electronic band structure with SOC is plotted for FeGe of the ground state *ab-initio* calculation (see 2.4.2) as the black curves along with that

of the MLWF in red crosses. In FeGe the optimization process uses 64 MLWF, 10 d -type Wannier functions for the four transition magnetic elements, and 6 p -type Wannier functions for four the main group elements. For the calculation of the entangled bands a disentanglement procedure is adapted, where two energy windows are set [152]. Specifically in the case of FeGe the disentanglement ("outer") window is set from -7.43 eV (in the gap above s states) to 18.97 eV above the Fermi energy, where Ω_I is minimized. In the outer window the optimal energy bands may not correspond to the original energy bands due to the hybridization of energy states. In order to retain the exact properties of the system within a desired energy range a frozen ("inner") energy window is set from the bottom of the outer energy window up to 4.77 eV where the states are physically exact in this desired subspace. Similar windows are made for the B20 compounds $\text{Mn}_{1-x}\text{Fe}_x\text{Ge}$ and $\text{Fe}_{1-y}\text{Co}_y\text{Ge}$ within ± 0.2 eV.

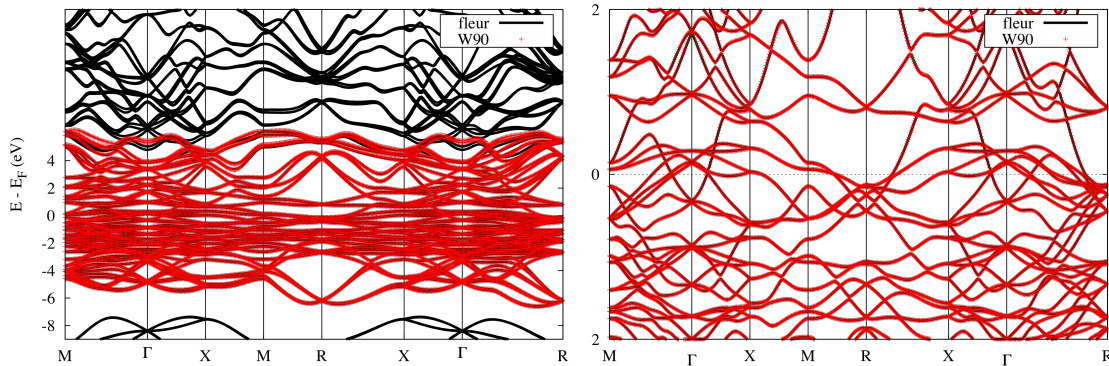


Figure 3.12: *Left* SOC bands of FeGe *ab-initio* in black and the MLWF in red for the outer window. *Right* Zoom of the plot on the left ± 2 eV around the Fermi level.

In figure 3.13 the Wannier functions for MnGe is shown in comparison to the *ab-initio* calculations. Here the four plots show the Wannier functions above the

gap (top left) a 2 eV range around the Fermi level (top right) and the above the Fermi energy (bottom plots). Here only the results for MnGe are shown, where the MLWF have been optimized on a similar setting. The first three graphs (excluding the bottom right) are within the inner energy window where the MLWF match the bands of the FLEUR calculation exceptionally well. The region of most interest is the top right graph for the MLW within ± 1 eV of the Fermi level. This is the most important region for the calculation of Berry-phase effects. Adding a small amount of disorder will keep the Fermi surface within this window. The last graph on the bottom right is where the bands begin to deviate from the *ab-initio* bands. In the regime the bands above 4.5eV are out side of the frozen window, but still in the outer window. This method for calculating the Hamiltonian from the MLWFs is repeated for $\text{Mn}_{1-x}\text{Fe}_x\text{Ge}$ and $\text{Fe}_{1-y}\text{Co}_y\text{Ge}$ where we use the SOC MLWF for the calculation of the AHE and DMI.

Lastly, we calculate the MLWF for spin polarized bands without SOC and the spin dependent Hamiltonians. Similar to the case with SOC the same inner and outer window is used in for the spin-polarized case without SOC. This leads to two non-interacting Hamiltonians for each spin. As in the previous case, we use 64 MLWFs to fit to the *ab-initio* electronic band structure, 32 for each spin state. The MLWFs are converged for each spin separately. In figure 3.14 the MLWF for majority (left red circles) and the minority (right blue circles) are plotted in comparison with the *ab-initio* spin polarized (black bands) electronic band structure of $\text{Mn}_{0.4}\text{Fe}_{0.6}\text{Ge}$. Here the energy is plotted only within ± 2 eV of the Fermi energy. The agreement between the first principles calculations and the MLWFs is suitable for calculation of transport properties. We use the Wannier Hamiltonian and MLWFs in the next section for the calculation of the the topological Hall constant.

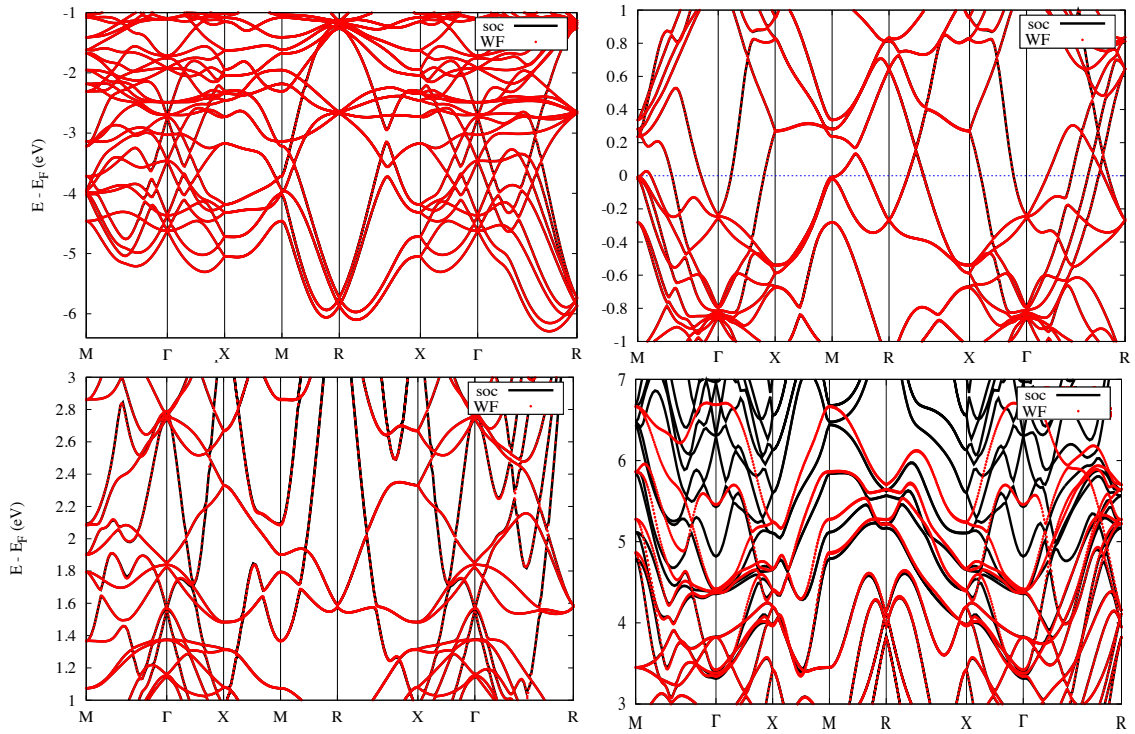


Figure 3.13: *Top left* SOC bands of MnGe *ab-initio* in black and the MLWF in red from the bottom of the frozen energy window to -1 eV below the Fermi level. *Top right* MLWF at ± 1 eV around the Fermi Level. *Bottom left* MLWF from 1 eV above the Fermi level to 3 eV above the Fermi level. *Bottom right* MLWF from 3 eV above the Fermi level to 7 eV above the Fermi level.

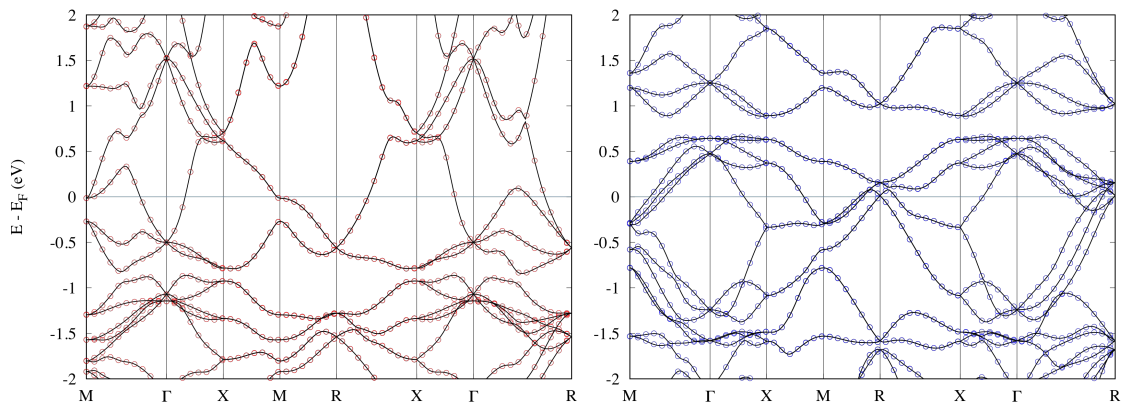


Figure 3.14: *Left* Black bands show majority spin bands for $\text{Mn}_{0.4}\text{Fe}_{0.6}\text{Ge}$ and red circles are the fitted MLWFs. *Right* Black bands show minority spin bands for $\text{Mn}_{0.4}\text{Fe}_{0.6}\text{Ge}$ and blue circles are the fitted MLWFs.

3.11 BERRY PHASE EFFECTS

Although, the concept of geometric phases existed for some time it was not until the intuitive work of Berry [12] that there was an increased interest in geometric phases in condensed matter physics. In this section the Berry phase effects of the B20 compounds will be discussed. The theoretical background of this section follows the lecture notes of Mokrousov et al. [105]. For an introduction to general Berry-Phase theory the reader is referred to the books of Griffiths [48] and Marder [99]. For mathematical perspective of geometric phase the reader can refer to the books of Nakahara [115] and of Bohm [17]. Berry-Phase effects can be found in most branches of physics, but electronic properties in condensed matter systems have come to the forefront and is nicely reviewed by Xiao et al. [173]. Berry-Phases are useful in the description of electric polarization [133], Chern and topological insulators [11]. However, in this case we are more interested in the phase-space Berry effects in metallic systems [174]. *

It is very clear that these materials exhibit strong Berry-Phase effects, mixing real space and reciprocal space. However, these materials have not been closely examined from this point of view in an electronic structure setting to produce experimentally agreeable results. The antisymmetric 6×6 phase-space Berry curvature (BC) is detailed as,

$$\Omega_{n,ij} = \left(\begin{array}{c|c} \Omega_{n,\mathbf{RR}}^{(THE)} & \Omega_{n,\mathbf{Rk}}^{(DMI)} \\ \hline \Omega_{n,\mathbf{kR}}^{(DMI)} & \Omega_{n,\mathbf{kK}}^{(AHE)} \end{array} \right)_{ij}, \quad (3.44)$$

where a non-zero $\Omega_{n,\mathbf{RR}}^{(THE)}$ produces emergent magnetic fields arising from non-

*Reprinted with permission from "Dzyaloshinskii-Moriya Interaction and Hall Effects in the Skyrmion Phase of $\text{Mn}_{1-x}\text{Fe}_x\text{Ge}$ " J. Gayles, F. Freimuth, T. Schena, G. Lani, P. Mavropoulos, R. A. Duine, S. Blügel, J. Sinova, and Y. Mokrousov. Physical Review Letters, 115(3):1-6, 2015. Copyright 2016 by Copyright Clearance Center

trivial textures allowing for a finite THE. $\Omega_{n,\mathbf{k}\mathbf{k}}^{(AHE)}$ is the momentum space Berry curvature which gives rise to the AHE for magnetic systems with spin-orbit coupling. Lastly, $\Omega_{n,\mathbf{R}\mathbf{k}}^{(DMI)}$ contains information of the DMI where a Berry phase is picked up as an electron traverses the phase-space [44]. The DMI is closely related to the spin-orbit torque phenomena which is seen in magnetic systems that also break inversion symmetry [45]. The DMI can be seen as the free energy correction to systems with smoothly varying magnetization in real space. To my knowledge the three phenomena have not been simultaneously calculated from an electronic structure perspective.

3.12 General Berry-Phase Theory

The idea of geometric phases starts with a quantum system described by some Hamiltonian $\mathcal{H}(\lambda)$ that depends on a set of parameters determined by λ . It is assumed that λ is also a function of the eigenstates, where both the Hamiltonian and the eigenenergies, ε_λ , are smooth functions of λ . Here λ is taken to be a slowly varying parameter, taking on an adiabatic approximation. In this approximation a particle in the eigenstate $|\Psi_\lambda\rangle$ will remain in this eigenstate [99]. However, this statement completely disregards the phase of the particle.

If λ is time dependent the Schrödinger equation has the form,

$$-\frac{\hbar}{i} \frac{\partial |\Psi\rangle}{\partial t} = \mathcal{H} |\Psi\rangle \quad (3.45)$$

where the λ and t dependence are dropped for convenience. The trial solution can take the form, $|\Psi\rangle = e^{-(i/\hbar) \int_0^t dt' \varepsilon} e^{i\phi} |\Psi\rangle$. The second part of the phase factor that depends on ϕ is time dependent and is a correction to the eigenstate. This solution

can be inserted into the Eq. 3.45 to get,

$$\frac{\partial \phi}{\partial t} = i\lambda \cdot \langle \Psi | \frac{\partial}{\partial \lambda} | \Psi \rangle. \quad (3.46)$$

The expectation value in Eq. 3.46, $i \langle \Psi | \frac{\partial}{\partial \lambda} | \Psi \rangle$, is called the Berry connection, which connects the wavefunction on two points in λ . In many cases when the berry connection is integrated on a closed loop this leads to a nonzero value, called the Berry-Phase,

$$\Gamma = \oint i\lambda \cdot \langle \Psi | \frac{\partial}{\partial \lambda} | \Psi \rangle d\lambda. \quad (3.47)$$

Of course, λ can take on any values such as momentum, k , or the position, r . However, this can be written at a single point in λ space as $\frac{\partial}{\partial \lambda} |n\Psi\rangle = \sum_{m \neq n} \frac{\langle m\Psi | \frac{\partial \mathcal{H}}{\partial \lambda} |n\Psi\rangle}{\varepsilon_n - \varepsilon_m} |m\Psi\rangle$. From here one can solve for the gauge-invariant expression for the Berry curvature [105],

$$\Omega_{ij}^n = -2\text{Im} \sum_{m \neq n} \frac{\langle n\lambda | \frac{\partial \mathcal{H}}{\partial \lambda_i} |m\lambda\rangle \langle m\lambda | \frac{\partial \mathcal{H}}{\partial \lambda_j} |n\lambda\rangle}{(\varepsilon_n - \varepsilon_m)^2}. \quad (3.48)$$

The curvature above is a second-rank antisymmetric tensor. From Eq. 3.48, it can be intuitively seen that degeneracies in the band (n, m) energies will increase the curvature, i.e. as $(\varepsilon_n - \varepsilon_m)^2$ goes to zero the curvature will go to infinity. This discontinuity will be discussed in the following section.

3.13 Anomalous Hall Effect

Over a hundred ago the anomalous Hall effect (AHE) was discovered a year after Edwin Hall discovered the Hall effect, however it was not until the last two decades that the underlying physics of the AHE was explained, which is quantum mechanical in origin as Berry curvature of Bloch states [114]. The AHE in ferromagnetic

materials with SOC as a transverse response to an electric field that is perpendicular to the magnetic field. In some cases the AHE can arise in non-collinear antiferromagnets due to orbital magnetization [23, 62]. Furthermore, within the last decade first principle calculations have shown tremendous effort in calculating the AHE in ferromagnetic metals and textured magnetic materials. Most of the computational effort has gone to calculating the intrinsic Hall effect due the momentum space Berry curvature. However, recently there has been promising results in the calculation of extrinsic mechanisms using gaussian disorder or the coherent potential approximation [169]. Within this work we are primarily interested in the intrinsic mechanism [166, 176] in B20 compounds. Where the calculation of the extrinsic mechanisms, namely the side-jump, may have significance in future work.

The calculation of the intrinsic AHE is carried out using the Kubo formalism where the eigenstates are taken from ground state first principle calculations. In the Kubo formalism we take a constant- γ approximation, where we take the intrinsic value as $\gamma \rightarrow 0$ [166, 176]. For the calculations of the AHE in $\text{Fe}_{1-y}\text{Co}_y\text{Ge}$ we collaborated with experimentalists at the University of LEEDs in the group of Professor Chris Marrows. In order to compare the AHE with experimental results we match the longitudinal conductivity in the Kubo formalism as a function of γ , where we take the diagonal conductivity at this value (see section 3.20).

In the technical calculation of the Kubo formalism we use maximally localized Wannier functions, instead of the Kohn-Sham eigenstates. Although Kohn-Sham eigenstates ($u_{\mathbf{k}n}$) are Bloch functions, where momentum is a good quantum number, the expectation of the velocity operator is not precisely the derivative of the energy band, $\langle u_{\mathbf{k}n} | \mathbf{v}_{\mathbf{k}n} | u_{\mathbf{k}n} \rangle \neq \frac{1}{\hbar} \frac{\partial \varepsilon_{\mathbf{k}n}}{\partial \mathbf{k}}$. However, with Wannier functions the \mathbf{k} -dependent Hamiltonian is Fourier transformed into a function of \mathbf{R} , where the \mathbf{k} -dependence is considered in an exponential factor. In this case it is simple to take momentum

derivatives of the Hamiltonian, where it is just the derivative of an exponential function, and allows for simple expressions for velocity operators. The Wannier functions are an over-complete basis of the Hamiltonian, however it allows for a speed up in computation where they are fit to the Kohn-Sham eigenstates of the first principle calculation, in a given energy range. The Berry curvature (BC) within the Kubo formalism for the AHE takes the form,

$$\Omega_{ij}^n(\mathbf{k}) = -2\text{Im} \sum_{m \neq n} \frac{\langle u_{n\mathbf{k}} | \frac{\partial \mathcal{H}_{\mathbf{k}}}{\partial \mathbf{k}_i} | u_{m\mathbf{k}} \rangle \langle u_{m\mathbf{k}} | \frac{\partial \mathcal{H}_{\mathbf{k}}}{\partial \mathbf{k}_j} | u_{n\mathbf{k}} \rangle}{(\varepsilon_{n\mathbf{k}} - \varepsilon_{m\mathbf{k}})^2 + \gamma^2}. \quad (3.49)$$

From here it is convenient to introduce the sum of the BC as the sum over occupied bands $\Omega_{ij}(\mathbf{k}) = \sum_n f_n \Omega_{ij}^n(\mathbf{k})$. This is the momentum space Berry curvature that is written $(\Omega_{n,\mathbf{k}\mathbf{k}}^{(AHE)})_{ij} = \Omega_{ij}^n(\mathbf{k})$. The intrinsic anomalous hall conductivity is calculated as the integral of the BC over the entire Brillouin zone:

$$\sigma_{ij}(\gamma) = -\frac{e\hbar}{(2\pi)^3} \int_{BZ} \Omega_{ij}(\mathbf{k}) d\mathbf{k} \quad (3.50)$$

Here the conductivity is a function of γ , the disorder parameter. The calculation of the conductivity is converged as a function of the \mathbf{k} point grid in the full BZ. In principle, the AHE is also anisotropic, however there have not been many studies in regards to first principle studies [106], however this has not yet been studied in the B20 compounds. In this case, we are interested in the AHE as the intrinsic value varies with concentration as also the DMI changes.

3.14 Topological Hall Effect

Contrary to the AHE, the THE does not require spin-orbit coupling and arises from a non-trivial magnetic texture which produces a Berry's phase in real space. This effect was first predicted by Bruno et al. in 2004 and shortly after confirmed

in experiments in the B20 compound MnSi of Neubauer et al. in 2009 [20, 120]. Although, in many of the systems, SOC is necessary in order to stabilize chiral magnetic structures (e.g. DMI), the origin of the THE is due to the emergent field that acts on electron quasiparticles that traverse a magnetic texture[1]. In the limit of strong exchange much larger than the SOC and where the magnetization slowly varies from one site to the next, one can take the approximation that there is little interaction between up and down spins[20]. In this adiabatic approximation one can solve for each spin separately for the THE as the subtraction of the two spin-dependent ordinary Hall effect (OHE) do to the emergent magnetic field, B_e , which has an opposite sign for opposite spins [120]. The relation between the OHE and THE is analogous to that of the AHE and the SHE[45, 148]. Where the THE is seen as the subtraction of spin dependent hall effects in an emergent magnetic field, and the OHE is the addition of the spin dependent hall effects in an external field.

This approximation is made possible due to the fact that the magnetization structure is varying slowly, i.e. that in the local vicinity of a point in real space the direction of the magnetization is considered constant. This gives a set of eigenvalues and wave functions that depend on the local nature of the Hamiltonian. In this case the Hamiltonian is dependent on the position as the electron traverses through a magnetic texture. Generally, this is seen as a mapping of real space to a point on a sphere of S^2 which depends on angles θ and φ . The adiabatic dynamics for each spin is determined by the trajectory on the sphere, where the adiabatic condition requires that time scales of traversing a trajectory is much smaller than spin-flip processes. This means that a quasiparticle stays in a spin-dependent subband throughout the trajectory.

For each spin σ on the sphere there is a Berry connection that contribution from the top and bottom poles of the sphere. The BC corresponds to an emergent

magnetic field that is opposite for each spin which takes the form of

$$\Omega_{ij}^\sigma(\mathbf{R}) = -2\text{Im} \left\langle \frac{\partial \psi_\sigma}{\partial \mathbf{R}_i} \left| \frac{\partial \psi_\sigma}{\partial \mathbf{R}_j} \right. \right\rangle. \quad (3.51)$$

This is the real space BC which is equivalent to $(\Omega_{n,\mathbf{R}\mathbf{R}}^{(THE)})_{ij} = \Omega_{ij}^\sigma(\mathbf{R})$, which is determined for a particular band. This BC can be written in terms of the magnetization texture as $\Omega_{ij}^\sigma(\mathbf{R}) = \hbar \sigma \mathbf{n} \cdot (\frac{\partial \mathbf{n}}{\partial \mathbf{R}_i} \times \frac{\partial \mathbf{n}}{\partial \mathbf{R}_j})/2$. Here \mathbf{n} is the vector of the magnetization, and determines the winding number for each time it winds around the sphere S^2 . The magnitude of the BC tensor at a point in real space is determined by the strength of the variation of the magnetization texture. When the both spin subbands are equally occupied, the sum of the BC equals zero.

In the general case of real ferromagnetic materials the two spin subbands are not equally occupied. A realistic Hamiltonian with a magnetic texture also includes SOC and the crystal potential. In the case of no SOC, the spin and orbital degrees of the wavefunction are decoupled leading to any \mathbf{k} dependent BC to be zero, e.g. $(\Omega_{n,\mathbf{k}\mathbf{k}}^{(AHE)})_{ij} = 0$. Thus the only finite part of the BC tensor is $(\Omega_{n,\mathbf{R}\mathbf{R}}^{(THE)})_{ij}$. The problem can effectively be solved in spin-space because without the effect of SOC, any rotation of the spin-quantization axis does not change the eigenspectrum. Due to the slowly varying in-plane magnetic texture, the electrons scattering on the length scale of the texture can be solved by the Boltzmann equation within the relaxation approximation for an out of plane emergent field B_e as [135],

$$\sigma_{ij}^{THE} \approx \frac{1}{(2\pi)^3} \sum_\sigma \sigma |B_e^\sigma| \sum_n \int_{BZ} \tau_{\sigma n}^2 \left(\frac{(v_{n\mathbf{k}}^i)^2}{m_{n\mathbf{k}}^{jj}} - \frac{v_{n\mathbf{k}}^i v_{n\mathbf{k}}^j}{m_{n\mathbf{k}}^{ij}} \right) \frac{\partial f_0(\varepsilon_{n\mathbf{k}}^\sigma)}{\partial \varepsilon} d\mathbf{k}. \quad (3.52)$$

Here $\tau_{\sigma n}$ are the spin dependent relaxation times, $v_{n\mathbf{k}}$ are the velocities, $m_{n\mathbf{k}}$ is the

effective mass tensor and f_0 is the Fermi occupation. The ordinary Hall effect would read in a similar equation without the index of the spin in the sum.

In order to compare the calculation of the THE in DFT with that of experiments, the topological Hall constant $|R_{yx}^{top}| = \rho_{yx}^{top}/B_e$ is calculated. This allows for the calculation of a scattering independent value that solely depends on the electronic structure of a collinear ordered magnetic structure. Using Wannier functions of the collinear magnetic structure for each spin channel the topological Hall constant is calculated in this semiclassical Boltzmann regime. This calculation in the linear response of the OHE for each spin channel depends on the scattering lifetime τ^2 in the simplest approximation. The longitudinal conductivity is computed and linear in the scattering lifetime. The topological Hall constant is computed as $R_{yx}^{top} = (\sigma_{xy}^{OHE,\uparrow} - \sigma_{xy}^{OHE,\downarrow})/B_e(\sigma_{xx}^\uparrow + \sigma_{xx}^\downarrow)^2$. For both conductivities the $\tau \rightarrow 0$ limit is taken.

3.15 Phase-Space Berry Effects

In the case where there is SOC and a magnetization texture the $(\Omega_{n,\mathbf{R}\mathbf{R}})_{ij}$ and $(\Omega_{n,\mathbf{k}\mathbf{k}})_{ij}$ part of the BC tensor are finite and both contribute to the transverse conductivity. In addition, there is a non-vanishing component of the mixed BC $(\Omega_{n,\mathbf{k}\mathbf{R}})_{ij}$. With both SOC and a magnetization texture there is a modification of the phase density of states $g^n(\mathbf{k}, \mathbf{R}) = \frac{1}{(2\pi)^d} (1 - \sum_i (\Omega_{n,\mathbf{k}\mathbf{R}})_{ii})$ [44]. From here the free energy at a local point \mathbf{R} in space is defined as,

$$F(\mathbf{R}) = -\frac{1}{\beta(2\pi)^d} \sum_n \int d\mathbf{k} \left(1 - \sum_i (\Omega_{\mathbf{k}\mathbf{R}}^n)_{ii} \right) \ln(1 + e^{-\beta(\epsilon_{n\mathbf{k}\mathbf{R}} - \mu)}). \quad (3.53)$$

In the time-independent case the electron wave packet in the semi-classical band energies acquire an additional contribution due to the magnetic texture, $\epsilon_{n\mathbf{k}\mathbf{R}} = \epsilon_{n\mathbf{k}\mathbf{R}} - \text{Im} \sum_i \langle \frac{\partial u_{n\mathbf{k}\mathbf{R}}}{\partial \mathbf{R}} | \epsilon_{n\mathbf{k}\mathbf{R}} - H_{\mathbf{k}\mathbf{R}} | \frac{\partial u_{n\mathbf{k}\mathbf{R}}}{\partial \mathbf{k}} \rangle$. The second part is the correction $\delta\epsilon_{n\mathbf{k}\mathbf{R}}$ to the band energy. The expansion of the free energy in terms of gradients of the

magnetization leads to a first order correction due to the chirality,

$$\delta F(\mathbf{R}) = -\frac{1}{\beta(2\pi)^d} \sum_n \int d\mathbf{k} \left(f_{n\mathbf{k}} \delta \epsilon_{n\mathbf{k}\mathbf{R}} - \frac{\sum_i (\Omega_{\mathbf{k}\mathbf{R}}^n)_{ii}}{\beta} \ln.(1 + e^{-\beta(\epsilon_{n\mathbf{k}\mathbf{R}} - \mu)}) \right). \quad (3.54)$$

In equation 3.54 β is the product of the Boltzmann constant and temperature, and $f_{n\mathbf{k}}$ is the Fermi occupation. This term can be rewritten in terms of the magnetization gradient as [45]:

$$\delta F(\mathbf{R}) = D_{ij}(\mathbf{R}) \hat{\mathbf{e}}_i \cdot (\hat{\mathbf{n}} \times \frac{\partial \hat{\mathbf{n}}}{\partial \mathbf{R}_j}). \quad (3.55)$$

In the above, D_{ij} corresponds to the DMI as discussed in section 3.2.2. Using equation 3.55 and 3.54 the DMI at zero temperature can be written in terms of the phase-space Berry curvature [45], $(\Omega_{n,\mathbf{k}\mathbf{R}}^{(DMI)})_{ij}$, as

$$D_{ij} = \frac{1}{\beta(2\pi)^d} \sum_n \int d\mathbf{k} f_{n\mathbf{k}} [A_{n\mathbf{k}\mathbf{R}}^{ij} - (\epsilon_{n\mathbf{k}\mathbf{R}} - \mu) B_{n\mathbf{k}\mathbf{R}}^{ij}]. \quad (3.56)$$

The above equation introduces $A_{n\mathbf{k}\mathbf{R}}^{ij}$ termed as the twist torque moment to the eigenstate n , and $B_{n\mathbf{k}\mathbf{R}}^{ij}$ which is due to the phase-space BC. The terms are shown in detail in the notes of Mokrousov et al. and the work of Freimuth et al. [105, 45]. This method presents a simplification of computing the DMI from electronic structure methods, however it is not as intuitive as the approach shown in section 3.2.2 where the correction due to SOC is explicitly computed.

3.16 Results in B20 Systems

The computation of the anomalous Hall conductivity at each concentration was carried out *i)* self-consistently and included the effect of spin-orbit interaction for the ferromagnetic state; *ii)* with 64 maximally localized Wannier functions using the WANNIER90 code [111]; *iii)* on a 512^3 k-point grid in the full Brillouin zone

employing the Wannier interpolation technique [166, 177]. Thus, the wave functions entering the calculation of $(\Omega_{n,\mathbf{k}\mathbf{k}}^{(AHE)})_{xy}$ are the eigenfunctions of the collinear ferromagnetic system with SOC. The Wannier functions are the results used in section 3.10. In addition, the Fermi occupation is taken for only the p and d states which form the Wannier band structure. Tests were made where s below the gap (see fig. 3.12) and also with Wannier functions using local orbitals, where results do not change the value of the AHC.

In figure 3.15 the anomalous hall conductivity is plotted as a function of the disorder broadening parameter γ from $1e^{-4}$ to 1 eV for FeGe. As γ approaches zero the value of the conductivity σ_{xy} is constant and reaches the value of -108 S/cm where the magnetization is pointing in the negative z -direction. Upon increasing γ the conductivity varies over 100 S/cm, and at large values of $\gamma > 0.01$ the conductivity consistently increases.

The calculations of the topological Hall constant have been performed analogously to the anomalous Hall conductivity. In this case a set 32 Wannier functions are used for each spin. The value of 512^3 k-points proved to provide converged values of the transport properties. In addition, in this case SOC is neglected. Thus, the wave functions entering the calculation of $(\Omega_{n,\mathbf{R}\mathbf{R}}^{(THE)})_{yx}$ are the eigenfunctions of the collinear ferromagnetic system without SOC. The Wannier functions are the results used in section 3.10. The Fermi occupation is taken for only the p and d states which form the Wannier band structure for each spin which have different occupations (see fig. 3.14).

In figure 3.16 the density of states (top left), longitudinal conductivity (top right), and the ordinary Hall conductivity (bottom left) is plotted for each spin channel as a function of the Fermi occupation. On the bottom right the ordinary Hall conductivity is plotted as a function of the disorder parameter. The two spins are the

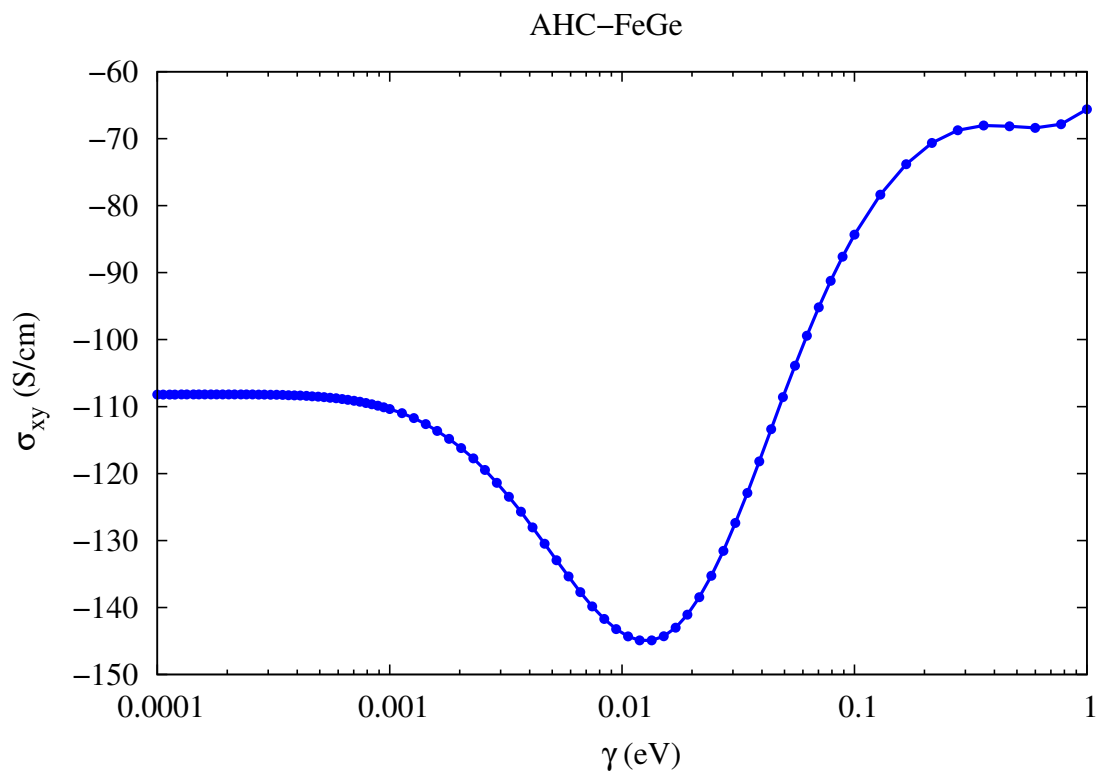


Figure 3.15: The anomalous Hall conductivity σ_{xy} in FeGe as a function of the disorder parameter with the magnetization in the negative z-direction.

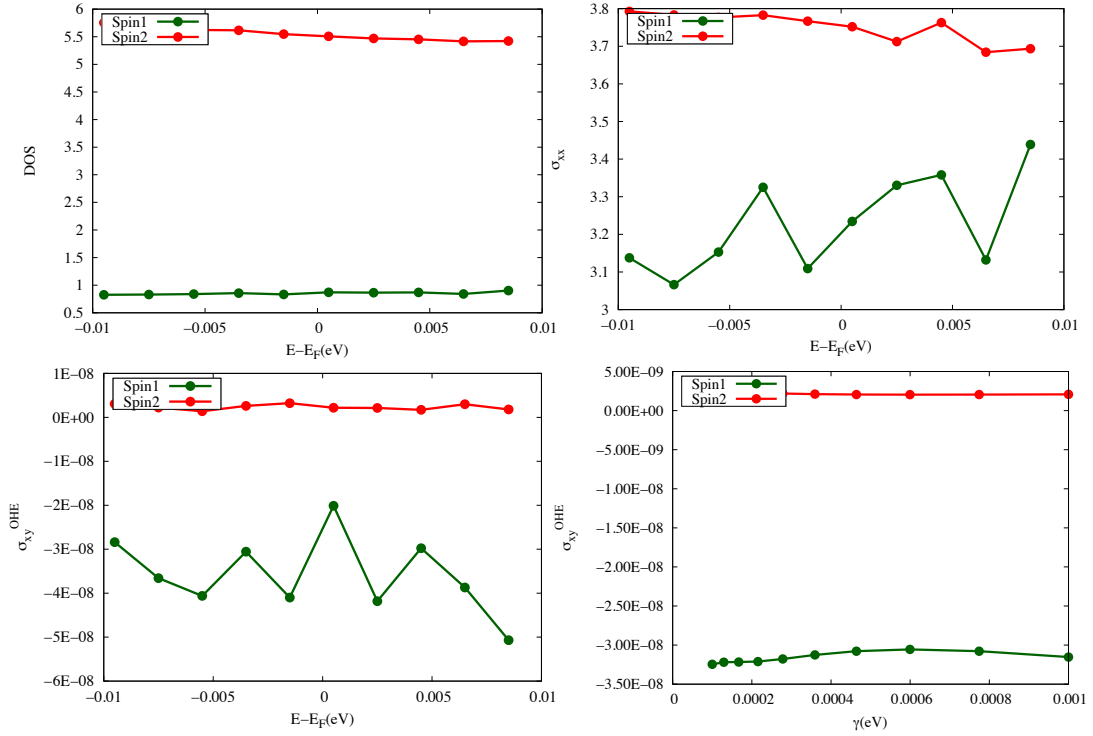


Figure 3.16: *Top Left:* Plot of the number of states as a function the Fermi energy for MnGe for the majority (red) and minority (green) spin. *Top Right:* The longitudinal conductivity as a function of the fermi energy for the majority (red) and minority (green) spin. *Bottom Left:* The ordinary Hall conductivity as a function of the fermi energy for the majority (red) and minority (green) spin. *Bottom Right:* The ordinary Hall conductivity as a function of the disorder parameter for the majority (red) and minority (green) spin.

majority (spin2 red) and the minority (spin1 green) spin channels. Within the small energy window ± 0.1 eV the density of states does not vary drastically. Whereas the longitudinal and the ordinary Hall conductivity vary drastically as a function of the Fermi energy. However, the OHE and the topological Hall constant does not vary strongly as a function of the disorder broadening. In this regime, the calculation of the topological Hall constant is acceptable within in the current approximation, where is should be independent of the disorder.

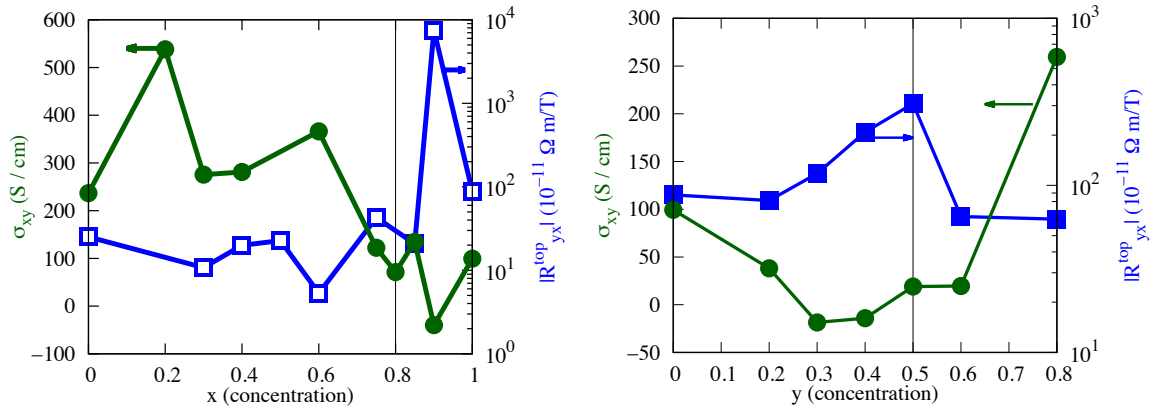


Figure 3.17: *Left:* *The anomalous hall conductivity (blue squares) and topological Hall constant (green circles) is plotted for $Mn_{1-x}Fe_xGe$ and *Right:* $Fe_{1-y}Co_yGe$ for different concentrations of Fe.

Lastly, in figure 3.17 the anomalous hall conductivity (blue squares) and topological Hall constant (green circles) is plotted for $Mn_{1-x}Fe_xGe$ (left) and $Fe_{1-y}Co_yGe$ (right) for different concentrations of Fe. Both plots consist of the intrinsic values of the hall effects due purely to the electronic structure in the limit of zero disorder. The anomalous Hall conductivity varies due to the Fermi occupation of the electronic structure. The intrinsic AHE agrees remarkably well experimental results in the pure cases of MnGe [71] and that of FeGe [131]. In addition, the AHE was recently mea-

sured for different concentrations of Fe in $\text{Mn}_{1-x}\text{Fe}_x\text{Ge}$, which shows strong variation in the conductivity as a function of concentration [72]. Whereas, there calculation of the THE agrees well in the FeGe [64], but in the MnGe [71] there is a breakdown in the adiabatic approximation where the skyrmion size is on the order of 3 nm. In addition, the DMI is lower than the expected experimental results. The THE in the $\text{Fe}_{1-y}\text{Co}_y\text{Ge}$ shows a monotonous behavior as a function of concentration, where at the critical concentration of $y=0.5$ the THE begins to diverge due to the blow up of skyrmions where the DMI goes to zero (see fig. 3.4). Unfortunately, there are not yet any experimental studies of the THE in ternary compounds of the FeCoGe to compare.

3.17 OVERVIEW AND DISCUSSION

In this last section before the conclusion, the work of the dissertation will be compared with recent computational work, that has followed since the main publication of this work in Gayles et. al [47]. Then the connection of this body of work and the many experimental studies will be reviewed. Lastly, the ongoing work in B20 compounds in collaboration with experimentalist will be discussed with future perspectives.

3.18 Theoretical Studies

One of the first studies to calculate the DMI in B20 compounds was done by Freimuth et al in the MnSi [44]. This article uses phase-space Berry curvatures described in section 3.15. These calculations for $D=-4.1 \text{ meV\AA}$ show good agreement with the expected experimental value of -3.43 meV\AA . The results also show that the phase-space Berry-Phases are essential for the stabilization of skyrmionic textures in these compounds and they cause of the redistribution of charge in the skyrmion phase. In this work the calculated the DMI in MnSi is positive and nearly twice the value of what is seen in Freimuth et al. The sign change is due to the using opposite crystal chiralities. In the calculations of Freimuth et al the magnetic moment is constrained to $0.4 \mu_B$, where in this work there are no constraints on the magnetization which relaxes to $0.9 \mu_B$.

One of the more prominent studies that followed this work, is the calculations of Kikuchi et. al [79]. In this paper the authors argue that DMI arises due to a *static* intrinsic spin current Doppler shift, which is due to the SOC and broken inversion symmetry. Therefore the DMI is calculated as the expectation value of a equilibrium spin-current, $D = \langle \hat{j}_s \rangle$ in $\text{Mn}_{1-x}\text{Fe}_x\text{Ge}$ and $\text{Fe}_{1-y}\text{Co}_y\text{Ge}$ (in fig. 3.18 y is replaced by x). In figure 3.18 a schematic of the intrinsic spin-current response to a magnetization

texture in an adiabatic limit. Which is a rewrite of the calculating the DMI as the moments of the torque operator [44]. In addition in figure 3.18, the DMI for varying concentration is plotted comparing the expectation of the intrinsic spin current and the method used in this dissertation. The calculations of the DMI follow the same

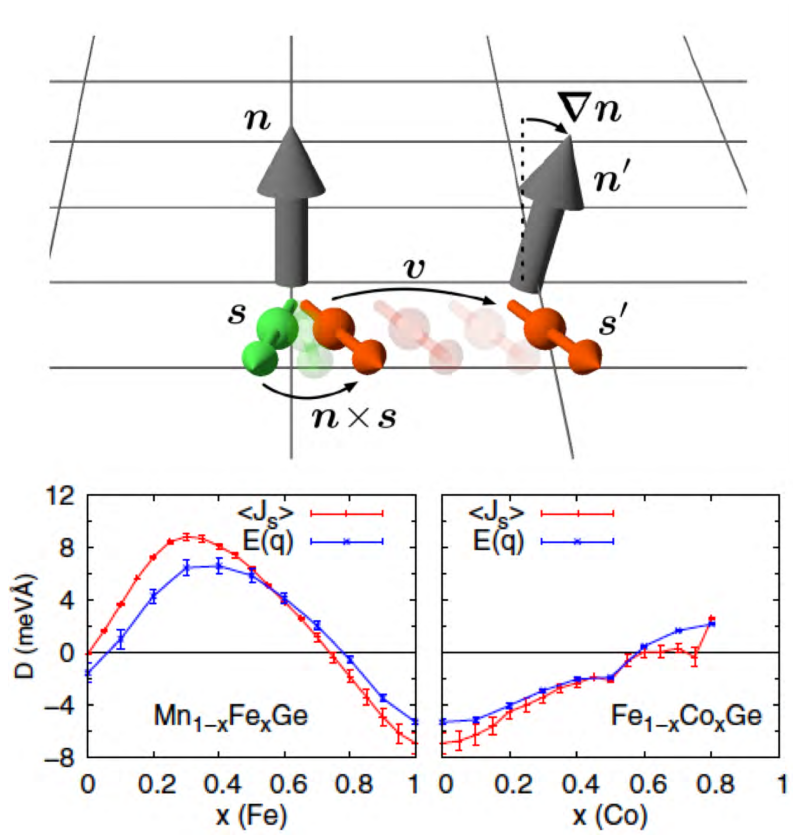


Figure 3.18: *Top:* Schematic of static spin-current Doppler shift. *Bottom:* Comparison of DMI for expectation of the static spin-current (red) and from the values of a helical spin-spiral (blue) [79].

trend and are of the same magnitude as the work in this dissertation. The red curve shows the calculation of the DMI using the static spin-current operator and the blue shows the calculation of helical spin spirals. The blue curve uses the same methods

as this dissertation. However, there is discrepancy in the Mn-rich alloying, where in Kikuchi et. al there is another sign change. This discrepancy is believed to come from the lower density of k -points used by the author, of a $10 \times 10 \times 10$ grid. Where in this work $24 \times 24 \times 24$ grid was used to calculate the DMI. The convergence of the DMI can be quite cumbersome, similar to the MCA.

Another interesting article, which was simultaneously completed as the work of Gayles et. al is the that of Koretsune et. al [84]. In this work they derive the DMI as a \mathbf{q} derivative of the spin correlation function, $D \propto \frac{\partial \chi(\mathbf{q})}{\partial q} |_{q=0}$. These results do not reproduce the change of sign in the DMI at $x \approx 0.8$ as in Gayles et al. and Kikuchi et. al. However, the discrepancy in these calculations may be due to the approximation used by Koretsune et. al. In this case the authors use a tight-binding model fitted from *ab-initio* results. To mimic the alloying affect, the authors vary the electronic occupation by shifting the Fermi energy. In figure 3.19 the anomalous

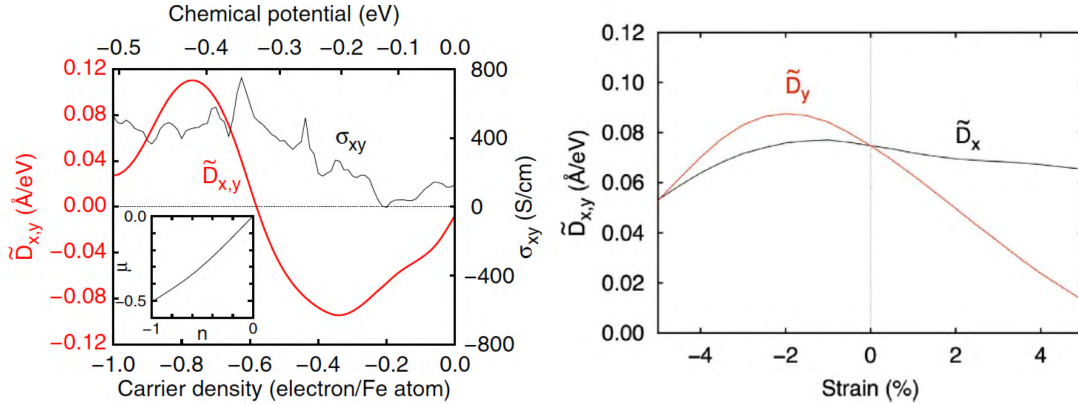


Figure 3.19: *Left:* AHE and DMI as a function of chemical potential from FeGe. *Right:* x and y component of the DMI as a function of uniaxial strain on the y axis at the concentration of $n=-0.45$ [84].

hall effect (black curve) and the DMI (red curve) is plotted as a function of electron

occupation. The results of the AHE are comparable to the results of the dissertation work. Whereas, the DMI values show slightly different trends, but with similar values. Koretsune et. al do find the largest value for the DMI in MnGe when they start with tight-binding parameters fitted from *ab-initio* FeGe and reduce the Fermi occupation. If they start from parameters from self-consistent calculations of MnGe the results differ drastically. In addition, in comparison to my results they do not use the Vegard's lattice constant for varying concentration, and the electronic levels are not reoriented for different occupations. However, it is interesting to see that the DMI is strongly anisotropic under strain (see figure 3.19), which can lead to very interesting effects for magnetic structures.

Moreover, in recent years there has been an increase in interest of understanding and manipulating the DMI. It was shown in 3d monolayers and 3d-5d interfaces that the chemical trend of the DMI follows Hund's first rule [9]. Also, in ferromagnetic/heavy metal bilayers systems it was shown with numerical studies that the interfacial DMI increase the switching current while decreasing the thermal energy barrier [66]. In Rashba SOC systems the DMI increases with SOC strength but decreases with spin-polarization[87]. Lastly, it was shown using DFT+U that the DMI in MnSi is due to a strong hybridization of the Mn-*d* states and the Si-*p* states [143], consistent with the work of this dissertation.

3.19 Experimental Studies

Experimentally, the subject of the DMI has been studied for years. In regards to the B20 compounds the story flows almost like a detective story. It started in 1976 with the first measurements in MnSi showing a helical spiral ground state along the $\langle 111 \rangle$ direction, where the screw axis coincided with the external field direction [65]. It was not until the early 1980's that a clear picture started to arise showing that the

main cause for these spin-spirals are due to the DMI. At this time the first papers derived the thermodynamic expressions for a spin-spiral in the B20 compound as a function of \mathbf{q} , in powers of magnetization, while taking into account the symmetry [7, 130, 116, 117]. However, it was not until the work of Muhlbauer et al. that were the first experiments to show the existence of magnetic skyrmions in B20 compounds [113]

Since this, skyrmions have become an interesting topic in condensed matter physics. Where skyrmions in the B20 compounds have shown a large THE [120, 71, 42, 76]. In addition, it was shown by Shibata et al that the size of the skyrmions can be tuned in $\text{Mn}_{1-x}\text{Fe}_x\text{Ge}$ with concentration of x [145]. This can also be seen in other B20 compounds [72, 107, 50]. The calculations of this dissertation have shown good agreement with the experimental results of Shibata et al and Grigoriev et al, especially in the regime of the critical concentration close to $x=0.8$ [145, 49]. However, at the time publication of Gayles et al there were no experimental studies on the AHE and THE for varying concentrations. There have been experimental studies in the pure Mn/FeGe that measure the AHE and THE [71, 131, 64]. As was discussed in the previous section, the AHE compares well with experiments, where the THE fails to agree with experiments in the case of MnGe [47].

Figure 3.20 shows the experimental findings of the Hall conductivity at fields higher than the field required for ferromagnetic saturation [72]. The results from Kanazawa et al study the magnetic and magneto-transport properties with varying concentration in $\text{Mn}_{1-x}\text{Fe}_x\text{Ge}$. In agreement with past theoretical work [47, 84, 79] the experimentalists show agreement for the magnetization and transport properties. The authors also conclude that by changing the electron occupation the spin orbit effects such as skyrmion size/helicity and transport properties also change continuously.

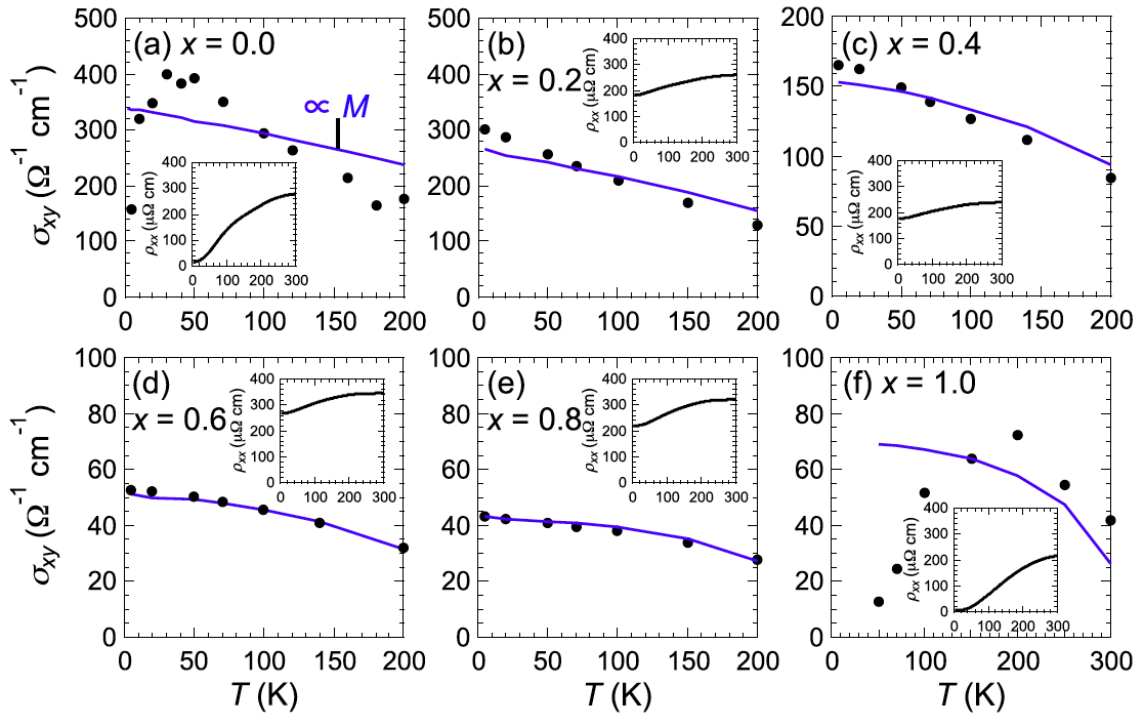


Figure 3.20: The Hall conductivity (black circles) and magnetization as a functions of temperature at fields higher than the critical field to cause a ferromagnetic structure. The insets show the temperature dependence of the zero field resistivity [72].

Since the publication of Gayles et al there have been many experimental works following that expanded the field of Berry-Phase effects. A particular article studies different skyrmions lattices in the pure FeGe compound [144]. Here they see that the shape of the skyrmion and even the lattice shape can vary with magnetic field direction and magnitude. Where the inter-skyrmion distance is invariant in an external magnetic field. In addition, recent experiments have shown that the stabilization of skyrmions in zero magnetic field in FeGe epitaxial thin films on Si(111) surfaces [46]. The results show that as the film thickness is decreased the field for maximum stability decreases. However, there have not been many studies comparing experimental results and computational results side by side in these materials.

3.20 Experimental and Computational Studies of FeCoGe

Since the studies of B20 $\text{Mn}_{1-x}\text{Fe}_x\text{Ge}$ and MnSi, there have been many more studies in other helimagnetic compounds that have the possibility for skyrmion states. One of the B20 that has not seen as much attention as FeGe and MnSi is CoGe. In the bulk at equilibrium pressure CoGe was determined to be a non-magnetic metal [28], where earlier studies believed it to be antiferromagnetic [155]. Previous studies on the ternary compounds have mostly been studied in a monoclinic structure [88]. It was not until recent interest in skyrmions that the helical magnetic structure of $\text{Fe}_{1-y}\text{Co}_y\text{Ge}$ became of interest [50]. Furthermore, it was shown that the cubic anisotropy plays a role by limiting the stability for long wavelength spin-spirals. In addition, it has a contribution to critical external field need to cause ferromagnetic saturation [51].

In figure 3.21 the exchange constant J and the DMI D are calculated from experiment spiral vector using two methods *i*) $k_s = D/J$ [145] and *ii*) $g\mu_B H_{c2} \approx Ak_s^2$ [98, 15]. The first model shows a monotonous behavior of J as the concentration of

Co is increased and a sign change of the DMI at the critical concentration of $x=0.6$. The second model shows the a divergence of both the DMI and J at the critical concentration, which the authors attribute to the change in cubic anisotropy. As the concentration is decreased from the critical concentration the two methods begin to agree.

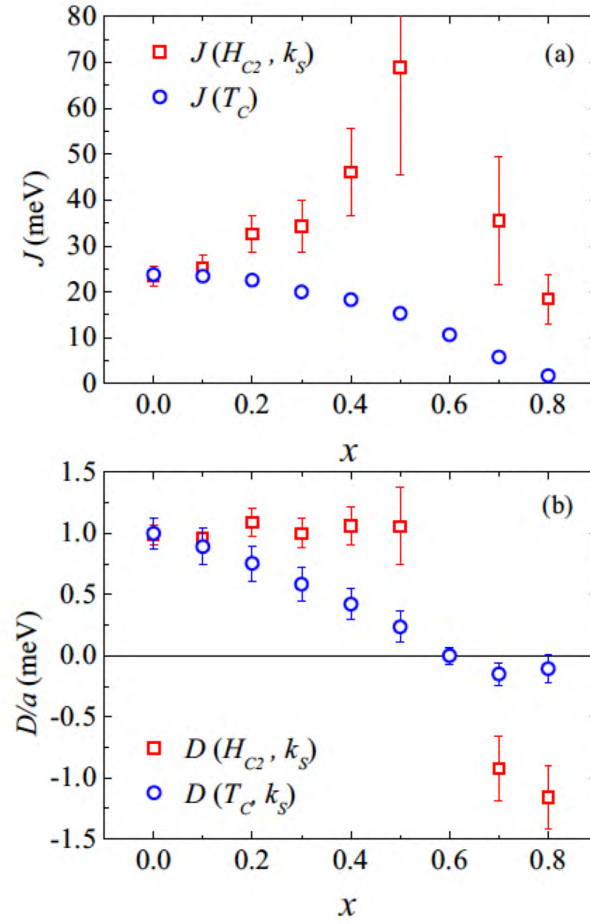


Figure 3.21: Experimental calculation of the exchange constant and the DMI using two methods [51].

In a recent collaboration, we compare first-principle calculations with experiments

in thin films of $\text{Fe}_{1-y}\text{Co}_y\text{Ge}$ [153]. The experimental measurements were carried out by Charles Spencer at ISIS, Oxford, using time-of-flight Polarized neutron reflectometry (PNR) on the Polref instrument. Samples of 20×20 mm samples were mounted in a helium flow cryostat in a $\theta - 2\theta$ configuration. A magnetic field was applied in plane with the film and parallel to the FeGe [110] direction. The reflected intensities of a polarized neutron beam is split into up (\mathcal{I}_+) and down (\mathcal{I}_-) and measured as a function of scattering vector $q_z = (4\pi/\lambda)\sin\theta$. Here θ is the incident angle and λ is the wavelength of the incident neutron. The variation in q_z is provided by the distribution of velocities within the neutron beam and two values of θ are used to provide a range of $0 - 0.15 \text{ \AA}^{-1}$. The total resolution of this PNR method data is 0.03 \AA^{-1} .

In figure 3.22, the results of the PNR measurements are shown in blue for the $\text{Fe}_{1-y}\text{Co}_y\text{Ge}$ for the helical spiral wavelength $\lambda_s \approx J/D$. In addition, the comparison of the bulk first-principles calculations are shown in red along with results from previous experiments using small-angle neutron scattering (SANS) in the bulk shown in red [50]. The results agree as the concentration recedes from the critical concentration. However, the bulk ab-initio results agree better with the thin film PNR measurements, in terms of the critical concentration and the wavelength. The discrepancy in the results that have larger Co concentrations that the critical point may be due to the small magnetic moment in the system. In addition, the PNR results never reach discontinuity in λ_s due to the thin film nature of the samples (70-116 nm). However from these results it is quite clear that the DMI causes a discontinuity in the helical spiral.

The calculations of the bulk first principles were furthered by calculating the AHE for different concentrations of Co. Within the first-principle calculations disorder was introduced by using the constant γ approximation (see section 3.13). These

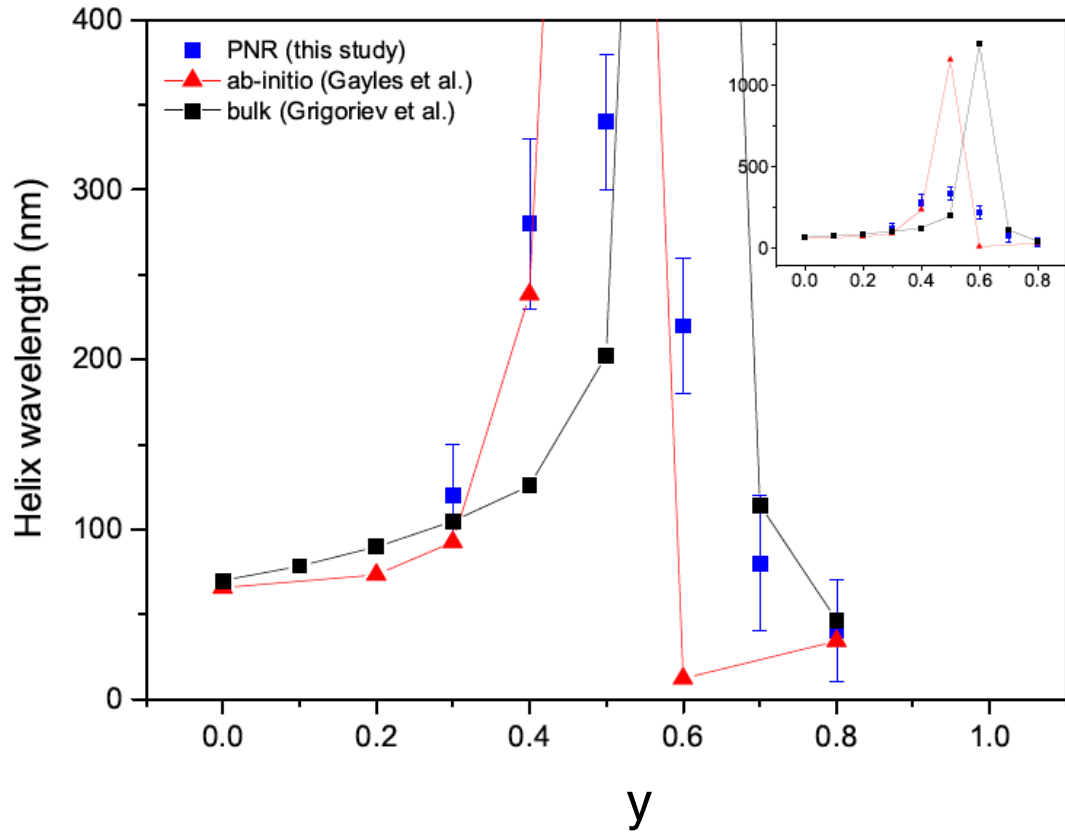


Figure 3.22: Helical wavelength of the $\text{Fe}_{1-y}\text{Co}_y\text{Ge}$ compound as a function of y comparing the thin film PNR (blue), bulk *ab-initio* (red), and bulk SANS (black) [50]. The inset is a zoom out of the original plot, where lines are shown as guides for the eye.

results are compared to that of the experimental results from the samples used in the PNR measurements. In both cases, the longitudinal conductivity and the AHE are compared, which for the first-principle calculations the same disorder parameter is taken into account.

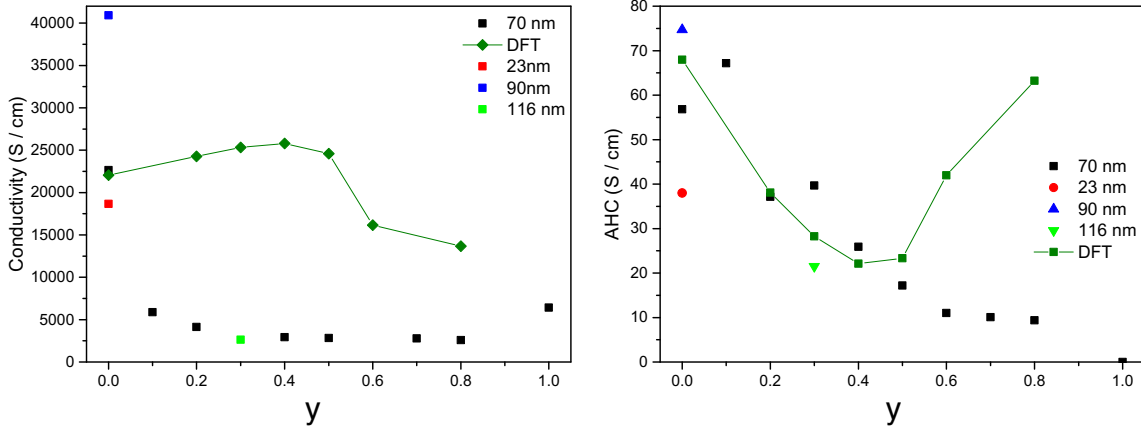


Figure 3.23: *Left:* Comparison of first-principles (green with line) longitudinal conductivity with that of the thin film measurement. *Right:* The anomalous Hall conductivity for $\text{Fe}_{1-y}\text{Co}_y\text{Ge}$ comparing the first-principle and experimental results.

In figure 3.23 the longitudinal conductivity and the AHE are plotted on the left and right respectively, comparing the experimental (points) and first-principle (green line) results. The experimental data was taken for samples of 23, 70, 90 and 116 nm. The first principle calculations are matched to the longitudinal conductivity in the pure FeGe at 70 nm with a disorder parameter of $\gamma = 0.57$ eV. From here, the same γ is used for the calculation of the longitudinal conductivities and the AHE for all concentrations of Co. The discrepancy in the longitudinal data is due to high concentration of impurities for ternary compounds, that are not the pure FeGe. The AHE (see fig 3.23 right) agrees well the experimental data for concentrations below

the critical point. The two possible reasons for this discrepancy, are possibly due to *i*) the vanishing magnetic moment for concentrations $y \leq 0.5$ and *ii*) the absence of scattering mechanisms to the AHE. Where in the small Co concentration limit the AHE is dominated by the intrinsic mechanism.

Lastly there is the calculation of the THE, which is shown for the scattering independent result in section 3.16. These results are still in the process of being measured experimentally. However, it is already clear that the THE will follow the adiabatic approximation in $\text{Fe}_{1-y}\text{Co}_y\text{Ge}$ due to the long wavelength spin-spirals that are expected. At the time of this dissertation there is no knowledge of measurements or calculations of the THE in the $\text{Fe}_{1-y}\text{Co}_y\text{Ge}$ compounds. This would lead to a new perspective in comparison to the results in $\text{Mn}_{1-x}\text{Fe}_x\text{Ge}$ where the adiabatic approximation breaks down for small skyrmion lattices.

4. CONCLUSION

In this dissertation, we used first principle calculations to understand the Berry phase contributions in ternary B20 compounds $\text{Mn}_{1-x}\text{Fe}_x\text{Ge}$ and $\text{Fe}_{1-y}\text{Co}_y\text{Ge}$. These alloys have interested the condensed matter community over the last four decades for their chiral magnetic properties, and recently being some of the first materials to display geometrical magnetic skyrmion phase at finite temperatures and subject to external magnetic fields. The skyrmion phase in these materials is due to spin orbit coupling, causing a the Dzyaloshinskii-Moriya interaction to stabilize a chiral structure with a preferred handedness. Furthermore, there is the topological Hall effect, which is purely due to the geometrical magnetic texture, and the anomalous Hall effect which coexist in the skyrmion phase. Skyrmions show potential for next generation logic devices due to there stability against external magnetic fields and the ease of manipulation with small current densities. Therefore it is of interest to understand the underlying mechanisms, i.e. Berry phase physics, that control the size and the transverse responses due to electrical fields that are used to detect them.

To understand the origin of the sign change in the DMI we have developed a minimal tight-binding model for a finite trimer system (see Fig. 3.8), positioned in the xy-plane. Within our model, the trimer of atoms mimics the bond between the two transition metals and one Ge atom in B20 structure (see Fig. 2.2). This model is derived in a similar way as a previous model for 3d-5d transition metal chains, and it captures the essential physics of the DMI in our ternary alloys. Based on the DFT results, in our model we neglect the SOC on the Ge atom, while the effects of non-collinearity and SOC on transition metals lead to a finite DMI strength, $D = |\mathbf{D}|$, via contribution to the energy of the type $E_{DM} = D \cdot (\mathbf{S}_1 \times \mathbf{S}_2)$, with \mathbf{S}_1 and \mathbf{S}_2 as spin

moments of two transition metal atoms. Within this model a finite DMI is estimated from the difference in energy between two configurations of \mathbf{S}_1 and \mathbf{S}_2 , with both spins lying in the xy -plane and vector \mathbf{D} out-of-plane. This intuitive model showed that the maximum and minimum in the DMI comes from the hybridization of the t_{2g} and e_g states.

In terms of the anomalous Hall effect, we considered the reciprocal space contribution and evaluated the \mathbf{k} -resolved and summed over all occupied states BC $(\Omega_{n,\mathbf{k}\mathbf{k}})_{xy}$ for [001]-direction of the magnetization in our ferromagnetic $\text{Mn}_{1-x}\text{Fe}_x\text{Ge}$ and $\text{Fe}_{1-y}\text{Co}_y\text{Ge}$ crystals for all x and y up to 0.8, with the SOI treated self-consistently. Our calculations show that the anisotropy of $(\Omega_{n,\mathbf{k}\mathbf{k}})_{xy}$ with respect to the direction of the magnetization is rather small. The manifestation of $(\Omega_{n,\mathbf{k}\mathbf{k}})_{xy}$ is the intrinsic contribution to the AHE, with the anomalous Hall conductivity (AHC) σ_{xy} given by the Brillouin zone integral of the non-vanishing \mathbf{k} -space $(\Omega_{n,\mathbf{k}\mathbf{k}})_{xy}$. The dependence of the computed AHC on the concentration of Fe in these alloys, is presented in Fig. 3.17, is ragged, which is typical for transition-metal ferromagnets upon changing the parameters of the electronic structure. Our values can be directly compared to experimental measurements of the AHC in the ferromagnetic phase of MnGe and FeGe, which constitute 150 and 38 S/cm, respectively. Clearly, there is a good qualitative agreement in magnitude, sign and trend between our calculations and experiments, while the remaining differences can be attributed to, e.g., extrinsic contributions to the AHE.

We also calculate the real part of BC tensor $(\Omega_{n,\mathbf{R}\mathbf{R}})_{yx}$ which gives rise to the topological Hall effect. For pure alloys, the sign of the THE which we predicted agrees with the experimental values. In the case of FeGe the value of R_{yx}^{top} constitutes $88 \times 10^{-11} \Omega\text{m}/\text{T}$ and compares remarkably well with the experimental value of $72 \times 10^{-11} \Omega\text{m}/\text{T}$, computed from the experimental values for ρ_{yx}^{top} and B_e . In MnGe

we obtain a value of $25 \times 10^{-11} \Omega\text{m}/\text{T}$ for R_{yx}^{top} , which is two orders of magnitude larger than the experimental value of $0.4 \times 10^{-11} \Omega\text{m}/\text{T}$. The overestimation of the topological Hall constant along with the underestimation of the DMI in Mn-rich alloys, can be attributed to the breakdown in the adiabatic approximation. This essential Berry phase viewpoint, shows the inability to properly capture the effect of a conduction spin to follow the rapidly varying magnetization of the skyrmion lattice. The physics of the electron dynamics and Hall effects in this regime, and its proper description with first principles methods, present important directions to tackle, especially in the light of recent intensive interest in nano-scale non-trivial spin textures arising at surfaces and interfaces.

In conclusion, our calculations have shown the extent of first-principle calculations in the regime of the adiabatic approximation for metallic chiral magnetic materials. The work we published has initiated studies to understand the Berry Phase physics from many perspectives. We see that these BC effects can be manipulated by the electronic occupation and alloying leading for precise atomic control of the spin-orbit effects, which could possibly lead to technology for next generation devices.

REFERENCES

- [1] Ar. Abanov and V. L Pokrovsky. Skyrmion in a real magnetic film. *Physical Review B*, 58(14):4, 1998.
- [2] T. Adams, A. Chacon, M. Wagner, A. Bauer, G. Brandl, B. Pedersen, H. Berger, P. Lemmens, and C. Pfleiderer. Long-wavelength helimagnetic order and skyrmion lattice phase in Cu_2OSeO_3 . *Phys. Rev. Lett.*, 108(23):1–5, 2012.
- [3] J. Adler and J. Oitmaa. The Heisenberg ferromagnet with higher-order exchange. *Journal of Physics C: Solid State Physics*, 12(3):575, 1979.
- [4] P. W. Anderson. Antiferromagnetism. Theory of superexchange interaction. *Phys. Rev.*, 79(2):350–356, jul 1950.
- [5] P. W. Anderson. Theory of magnetic exchange interactions - exchange in insulators and semiconductors. *Solid State Physics-Advances In Research And Applications*, 14:99–214, 1963.
- [6] U. Atxitia, D. Hinzke, O. Chubykalo-Fesenko, U. Nowak, H. Kachkachi, O. N. Mryasov, R. F. Evans, and R. W. Chantrell. Multiscale modeling of magnetic materials: Temperature dependence of the exchange stiffness. *Phys. Rev. B*, 82(13):134440, oct 2010.
- [7] P. Bak and M. H. Jensen. Theory of helical magnetic structures and phase transitions in MnSi and FeGe. *Journal of Physics C: Solid State Physics*, 13(31):L881–L885, 1980.
- [8] G. Baym. Lectures in Quantum Mechanics Boulder, CO, 1974.

- [9] A. Belabbes, G. Bihlmayer, F. Bechstedt, S. Blügel, and A. Manchon. Hund’s rule-driven Dzyaloshinskii-Moriya interaction at 3d-5d interfaces. pages 1–7, 2016.
- [10] L. Bellaïche and David Vanderbilt. Virtual crystal approximation revisited: Application to dielectric and piezoelectric properties of perovskites. *Phys. Rev. B*, 61(12):7877–7882, mar 2000.
- [11] B. Andrei Bernevig and Taylor L. Hughes. *Topological insulators and topological superconductors*. Princeton University Press, 2013.
- [12] M. V. Berry. Quantal Phase Factors Accompanying Adiabatic Changes. *Proceedings of the Royal Society of London A: Mathematical, Physical and Engineering Sciences*, 392(1802):45–57, 1984.
- [13] Felix Bloch. Über die Quantenmechanik der Elektronen in Kristallgittern. *Zeitschrift für Physik*, 52(7-8):555–600, 1929.
- [14] E. I. Blount. Formalisms of band theory. *Solid State Physics*, 13:305–373, 1962.
- [15] A. N. Bogdanov, U. K. Rössler, C. Pfleiderer, U. K. Rößler, and C. Pfleiderer. Modulated and localized structures in cubic helimagnets. *Physica B: Condensed Matter*, 359361:1162–1164, 2005.
- [16] A. N. Bogdanov and D.A. Yablonskii. Thermodynamically stable “vortices” in magnetically ordered crystals. The mixed state of magnets. *Zh. Eksp. Teor. Fiz*, 95(1):178, 1989.
- [17] A. Bohm, A. Mostafazadeh, Koiyumi H., Niu Q., and Zwanzinger J. *The Geometric Phase in Quantum Systems: Foundations, Mathematical Concepts*,

- and Applications in Molecular and Condensed Matter Physics*. Springer Berlin Heidelberg, 2003.
- [18] Max Born and Robert Oppenheimer. Zur quantentheorie der molekeln. *Annalen der Physik*, 389(20):457–484, 1927.
- [19] W. F. Brinkman and R. J. Elliott. Theory of Spin-Space Groups. *Proceedings of the Royal Society of London A: Mathematical, Physical and Engineering Sciences*, 294(1438):343–358, 1966.
- [20] P. Bruno, V. Dugaev, and M. Taillefumier. Topological Hall Effect and Berry Phase in Magnetic Nanostructures. *Phys. Rev. Lett.*, 93(9):096806, aug 2004.
- [21] Patrick Bruno. Tight-binding approach to the orbital magnetic moment and magnetocrystalline anisotropy of transition-metal monolayers. *Physical Review B*, 39(1):865–868, jan 1989.
- [22] D. M. Ceperley and B. J. Alder. Ground state of the electron gas by a stochastic method. *Physical Review Letters*, 45(7):566–569, aug 1980.
- [23] Hua Chen, Qian Niu, and a. H. MacDonald. Anomalous Hall Effect Arising from Noncollinear Antiferromagnetism. *Phys. Rev. Lett.*, 112(1):017205, jan 2014.
- [24] E. Şaşıoğlu, L. M. Sandratskii, and P. Bruno. First-principles calculation of the intersublattice exchange interactions and Curie temperatures of the full Heusler alloys Ni_2MnX ($X=\text{Ga,In,Sn,Sb}$). *Physical Review B - Condensed Matter and Materials Physics*, 70(2):24427, jul 2004.
- [25] E. Şaşıoğlu, L. M. Sandratskii, P. Bruno, and I. Galanakis. Exchange interactions and temperature dependence of magnetization in half-metallic

- Heusler alloys. *Physical Review B - Condensed Matter and Materials Physics*, 72(18):184415, nov 2005.
- [26] Elbio Dagotto and Adriana Moreo. Phase diagram of the frustrated spin-1/2 Heisenberg antiferromagnet in 2 dimensions. *Physical Review Letters*, 63(19):2148–2151, 1989.
- [27] P. A. M. Dirac. Note on Exchange Phenomena in the Thomas Atom, 1930.
- [28] J. F. Ditusa, S. B. Zhang, K. Yamaura, Y. Xiong, J. C. Prestigiacomo, B. W. Fulfer, P. W. Adams, M. I. Brickson, D. A. Browne, C. Capan, Z. Fisk, and Julia Y. Chan. Magnetic, thermodynamic, and electrical transport properties of the noncentrosymmetric B20 germanides MnGe and CoGe. *Physical Review B - Condensed Matter and Materials Physics*, 90(14):1–14, 2014.
- [29] W. Döring. Handbuch der Physik XVIII/2. 1966.
- [30] R. Drautz and M. Fähnle. Spin-cluster expansion: Parametrization of the general adiabatic magnetic energy surface with *ab initio* accuracy. *Phys. Rev. B*, 69(10):104404, mar 2004.
- [31] Bertrand Dupé, Markus Hoffmann, Charles Paillard, and Stefan Heinze. Tailoring magnetic skyrmions in ultra-thin transition metal films. *Nat. Commun.*, 5(May):4030, jan 2014.
- [32] H. Ebert, D. Ködderitzsch, and J. Minár. Calculating condensed matter properties using the KKR-Green’s function method recent developments and applications. *Reports on Progress in Physics*, 74(9):096501, 2011.
- [33] H. Ebert and S. Mankovsky. Anisotropic exchange coupling in diluted magnetic semiconductors: *Ab initio* spin-density functional theory. *Phys. Rev. B*, 79(4):45209, jan 2009.

- [34] J. Engelke, D. Menzel, and V. A. Dyadkin. Thin film MnGe grown on Si(111). *Journal of physics. Condensed matter : an Institute of Physics journal*, 25(47):472201, 2013.
- [35] J. Enkovaara, O. Heczko, A. Ayuela, R. M. Nieminen, J. Jalkanen, L. Nordström, and R. M. Nieminen. First-principles calculations of spin spirals in Ni₂MnGa and Ni₂MnAl. *Phys. Rev. B*, 67(5):054417, feb 2003.
- [36] T. Ericsson, W. Karner, L Häggström, and K Chandra. Magnetic Structure of Cubic FeGe. *Physica Scripta*, 23:1118–1121, 1981.
- [37] E. Fermi. Un metodo statistico per la determinazione di alcune priorietà dell’atome., volume = 6, year = 1927. *Rend. Accad. Naz. Lincei*, (602-607):602–607.
- [38] A. Fert and P. M. Levy. Role of Anisotropic Exchange Interactions in Determining the Properties of Spin-Glasses. *Phys. Rev. Lett.*, 44(23):1538, 1980.
- [39] Albert Fert, Vincent Cros, and J. Sampaio. Skyrmions on the track. *Nature nanotechnology*, 8(3):152–156, mar 2013.
- [40] V. Fock. Näherungsmethode zur Lösung des quantenmechanischen Mehrkörperproblems. *Zeitschrift für Physik*, 61(1-2):126–148, 1930.
- [41] W. M. C. Foulkes, L. Mitas, R. J. Needs, and G. Rajagopal. Quantum Monte Carlo simulations of solids. *Rev. Mod. Phys.*, 73(1):33–83, jan 2001.
- [42] C. Franz, F. Freimuth, A. Bauer, R. Ritz, C. Schnarr, C. Duvinage, T. Adams, S. Blügel, A. Rosch, Y. Mokrousov, and C. Pfleiderer. Real-space and reciprocal-space berry phases in the hall effect of Mn_{1-x}Fe_xSi. *Physical Review Letters*, 112(18):186601, may 2014.

- [43] F. Freimuth, Y. Mokrousov, D. Wortmann, S. Heinze, and S. Blügel. Maximally localized Wannier functions within the FLAPW formalism. *Phys. Rev. B*, 78(3):35120, jul 2008.
- [44] Frank Freimuth, Robert Bamler, Yuriy Mokrousov, and Achim Rosch. Phase-space Berry phases in chiral magnets: Dzyaloshinskii-Moriya interaction and the charge of skyrmions. *Phys. Rev. B*, 88(21):214409, dec 2013.
- [45] Frank Freimuth, Stefan Blügel, and Yuriy Mokrousov. Berry phase theory of Dzyaloshinskii-Moriya interaction and spin-orbit torques. *Journal of physics. Condensed matter : an Institute of Physics journal*, 26(10):104202, mar 2014.
- [46] J. C. Gallagher, K. Y. Meng, J. T. Brangham, H. L. Wang, B. D. Esser, D. W. McComb, and F. Y. Yang. Robust Zero-Field Skyrmion Formation in FeGe Epitaxial Thin Films. *arXiv:1604.06684*, pages 1–20, 2016.
- [47] J. Gayles, F. Freimuth, T. Schena, G. Lani, P. Mavropoulos, R. A. Duine, S. Blügel, J. Sinova, and Y. Mokrousov. Dzyaloshinskii-Moriya Interaction and Hall Effects in the Skyrmion Phase of $\text{Mn}_{1-x}\text{Fe}_x\text{Ge}$. *Physical Review Letters*, 115(3):1–6, 2015.
- [48] David Jeffery Griffiths. *Introduction to quantum mechanics*. Pearson Education India, 2005.
- [49] S. V. Grigoriev, N. M. Potapova, S. Siegfried, V. A. Dyadkin, E. V. Moskvin, V. Dmitriev, D. Menzel, C. D. Dewhurst, D. Chernyshov, R. A. Sadykov, L. N. Fomicheva, and A. V. Tsvyashchenko. Chiral Properties of Structure and Magnetism in $\text{Mn}_{1-x}\text{Fe}_x\text{Ge}$ Compounds : When the Left and the Right are Fighting , Who Wins ? *Phys. Rev. Lett.*, 114:207201, 2013.

- [50] S. V. Grigoriev, S. Siegfried, E. V. Altynbayev, N. M. Potapova, V. Dyadkin, E. V. Moskvina, D. Menzel, A. Heinemann, S. N. Axenov, L. N. Fomicheva, and A. V. Tsvyashchenko. Flip of spin helix chirality and ferromagnetic state in $\text{Fe}_{1-x}\text{Co}_x\text{Ge}$ compounds T (K). *Phys. Rev. B*, 90:174414, 2014.
- [51] S. V. Grigoriev, a. S. Sukhanov, and S. V. Maleyev. From spiral to ferromagnetic structure in B20 compounds: Role of cubic anisotropy. *Physical Review B*, 91(22):224429, 2015.
- [52] O. Gunnarsson. Band model for magnetism of transition metals in the spin-density-functional formalism. *Journal of Physics F: Metal Physics*, 6(4):587, 1976.
- [53] O. Gunnarsson, B. I. Lundqvist, and J. W. Wilkins. Contribution to the cohesive energy of simple metals: Spin-dependent effect. *Phys. Rev. B*, 10(4):1319–1327, aug 1974.
- [54] S. Halilov, H. Eschrig, a. Perlov, and P. Oppeneer. Adiabatic spin dynamics from spin-density-functional theory: Application to Fe, Co, and Ni. *Physical Review B*, 58(1):293–302, 1998.
- [55] Douglas Rayne Hartree. The wave mechanics of an atom with a non-Coulomb central field. Part I. Theory and methods, 1928.
- [56] Douglas Rayne Hartree. The wave mechanics of an atom with a non-Coulomb central field. Part II. Some results and discussion, 1928.
- [57] M. Heide, G. Bihlmayer, and S. Blügel. Describing Dzyaloshinskii-Moriya spirals from first principles. *Physica B*, 404(18):2678–2683, 2009.
- [58] M. Heide, G. Bihlmayer, and Stefan Blügel. Dzyaloshinskii-Moriya interaction accounting for the orientation of magnetic domains in ultrathin films:

- Fe/W(110). *Phys. Rev. B*, 78(14):140403, oct 2008.
- [59] Stefan Heinze, Kirsten von Bergmann, Matthias Menzel, Jens Brede, André Kubetzka, Roland Wiesendanger, G. Bihlmayer, and Stefan Blügel. Spontaneous atomic-scale magnetic skyrmion lattice in two dimensions. *Nature Physics*, 7(9):713–718, jul 2011.
- [60] C. Herring. Magnetism: Exchange interactions among itinerant electrons. In George Tibor Rado and Harry Suhl, editors, *Magnetism*. Academic Press, 1966.
- [61] C. Herring. Magnetism, vol. 4. by *GT Rado and H. Suhl*, *Acad. Press, New York*, 1966.
- [62] Markus Hoffmann, J. Weischenberg, Bertrand Dupé, Franck Freimuth, Paolo Ferriani, Y. Mokrousov, and Stefan Heinze. Topological orbital magnetization and emergent Hall effect of an atomic-scale spin lattice at a surface. *Physical Review B*, 92(2):020401, 2015.
- [63] Mahboubeh Hortamani, Leonid Sandratskii, Peter Kratzer, Ingrid Mertig, and Matthias Scheffler. Exchange interactions and critical temperature of bulk and thin films of MnSi: A density functional theory study. *Physical Review B - Condensed Matter and Materials Physics*, 78(10):104402, sep 2008.
- [64] S. X. Huang and C. L. Chien. Extended skyrmion phase in epitaxial FeGe(111) thin films. *Physical Review Letters*, 108(26):1–5, 2012.
- [65] Y. Ishikawa, K. Tajima, D. Bloch, and M. Roth. Helical spin structure in manganese silicide MnSi. *Solid State Communications*, 19(6):525–528, 1976.
- [66] Peong-Hwa Jang, Kyungmi Song, Seung-Jae Lee, Seo-Won Lee, and Kyung-Jin Lee. Detrimental effect of interfacial Dzyaloshinskii-Moriya interaction on

- perpendicular spin-transfer-torque magnetic random access memory. *Applied Physics Letters*, 107(20), 2015.
- [67] T. Jeong and W. E. Pickett. Implications of the B20 crystal structure for the magnetoelectronic structure of MnSi. *Physical Review B - Condensed Matter and Materials Physics*, 70(7):075114, aug 2004.
- [68] R. O. Jones and O. Gunnarsson. The density functional formalism, its applications and prospects. *Rev. Mod. Phys.*, 61(3):689–746, jul 1989.
- [69] F. Jonietz, S. Mühlbauer, C. Pfleiderer, A. Neubauer, W. Münzer, A. Bauer, T. Adams, R. Georgii, P. Böni, R. A. Duine, Karin Everschor, M. Garst, and A. Rosch. Spin transfer torques in MnSi at ultralow current densities. *Science (New York, N.Y.)*, 330(6011):1648–51, dec 2010.
- [70] N. Kanazawa, J. H. Kim, D. S. Inosov, J. S. White, N. Egetenmeyer, J. L. Gavilano, S. Ishiwata, Y. Onose, T. Arima, B. Keimer, and Y. Tokura. Possible skyrmion-lattice ground state in the B20 chiral-lattice magnet MnGe as seen via small-angle neutron scattering. *Physical Review B - Condensed Matter and Materials Physics*, 86(13):1–7, 2012.
- [71] N. Kanazawa, Y. Onose, T. Arima, D. Okuyama, K. Ohoyama, S. Wakimoto, K. Kakurai, S. Ishiwata, and Y. Tokura. Large Topological Hall Effect in a Short-Period Helimagnet MnGe. *Phys. Rev. Lett.*, 106(15):156603, apr 2011.
- [72] N. Kanazawa, K. Shibata, and Y. Tokura. Variation of spin-orbit coupling and related properties in skyrmionic system $\text{Mn}_{1-x}\text{Fe}_x\text{Ge}$. *New Journal of Physics*, 18(4):1–6, 2016.
- [73] Vikas Kashid, Timo Schena, Bernd Zimmermann, Yuriy Mokrousov, Stefan Blügel, Vaishali Shah, and H. G. Salunke. Dzyaloshinskii-Moriya interaction

- and chiral magnetism in 3d5d zigzag chains: Tight-binding model and ab initio calculations. *Phys. Rev. B*, 90(5):054412, aug 2014.
- [74] Tadao Kasuya. A Theory of Metallic Ferro- and Antiferromagnetism on Zener's Model. *Progress of Theoretical Physics*, 16(1):45–57, 1956.
- [75] Mitsuo Kataoka and Osamu Nakanishi. Helical spin density wave due to antisymmetric exchange interaction. *Journal of the Physical Society of Japan*, 50(12):3888–3896, 1981.
- [76] M. Kawasaki, M. Ichikawa, F. Kagawa, and Y. Tokura. Discretized Topological Hall Effect Emerging from Skyrmions in Constricted Geometry. pages 1–5, 2015.
- [77] Efthimios Kaxiras. *Atomic and electronic structure of solids*. Cambridge University Press, 2003.
- [78] I. Kézsmárki, S. Bordács, P. Milde, E. Neuber, L. M. Eng, J. S. White, H. M. Rønnow, C. D. Dewhurst, M. Mochizuki, K. Yanai, H. Nakamura, D. Ehlers, V. Tsurkan, and A. Loidl. Néel-type skyrmion lattice with confined orientation in the polar magnetic semiconductor GaV4S8. *Nat. Mater.*, 14(11):1116–22, 2015.
- [79] Toru Kikuchi, Takashi Koretsune, Ryotaro Arita, and Gen Tatara. Dzyaloshinskii-Moriya Interaction as a Consequence of a Doppler Shift due to Spin-Orbit-Induced Intrinsic Spin Current. *Physical Review Letters*, 116(24):247201, feb 2016.
- [80] Charles Kittel. Physical Theory of Ferromagnetic Domains. *Rev. Mod. Phys.*, 21(4):541–583, oct 1949.

- [81] D. D. Koelling and B. N. Harmon. A technique for relativistic spin-polarised calculations. *Journal of Physics C: Solid State Physics*, 10(16):3107, 1977.
- [82] W. Kohn. Construction of Wannier Functions and Applications to Energy Bands. *Phys. Rev. B*, 7(10):4388–4398, may 1973.
- [83] W. Kohn and L. J. Sham. Self-Consistent Equations Including Exchange and Correlation Effects. *Phys. Rev.*, 140(4A):A1133—A1138, nov 1965.
- [84] Takashi Koretsune, Naoto Nagaosa, and Ryotaro Arita. Control of Dzyaloshinskii-Moriya interaction in $\text{Mn}_{1-x}\text{Fe}_x\text{Ge}$: a first-principles study. mar 2015.
- [85] G. F. Koster. Localized Functions in Molecules and Crystals. *Phys. Rev.*, 89(1):67–77, jan 1953.
- [86] H. A. Kramers. L’interaction Entre les Atomes Magnétogènes dans un Cristal Paramagnétique. *Physica*, 1(1-6):182–192, jan 1934.
- [87] A. Kundu and S. Zhang. Dzyaloshinskii-Moriya interaction mediated by spin-polarized band with Rashba spin-orbit coupling. *Phys. Rev. B*, 92:094434, 2015.
- [88] C. Le Caër, G. Le Caër, and B. Roques. Domaines d’existence et propriétés magnetiques des germaniures ternaires monocliniques $\text{Fe}_{1-x}\text{Co}_x\text{Ge}$ et $\text{Fe}_{1-x}\text{Ni}_x\text{Ge}$. *Journal of Solid State Chemistry*, 16(3-4):307–315, 1976.
- [89] Mel Levy. Universal variational functionals of electron densities, first-order density matrices, and natural spin-orbitals and solution of the v -representability problem. *Proceedings of the National Academy of Sciences*, 76(12):6062–6065, 1979.

- [90] Elliott H. Lieb. Density functionals for Coulomb systems. In *Density Functional Methods in Physics*, pages 31–80. Springer, 1985.
- [91] A. I. Liechtenstein, M. I. Katsnelson, V. P. Antropov, and V. A. Gubanov. Local spin density functional approach to the theory of exchange interactions in ferromagnetic metals and alloys. *Journal of Magnetism and Magnetic Materials*, 67(1):65–74, 1987.
- [92] A. I. Liechtenstein, M. I. Katsnelson, V. P. Antropov, and V. A. Gubanov. Local spin density functional approach to the theory of exchange interactions in ferromagnetic metals and alloys. *Journal of Magnetism and Magnetic Materials*, 67(1):65–74, 1987.
- [93] L. Ludgren, O. Beckman, V. Attia, S. P. Bhattacharjee, and M. Richardson. Helical Spin Arrangement in Cubic FeGe. *Physica Scripta*, 1:69–72, 1970.
- [94] A. H. MacDonald, W. E. Pickett, and D. D. Koelling. A linearised relativistic augmented-plane-wave method utilising approximate pure spin basis functions. *Journal of Physics C: Solid State Physics*, 13(14):2675, 1980.
- [95] A. H. MacDonald and S. H. Vosko. A relativistic density functional formalism. *Journal of Physics C: Solid State Physics*, 12(15):2977, 1979.
- [96] J. M. MacLaren, T. C. Schulthess, W. H. Butler, R. Sutton, and M. McHenry. Electronic structure, exchange interactions, and Curie temperature of FeCo. *Journal of Applied Physics*, 85(8):4833, 1999.
- [97] O. L. Makarova, A. V. Tsvyashchenko, G. Andre, F. Porcher, L. N. Fomicheva, N. Rey, and I. Mirebeau. Neutron diffraction study of the chiral magnet MnGe. *Phys. Rev. B*, 85(20):205205, may 2012.

- [98] S. V. Maleyev. Cubic magnets with Dzyaloshinskii-Moriya interaction at low temperature. *Phys. Rev. B*, 73:174402, 2006.
- [99] Michael P. Marder. *Condensed matter physics*. John Wiley & Sons, 2010.
- [100] R. M. Martin. *Electronic Structure: Basic Theory and Practical Methods*. Cambridge University Press, 2004.
- [101] N. Marzari and D. Vanderbilt. Maximally Localized Generalized Wannier Functions for Composite Energy Bands. *Physical Review B*, 56(20):22, nov 1997.
- [102] Nicola Marzari, Arash A. Mostofi, Jonathan R. Yates, Ivo Souza, and David Vanderbilt. Maximally localized Wannier functions: Theory and applications. *Rev. Mod. Phys.*, 84(4):1419–1475, oct 2012.
- [103] Michael J. Mehl and Dimitrios A. Papaconstantopoulos. Applications of a tight-binding total-energy method for transition and noble metals: Elastic constants, vacancies, and surfaces of monatomic metals. *Phys. Rev. B*, 54(7):4519–4530, 1996.
- [104] O Meshcheriakova, S Chadov, A K Nayak, U K Rö\ssler, J Kübler, G André, A A Tsirlin, J Kiss, S Hausdorf, A Kalache, W Schnelle, M Nicklas, and C Felser. Large Noncollinearity and Spin Reorientation in the Novel Mn_2RhSn Heusler Magnet. *Phys. Rev. Lett.*, 113(8):87203, aug 2014.
- [105] Yuriy Mokrousov and Frank Freimuth. Geometric Phases and Topological Effects. *arXiv:1407.2847*, 2014.
- [106] Yuriy Mokrousov, Hongbin Zhang, Frank Freimuth, Bernd Zimmermann, Nguyen H. Long, Jürgen Weischenberg, Ivo Souza, Phivos Mavropoulos, and Stefan Blügel. Anisotropy of spin relaxation and transverse transport in met-

- als. *Journal of physics. Condensed matter : an Institute of Physics journal*, 25(16):163201, apr 2013.
- [107] D. Morikawa, K. Shibata, N. Kanazawa, X. Z. Yu, and Y. Tokura. Crystal chirality and skyrmion helicity in MnSi and (Fe , Co) Si as determined by transmission electron microscopy. *Phys. Rev. B*, 88:024408, 2013.
- [108] Tôru Moriya. Anisotropic superexchange interaction and weak ferromagnetism. *Phys. Rev.*, 120(1):91–98, 1960.
- [109] Tôru Moriya. New mechanism of anisotropic superexchange interaction. *Phys. Rev. Lett.*, 4(5):228, 1960.
- [110] Tôru Moriya, Osamu Nakanishi, Akira Yanase, and Mitsuo Kataoka. *Springer Series in Solid-State Sciences*, volume 29, pages 126–135. Springer Berlin Heidelberg, 1981.
- [111] Arash A. Mostofi, Jonathan R. Yates, Young Su Lee, Ivo Souza, David Vanderbilt, and Nicola Marzari. wannier90: A tool for obtaining maximally-localised Wannier functions. *Computer Physics Communications*, 178(9):685–699, 2008.
- [112] O. N. Mryasov, A. I. Liechtenstein, L. M. Sandratskii, and V. A. Gubanov. Magnetic structure of FCC iron. *Journal of Physics: Condensed Matter*, 3(39):7683, 1991.
- [113] S. Mühlbauer, B. Binz, F. Jonietz, and C. Pfleiderer. Skyrmion lattice in a chiral magnet. *Science (New York, N.Y.)*, 323(September):915–920, 2009.
- [114] Naoto Nagaosa, Jairo Sinova, Shigeki Onoda, A. H. MacDonald, and N. P. Ong. Anomalous Hall effect. *Rev. Mod. Phys.*, 82(2):1539–1592, may 2010.
- [115] M. Nakahara. *Geometry, Topology, and Physics*. Institute of Physics Publishing, 2003, second edition, 2011.

- [116] O. Nakanishi, A. Yanase, A. Hasegawa, and M. Kataoka. ORIGIN OF THE HELICAL SPIN DENSITY WAVE IN MnSi. *Solid State Communications*, 35(12):995–998, 1980.
- [117] Osamu Nakanishi, Akira Yanase, and Mitsuo Kataoka. Electronic Band Structure and Helical Spin Density Wave of MnSi. In *Electron Correlation and Magnetism in Narrow-Band Systems*, pages 126–135. Springer, 1981.
- [118] Matthias Neef, Klaus Doll, and Gertrud Zwicknagl. Ab initio study of pressure-induced metal-insulator transition in cubic FeGe. *Physical Review B - Condensed Matter and Materials Physics*, 80(3):1–8, 2009.
- [119] G. Nenciu. Dynamics of band electrons in electric and magnetic fields: rigorous justification of the effective Hamiltonians. *Rev. Mod. Phys.*, 63(1):91–127, jan 1991.
- [120] A. Neubauer, C. Pfleiderer, B. Binz, A. Rosch, R. Ritz, P. Niklowitz, and P. Böni. Topological Hall Effect in the A Phase of MnSi. *Phys. Rev. Lett.*, 102(18):186602, may 2009.
- [121] L. Nordström and A. Mavromaras. Magnetic ordering of the heavy rare earths. *Europhys. Lett.*, 49(6):775–781, 2000.
- [122] Robert G. Parr. Density functional theory of atoms and molecules. In *Horizons of Quantum Chemistry*, pages 5–15. Springer, 1980.
- [123] W. Pauli. Über den Zusammenhang des Abschlusses der Elektronengruppen im Atom mit der Komplexstruktur der Spektren. *Zeitschrift für Physik Physik*, 31(1):765–783, 1925.
- [124] W. Pauli. Zur Quantenmechanik des magnetischen Elektrons. *Zeitschrift für Physik*, 43(9):601–623, 1927.

- [125] W. Pauli. The connection between spin and statistics. *Physical Review*, 58(8):716–722, oct 1940.
- [126] John P. Perdew, Kieron Burke, and Matthias Ernzerhof. Generalized Gradient Approximation Made Simple. *Physical Review Letters*, 77(18):3865–3868, 1996.
- [127] John P. Perdew, Adrienn Ruzsinszky, Jianmin Tao, Viktor N. Staroverov, Gustavo E. Scuseria, and Gabor I. Csonka. Prescription for the design and selection of density functional approximations: More constraint satisfaction with fewer fits. *The Journal of Chemical Physics*, 123(6):062201, 2005.
- [128] John P. Perdew and Yue Wang. Accurate and simple analytic representation of the electron-gas correlation energy. *Phys. Rev. B*, 45(23):13244–13249, jun 1992.
- [129] C. Pfleiderer, P. Böni, T. Keller, U. K. Rößler, and A. Rosch. Non-Fermi Liquid Metal Without Quantum Criticality. *Science*, 316(June):1871–1875, 2007.
- [130] M. L. Plumer and M. B. Walker. Wavevector and spin reorientation in MnSi. *Journal of Physics C: Solid State Physics*, 14:4689–4699, 1981.
- [131] N. A. Porter, J. C. Gartside, and C. H. Marrows. Scattering mechanisms in textured FeGe thin films: Magnetoresistance and the anomalous Hall effect. *Phys. Rev. B*, 90(2):24403, jul 2014.
- [132] J. J. Pulikkotil, S. Auluck, P. K. Rout, and R. C. Budhani. Effect of pressure on itinerant magnetism and spin disorder in cubic FeGe. *Journal of Physics: Condensed Matter*, 24(9):96003, 2012.
- [133] Raffaele Resta. Macroscopic polarization in crystalline dielectrics: the geometric phase approach. *Reviews of Modern Physics*, 66(3):899–915, jul 1994.

- [134] Ysical Reveew. Theory of Electronic Transport in Disordered Binary Alloys: Coherent-Potential. 321(3), 1969.
- [135] R. Ritz, M. Halder, C. Franz, A. Bauer, M. Wagner, R. Bamler, A. Rosch, and C. Pfleiderer. Giant generic topological Hall resistivity of MnSi under pressure. *Physical Review B - Condensed Matter and Materials Physics*, 87(13):1–17, 2013.
- [136] Ulrich K. Roessler, A. N. Bogdanov, C Pfleiderer, U K Röbller, A. N. Bogdanov, and C Pfleiderer. Spontaneous skyrmion ground states in magnetic metals. *Nature*, 442(7104):797–801, aug 2006.
- [137] Niklas Romming, Christian Hanneken, Matthias Menzel, Jessica E. Bickel, Boris Wolter, Kirsten von Bergmann, André Kubetzka, and Roland Wiesendanger. Writing and deleting single magnetic skyrmions. *Science (New York, N.Y.)*, 341(6146):636–9, aug 2013.
- [138] U K Röbller. Ab initio study on magnetism and pressure-induced transitions in cubic MnGe. *Journal of Physics: Conference Series*, 391(1):012104, 2012.
- [139] M. A. Ruderman and C. Kittel. Indirect Exchange Coupling of Nuclear Magnetic Moments by Conduction Electrons. *Phys. Rev.*, 96(1):99–102, oct 1954.
- [140] L. M. Sandratskii. Symmetry analysis of electronic states for crystals with spiral magnetic order. I. General properties. *Journal of Physics: Condensed Matter*, 3:8565, 1991.
- [141] L. M. Sandratskii. Noncollinear magnetism in itinerant-electron systems: theory and applications. *Adv. Phys.*, 47:91, 1998.
- [142] Leonid M. Sandratskii. Energy Band Structure Calculations for Crystals with Spiral Magnetic Structure. *Physica Status Solidi*, 136(1):167–180, 1986.

- [143] K. V. Shanavas and S. Satpathy. Electronic structure and the origin of the Dzyaloshinskii-Moriya interaction in MnSi. 195101:1–8, 2016.
- [144] K. Shibata, A. Kovács, N. Kanazawa, R. E. Dunin-Borkowski, and Y. Tokura. Temperature and magnetic field dependence of the internal and lattice structures of skyrmions by off-axis electron holography. pages 1–12, 2016.
- [145] K. Shibata, X. Z. Yu, T. Hara, D. Morikawa, N. Kanazawa, K. Kimoto, S. Ishiwata, Y. Matsui, and Y. Tokura. Towards control of the size and helicity of skyrmions in helimagnetic alloys by spin-orbit coupling. *Nature Nanotechnology*, 8:723–8, 2013.
- [146] N. A. Sinitsyn. Semiclassical theories of the anomalous Hall effect. *Journal of Physics: Condensed Matter*, 20(2):023201, jan 2008.
- [147] Jairo Sinova and A. H. MacDonald. Theory of spin-orbit effects in semiconductors. In T. Dietl, D. D. Awschalom, M. Kaminska, and H. Ohno, editors, *Spintronics, Semicond. Semimet. 82*. Elsevier B.V., 2008.
- [148] Jairo Sinova, Sergio O. Valenzuela, J. Wunderlich, C. H. Back, and T. Jungwirth. Spin Hall effects. *Reviews of Modern Physics*, 87(4):1213–1260, 2015.
- [149] T.H.R. Skyrme. A unified field theory of mesons and baryons. *Nuclear Physics*, 31:556–569, 1962.
- [150] J. C. Slater and G. F. Koster. Simplified LCAO method for the periodic potential problem. *Physical Review*, 94(6):1498–1524, 1954.
- [151] John C. Slater. Fifty Years in Physics and Chemistry.(Book Reviews: Solid State and Molecular Theory. A Scientific Biography). *Science*, 188:839–840, 1975.

- [152] Ivo Souza, Tim Wilkens, and Richard M. Martin. Polarization and localization in insulators: generating function approach. *Physical Review B*, 62(3):25, jul 1999.
- [153] Charles S. Spencer, Nicholas A. Porter, Rowan C. Temple, Christian J. Kinane, Timothy R. Charlton, Sean Langridge, Christopher H. Marrows, Jacob Gayles, Jairo Sinova, Frank Freimuth, Yuriy Mokrousov, and Stefan Blugel. Divergence of the magnetic helical period in $\text{Fe}_{1-x}\text{Co}_x\text{Ge}$ epilayers. (unpublished).
- [154] L. Szunyogh, L. Udvardi, J. Jackson, U. Nowak, and R. Chantrell. Atomistic spin model based on a spin-cluster expansion technique: Application to the IrMn_3/Co interface. *Phys. Rev. B*, 83(2):24401, jan 2011.
- [155] H. Takizawa, T. Sato, T. Endo, and M. Shimada. High-pressure synthesis and electrical and magnetic properties of MnGe and CoGe with the cubic B20 structure. *Journal of Solid State Chemistry*, 73(1):40–46, 1988.
- [156] Toshiaki Tanigaki, Kiyou Shibata, Naoya Kanazawa, Xiuzhen Yu, Yoshinori Onose, Hyun Soon Park, Daisuke Shindo, and Yoshinori Tokura. Real-Space Observation of Short-Period Cubic Lattice of Skyrmions in MnGe . *Nano Letters*, 15(8):5438–5442, 2015.
- [157] Jianmin Tao, John P. Perdew, Viktor N. Staroverov, and Gustavo E. Scuseria. Climbing the Density Functional Ladder: Non-Empirical Meta-Generalized Gradient Approximation Designed for Molecules and Solids. *Physical Review Letters*, 91(14):146401, sep 2003.
- [158] Edward Teller. On the Stability of Molecules in the Thomas-Fermi Theory. *Rev. Mod. Phys.*, 34(4):627–631, oct 1962.
- [159] L. H. Thomas. The calculation of atomic fields, jan 1927.

- [160] Y. Tsunoda. Spin-density wave in cubic γ -Fe and γ -Fe 100-x Co x precipitates in Cu. *Journal of Physics: Condensed Matter*, 1(51):10427, 1989.
- [161] M. Uhl, L. M. Sandratskii, and J. Kübler. Electronic and magnetic states of γ -Fe. *Journal of Magnetism and Magnetic Materials*, 103(3):314–324, 1992.
- [162] M. Vanatka, J. C. Rojas-Sánchez, J. Vogel, M. Bonfim, A. Thiaville, and S. Pizzini. Velocity asymmetry of Dzyaloshinskii domain walls in the creep and flow regimes. 2015.
- [163] G. Vignale and M. Rasolt. Density-functional theory in strong magnetic fields. *Physical Review Letters*, 59(20):2360–2363, 1987.
- [164] U. von Barth and L. Hedin. A local exchange-correlation potential for the spin polarized case: I. *Journal of Physics C: Solid State Physics*, 5(13):1629–1642, 1972.
- [165] C. S. Wang, R. E. Prange, and V. Korenman. Magnetism in iron and nickel. *Phys. Rev. B*, 25(9):5766–5777, may 1982.
- [166] Xinjie Wang, Jonathan R. Yates, Ivo Souza, and David Vanderbilt. Ab initio calculation of the anomalous Hall conductivity by Wannier interpolation. *Physical Review B - Condensed Matter and Materials Physics*, 74(19):1–15, 2006.
- [167] Gregory H. Wannier. The Structure of Electronic Excitation Levels in Insulating Crystals. *Phys. Rev.*, 52(3):191–197, aug 1937.
- [168] Gregory H. Wannier. Dynamics of band electrons in electric and magnetic fields. *Reviews of Modern Physics*, 34(4):645–655, oct 1962.

- [169] Jürgen Weischenberg, Frank Freimuth, Jairo Sinova, Stefan Blügel, and Yuriy Mokrousov. Ab Initio Theory of the Scattering-Independent Anomalous Hall Effect. *Phys. Rev. Lett.*, 107(10):106601, sep 2011.
- [170] H. Wilhelm, M. Baenitz, M. Schmidt, C. Naylor, R. Lortz, U. K. Rößler, A. A. Leonov, and A. N. Bogdanov. Confinement of chiral magnetic modulations in the precursor region of FeGe. *Journal of Physics: Condensed Matter*, 24(29):294204, 2012.
- [171] H. Wilhelm, M. Baenitz, M. Schmidt, U. K. Rößler, A. A. Leonov, and A. N. Bogdanov. Precursor phenomena at the magnetic ordering of the cubic helimagnet FeGe. *Physical Review Letters*, 107(12):127203, 2011.
- [172] R. Winkler. *Spin-Orbit Coupling effects in Two-Dimensional Electron and Hole Systems*. Springer-Verlag Berlin, 2003.
- [173] Di Xiao, Ming-Che Chang, and Qian Niu. Berry phase effects on electronic properties. *Rev. Mod. Phys.*, 82(3):1959–2007, jul 2010.
- [174] Di Xiao, Junren Shi, and Qian Niu. Berry Phase Correction to Electron Density of States in Solids. *Phys. Rev. Lett.*, 95(13):137204, sep 2005.
- [175] H. Yamada, K. Terao, and T. Goto. Itinerant-electron metamagnetism of Fe(Si,Ge) with B20-type structure. *Physica B: Condensed Matter*, 344(1-4):451–455, 2004.
- [176] Yugui Yao, Leonard Kleinman, A. H. MacDonald, Jairo Sinova, T. Jungwirth, Ding-sheng Wang, Enge Wang, and Qian Niu. First Principles Calculation of Anomalous Hall Conductivity in Ferromagnetic bcc Fe. *Phys. Rev. Lett.*, 92(3):1–4, jan 2004.

- [177] Jonathan R. Yates, Xinjie Wang, David Vanderbilt, and Ivo Souza. Spectral and Fermi surface properties from Wannier interpolation. *Physical Review B - Condensed Matter and Materials Physics*, 75(19):195121, 2007.
- [178] Kei Yosida. Magnetic Properties of Cu-Mn Alloys. *Phys. Rev.*, 106(5):893–898, jun 1957.
- [179] X. Z. Yu, Y. Onose, N. Kanazawa, J. H. Park, J. H. Han, Y. Matsui, N. Nagaosa, and Y. Tokura. Real-space observation of a two-dimensional skyrmion crystal. *Nature*, 465(7300):901–904, jun 2010.
- [180] Clarence Zener. Interaction between the d -Shells in the Transition Metals. II. Ferromagnetic Compounds of Manganese with Perovskite Structure. *Phys. Rev.*, 82(3):403–405, may 1951.
- [181] Xichao Zhang, G P Zhao, Hans Fangohr, J Ping Liu, W X Xia, J Xia, and F J Morvan. Skyrmion-skyrmion and skyrmion-edge repulsions in skyrmion-based racetrack memory. *Sci. Rep.*, 5:7643, jan 2015.
- [182] Xichao Zhang, Yan Zhou, Motohiko Ezawa, G P Zhao, and Weisheng Zhao. Magnetic skyrmion transistor: skyrmion motion in a voltage-gated nanotrack. *Sci. Rep.*, 5:11369, jun 2015.

APPENDIX A

BLOCH THEOREM

A.1 Periodic Systems

Lattices are commonly described by a set of vectors $\mathbf{a}_1, \mathbf{a}_2, \dots, \mathbf{a}_N$ called primitive lattice vectors, where N is the number of dimensions. The position of all lattice points are described by the lattice vectors \mathbf{R} that connect all equivalent points in space and is referred to as the Bravais lattice.

$$\mathbf{R} = n_1\mathbf{a}_1 + n_2\mathbf{a}_2 + \dots n_N\mathbf{a}_N \quad (\text{A.1})$$

The volume Ω enclosed by three primitive lattice vectors in three dimensions is considered the primitive unit cell: $\Omega = |\mathbf{a}_1 \cdot (\mathbf{a}_2 \times \mathbf{a}_3)|$

In order to actually have a crystal one needs a lattice and a basis. The basis describes the positions of atoms/ions in regards to the the lattice. It is often better to describe the behavior of electrons in the reciprocal space of the crystal. In three dimensions the reciprocal vectors are defined by

$$\mathbf{b}_1 = \frac{2\pi(\mathbf{a}_2 \times \mathbf{a}_3)}{\Omega}, \quad \mathbf{b}_2 = \frac{2\pi(\mathbf{a}_3 \times \mathbf{a}_1)}{\Omega}, \quad \mathbf{b}_3 = \frac{2\pi(\mathbf{a}_1 \times \mathbf{a}_2)}{\Omega} \quad (\text{A.2})$$

Where $\mathbf{a}_i \cdot \mathbf{b}_j = 2\pi\delta_{ij}$ shows the property $e^{i\mathbf{G} \cdot \mathbf{R}} = 1$. This defines the reciprocal lattice vector \mathbf{G} which connects all equivalent points in reciprocal space analogous to eq. 1 it is written

$$\mathbf{G} = m_1\mathbf{b}_1 + m_2\mathbf{b}_2 + \dots m_N\mathbf{b}_N \quad (\text{A.3})$$

For a given function $f(\mathbf{r})$ with the periodicity of the lattice can be written as a function of the Fourier transform.

$$f(\mathbf{r}) = \sum_{\mathbf{G}} e^{i\mathbf{G}\cdot\mathbf{r}} f(\mathbf{G}) \quad (\text{A.4})$$

Because of the periodicity the function only needs to be studied in the primitive unit cell with respect to \mathbf{r} . Equation A.4 leads to Bloch Theorem in the single particle case.

For electrons moving about a simple potential $U(\mathbf{r})$ that is periodic, the electrons can be considered to be subject to an approximated potential,

$$U(\mathbf{r} + \mathbf{R}) = U(\mathbf{r}) \quad \text{For all } \mathbf{R} \text{ in the lattice.} \quad (\text{A.5})$$

This model permits the prediction of real properties of solids such that some are metals, as opposed to semiconductors or insulators. The single-particle wavefunctions will also have a symmetry but subject to a phase factor

$$\Psi_k(\mathbf{r} + \mathbf{R}) = e^{i\mathbf{k}\cdot\mathbf{R}} \Psi_k(\mathbf{r}) \quad (\text{A.6})$$

Where the wavefunction can be decomposed to a periodic functions and plane waves:

$$\Psi_k(\mathbf{r}) = e^{i\mathbf{k}\cdot\mathbf{r}} u_k(\mathbf{r}) \quad (\text{A.7})$$

The periodic function $u_k(\mathbf{r})$ contains the full symmetry of the Bravais lattice

A.2 Generalized Bloch Theorem

In the case of spin-spiral with rotation angle $\varphi = \mathbf{q}\mathbf{R}_n$ that is counterclockwise. The exchange-correlation field, \mathbf{B}_{xc} constantly varies from one unit cell to the next.

Then the Hamiltonian $\mathcal{H}(\mathbf{r})$, must satisfy

$$\mathcal{H}(\mathbf{r} + \mathbf{R}_n) = \mathcal{U}(\mathbf{q}\mathbf{R}_n)\mathcal{H}(\mathbf{r})\mathcal{U}^\dagger(\mathbf{q}\mathbf{R}_n). \quad (\text{A.8})$$

Where $\mathcal{U}(\mathbf{q}\mathbf{R}_n)$ is the spin 1/2 rotation matrix,

$$\mathcal{U} = \begin{pmatrix} e^{-i\varphi/2} & 0 \\ 0 & e^{i\varphi/2} \end{pmatrix}. \quad (\text{A.9})$$

A general translation operator can be defined $\mathcal{T}_n = \{-\mathbf{q}\mathbf{R}_n|\mathbb{1}|\mathbf{R}\}$, where a translation and a spin rotation operator are combined with $\mathbb{1}$ being the identity matrix. The translation operator is part of the spin space group and satisfy the relation $\mathcal{T}_n\mathcal{T}_m = \mathcal{T}_m\mathcal{T}_n = \mathcal{T}_{n+m}$. Applying this generalized translation operator to $\mathcal{H}\psi$ leads to,

$$\begin{aligned} \mathcal{T}_n\mathcal{H}(\mathbf{r})\psi(\mathbf{r}) &= \mathcal{U}(-\mathbf{q}\mathbf{R}_n)\mathcal{H}(\mathbf{r} + \mathbf{R}_n)\mathcal{U}^\dagger(-\mathbf{q}\mathbf{R}_n)\mathcal{U}(-\mathbf{q}\mathbf{R}_n)\psi(\mathbf{r}) \\ &= \mathcal{H}(\mathbf{r})\mathcal{U}(-\mathbf{q}\mathbf{R}_n)\psi(\mathbf{r}) \end{aligned} \quad (\text{A.10})$$

Which leaves the Hamiltonian invariant with the generalized translation operator, i.e. $\mathcal{T}_n\mathcal{H} = \mathcal{H}\mathcal{T}_n$. The Bloch eigenstates take the form,

$$\mathcal{T}_n\psi(\mathbf{k}, \mathbf{r}) = \mathcal{U}(-\mathbf{q}\mathbf{R}_n)\psi(\mathbf{k}, \mathbf{r} + \mathbf{R}_n) = e^{-i\mathbf{k}\cdot\mathbf{R}_n}\psi(\mathbf{k}, \mathbf{r}) \quad (\text{A.11})$$

and the eigenstates have the form,

$$\psi(\mathbf{k}, \mathbf{r}) = e^{-i\mathbf{k}\cdot\mathbf{r}} \begin{pmatrix} e^{-i\mathbf{q}\cdot\mathbf{r}}\alpha(\mathbf{k}, \mathbf{r}) \\ e^{i\mathbf{q}\cdot\mathbf{r}}\beta(\mathbf{k}, \mathbf{r}) \end{pmatrix}. \quad (\text{A.12})$$

Here α and β are periodic functions, i.e. $\alpha(\mathbf{k}, \mathbf{r}) = \alpha(\mathbf{k}, \mathbf{r} + \mathbf{R}_n)$.

APPENDIX B

EXCHANGE AND CORRELATIONS FUNCTIONALS

In this appendix the analytical forms for the LDA and GGA exchange-correlation energies functional are shown. The forms of these energies are relatively simple compared to other potentials and form the lowest rungs of the Jacob's Ladder.

B.1 Local Density Approximation

In general the spin unpolarized exchange-correlation energy functional takes the form,

$$E_{xc}^{\text{LDA}}[n] = \int n(\mathbf{r})\epsilon_{xc}[n(\mathbf{r})]d\mathbf{r}, \quad (\text{B.1})$$

and the spin polarized,

$$E_{xc}^{\text{LSDA}}[n, \mathbf{m}] = \int n(\mathbf{r})\epsilon_{xc}[n(\mathbf{r}), \mathbf{m}(\mathbf{r})]d\mathbf{r}. \quad (\text{B.2})$$

The electron density $n(\mathbf{r}) = \sum_{i,s} |\psi_{i,s}(\mathbf{r})|^2$ and the spin density $\mathbf{m}(\mathbf{r}) = \sum_i \langle \psi_i(\mathbf{r}) | \boldsymbol{\sigma} | \psi_i(\mathbf{r}) \rangle$ are functions of the position \mathbf{r} . The spin index is denoted as s for up/down bands, i . In the case of unpolarized LDA the spin index is taken out of the sum, due to the degeneracy of the wavefunctions. The exact exchange of a unpolarized homogenous electron gas is [27],

$$E_x^{\text{LDA}}[n] = -\frac{3}{4} \left(\frac{3}{\pi}\right)^{1/3} \int n(\mathbf{r})^{4/3} d\mathbf{r}. \quad (\text{B.3})$$

The energy functional for the correlation has analytic expressions for the high and low density limits [122].

The exchange-correlation potential is,

$$v_{xc}^{\text{LDA}}(\mathbf{r}) = \frac{\partial E_{xc}^{\text{LDA}}}{\partial n} = \epsilon_{xc}(n(\mathbf{r})) + n(\mathbf{r}) \frac{\partial \epsilon_{xc}(n(\mathbf{r}))}{\partial n}. \quad (\text{B.4})$$

Within in the LSDA the exchange-correlation field is parallel to the spin density,
The exchange-correlation potential is,

$$\mathbf{B}_{xc}(\mathbf{r}) = \frac{\delta E_{xc}^{\text{LDA}}[n, \mathbf{m}]}{\delta \mathbf{m}} = n(\mathbf{r}) \frac{\partial \epsilon_{xc}(n(\mathbf{r}), m(\mathbf{r}))}{\partial m(\mathbf{r})} \hat{\mathbf{m}}. \quad (\text{B.5})$$

B.2 Generalized Gradient Approximation

The GGA functional [126] corrects for rapid variations in the LDA functional by adding derivatives to the exchange-correlation potential as,

$$E_{xc}^{\text{GGA}}[n] = E_{xc}^{\text{LDA}}[n] + \int \Delta \epsilon_{xc}[n(\mathbf{r}), |\nabla n(\mathbf{r})|] d\mathbf{r}, \quad (\text{B.6})$$

APPENDIX C

CONVERGENCE

For the collinear ferromagnetic first principle calculations with and without spin-orbit coupling we found that the planewave cutoff radius K_{max} of 4.0 bohr^{-1} and a $12 \times 12 \times 12$ \mathbf{k} -points equivalent to 119 N_k in the IBZ converged the total energy to less than 0.1 meV (see fig. C.1). The calculation of the self-consistent spin-spiral

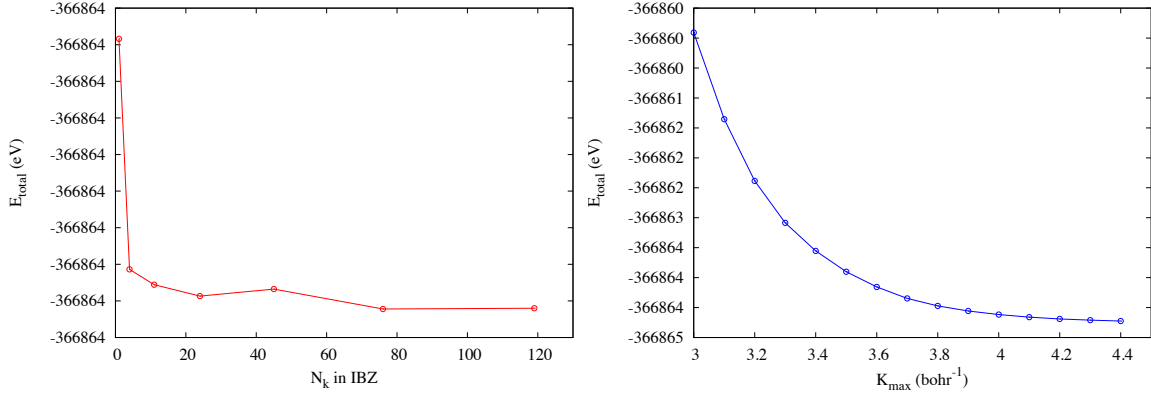


Figure C.1: *Left:* Total energy convergence in FeGe as a function of the number of kpoints in the IBZ. *Right:* Total energy convergence in FeGe as a function of the planewave cutoff radius K_{max} .

is found to be converged at $18 \times 18 \times 18$ in the full BZ, however the calculation of the DMI is converged for < 1 meV at $24 \times 24 \times 24$. For the calculation of the DMI and the exchange stiffness the k-grid of $24 \times 24 \times 24$ is used.